WCAP-14216

AP600 CORE MAKEUP TANK TEST ANALYSIS

December 1994

J. P. Cunningham
R. C. Haberstroh
L. E. Hochreiter
R. F. Wright

WESTINGHOUSE ELECTRIC CORPORATION
Energy Systems Business Unit
P.O. Box 355
Pittsburgh, Pennsylvania 15230-0355

TABLE OF CONTENTS

TABLE OF CONTENTS (Cont.)

LIST OF TABLES

LIST OF FIGURES

LIST OF FIGURES (Cont.)

LIST OF FIGURES (Cont.)

LIST OF FIGURES (Cont.)

LIST OF FIGURES (Cont.)

LIST OF FIGURES (Cont.)

LIST OF FIGURES (Cont.)

LIST OF FIGURES (Cont.)

LIST OF FIGURES (Cont.)

LIST OF FIGURES (Cont.)

ACKNOWLEDGEMENTS

The authors would like to thank J. C. Butler, E. H. Novensdstern, E. J. Piplica, and especially B. E. Rarig for the technical review of the report; D. G. Morgan for the preparation of the figures and the data; and L. G. McSwain for the excellent editing and coordination effort to complete the report. The authors would also like to express their thanks to D. Kephart who coordinated the word processing effort for the report.

SUMMARY

This report presents the analysis of the AP600 core makeup tank (CMT) test data. The CMT test data have been analyzed to obtain thermal-hydraulic information that will be used for safety analysis computer code model development and verification. There are four test series designed to obtain data on the thermal-hydraulic phenomena needed to model the AP600 plant CMT. These test series include: wall condensation tests, steam mixing and draining tests at constant pressure, steam mixing and draining tests with depressurization, and recirculation with draindown and depressurization. The CMT test program addresses the range of thermal-hydraulic phenomena identified in the phenomena importance ranking table.

1.0 INTRODUCTION

1.1 Background

A unique feature of the AP600 design is the use of passive safety systems to enhance reactor protection following postulated accidents. The core makeup tank (CMT), shown in Figure 1.1-1, is one component of the AP600 passive safety systems. Each tank stores 2000 $ft.^3$ of cold borated water at reactor coolant system (RCS) pressure that can be gravity-injected into the RCS to provide reactivity control and core cooling. The CMTs provide the same function as the high-pressure safety injection system in existing pressurized water reactors (PWRs), with the difference being that current plants require the availability of ac power to perform their safety function, whereas the CMTs perform this function by gravity-driven flows.

The CMTs are connected to the RCS, as shown in Figure 1.1-2, by normally open isolation valves on the cold leg balance line and normally closed isolation valves on the CMT discharge line. The CMT discharge valves open on a safety ("S") signal and remain open. The tanks are maintained at full-system pressure by the cold leg balance lines. During normal operation, the CMTs and the cold leg balance lines are completely filled.

In addition to adding coolant and boron to the reactor systems, the CMTs have an additional safety function. Continued draining of the tank indicates an unrecoverable loss-of-coolant accident (LOCA). When approximately 33 percent of the tank liquid has drained, the CMT level sensing device activates the first stage of the automatic depressurization system (ADS), and the plant begins a controlled blowdown through the ADS valves into the in-containment refueling water storage tank (IRWST). The second- and third-stage ADS valves open based on timers that are started with the opening of ADS stage 1. If the CMTs continue to drain and the volume reaches 20 percent, the fourth-stage ADS valves, which are located on the hot legs, open, providing a large vent path directly to containment to depressurize the RCS to containment pressure. As the RCS depressurizes by opening the ADS valves on the pressurizer and hot legs, the CMTs continue to add coolant to the RCS to maintain continued core cooling during the depressurization.

Each AP600 CMT is a 2000-$ft.^3$ tank consisting of hemispherical heads and a cylindrical shell. The hemispherical heads are stainless-steel-clad carbon steel (0.25-in. stainless cladding) with a total thickness of 4.6 in. The cylindrical portion of the tank is also stainless-steel clad and is a total of 7.78-in. thick. The top of the tank is located 28 ft. above the RCS cold legs, providing a gravity head to drive the flow into the reactor vessel downcomer. The drain line is connected from the bottom of the CMT through an isolation valve and two check valves to the direct vessel injection line. The cold leg balance line between the top of a cold leg and the top of a CMT is an 8-in. schedule 160 pipe with an inside diameter of 6.82 in. There is a normally open isolation valve near the top of this balance line. The AP600 piping schematic for the CMT and its balance lines is shown in Figure 1.1-2.

There are two modes of operation for the CMTs: recirculation and draining. During the initial phase of a small-break LOCA, steam line break, or steam generator tube rupture event, the RCS inventory

remains at or near its steady-state value. When an "S" signal occurs (typically low pressurizer pressure), the reactor coolant pumps trip, and the CMT isolation valves open. With the valves open, buoyancy-driven flow from the CMT to the reactor vessel and return flow from the cold leg to the top of the CMT is initiated, beginning the recirculation phase of operation for the CMTs. The colder, denser CMT water drives flow into the reactor vessel because of the density difference between the CMT water and the cold leg balance line (approximately 20 percent with T_{cold} at 550°F and CMT water at 120°F). Figure 1.1-3 from the AP600 SSAR calculations, shows the calculated CMT discharge flow during the recirculation period for a 2-in. diameter cold leg break. This flow will continue and steadily decrease as the colder CMT water is replaced by hotter water from the balance line; thereby decreasing the thermal driving head.

As the break continues to drain the RCS, the cold leg balance line begins to void (as seen in Figure 1.1-4), the recirculation flow path is broken, and the CMT drains as the water volume is replaced by steam from the cold leg, beginning the draining mode of the CMT. The CMT injection flow rate is larger in this mode because of the greater density difference between the colder CMT water and the steam or two-phase mixture in the balance line.

For a small break, the CMT is in the recirculation mode for an extended period, and there is the potential for a thick, hot liquid layer to exist at the top of the CMT, which will reduce the steam condensation when the CMT transitions into the draining mode. The hot liquid layer can flash as the RCS depressurizes, causing mixing and reducing the effects of condensation in the CMT.

For a larger break, the recirculation period is reduced because the cold leg balance line will void sooner, breaking natural circulation. In these cases, the hot liquid layer in the CMT will be thinner or may not exist.

Since the top of the CMT is connected to the cold leg, the potential for steam to interact with cold CMT liquid is minimized. For nearly all cases, the design of the CMT causes some cold leg recirculation to occur, which will heat the liquid at the top of the CMT. The hotter water at the top of the CMT will reduce the rapid condensation, such that the CMT will drain more easily.

The AP600 design includes a venturi in the direct vessel injection line to reduce the limiting flow area if that line is postulated to fail. The SSAR calculations, presented in Revision 1 of the SSAR,[1] for the double-ended guillotine break of the direct vessel injection line did not have the venturi installed, and this break was the most limiting of the "small breaks" because the large-break area caused a rapid depressurization of the primary system. The rapid depressurization quickly voids the cold leg balance line, such that recirculation is very limited and steam can mix with colder CMT liquid. The addition of the venturi in the direct vessel injection line limits the break area of the vessel side of the DVI line, such that a slower depressurization occurs. Therefore, there is additional time for the cold leg balance line to recirculate and to heat the top of the CMT, and condensation is reduced.

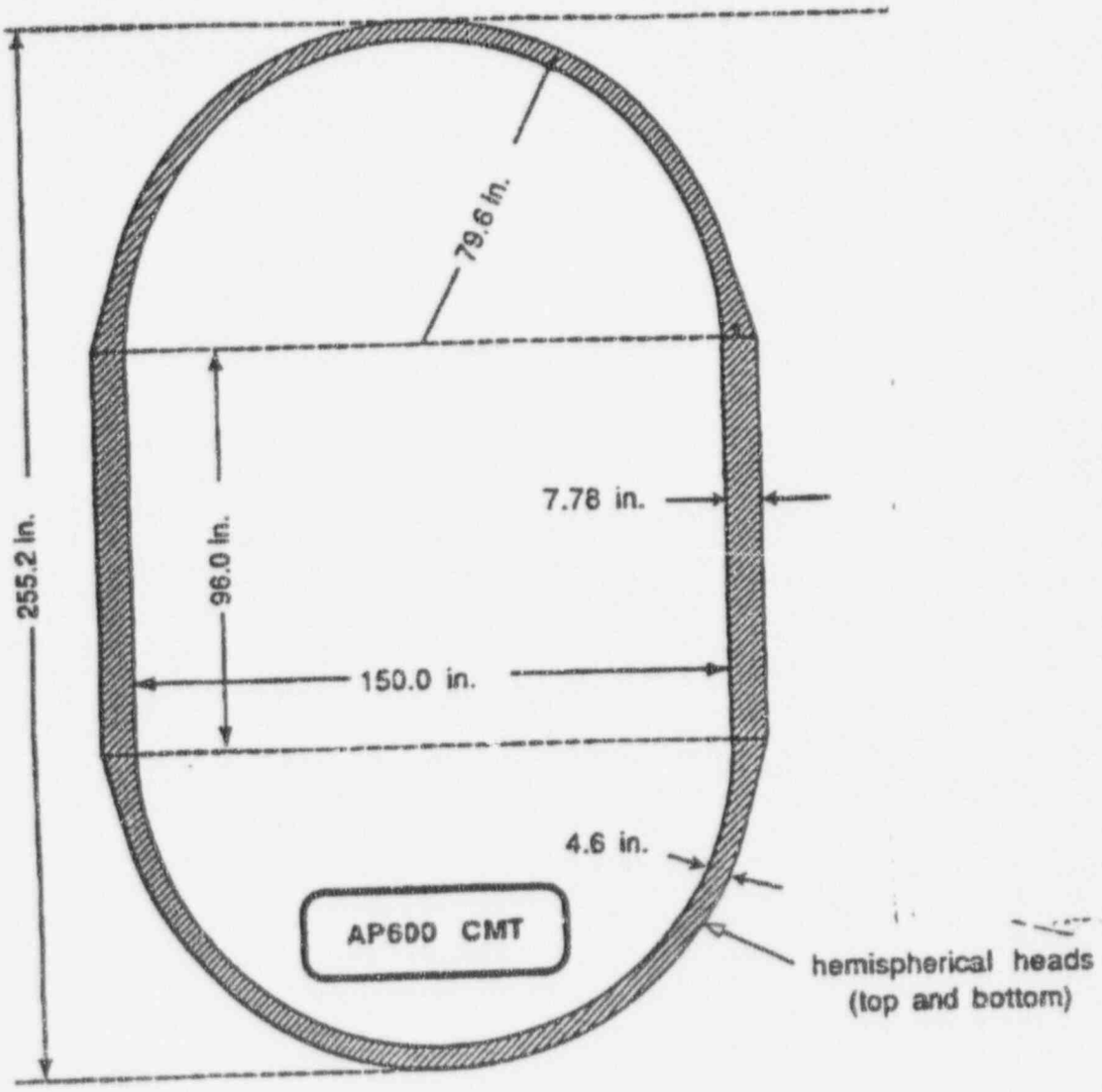

Figure 1.1-1 AP600 Core Makeup Tank

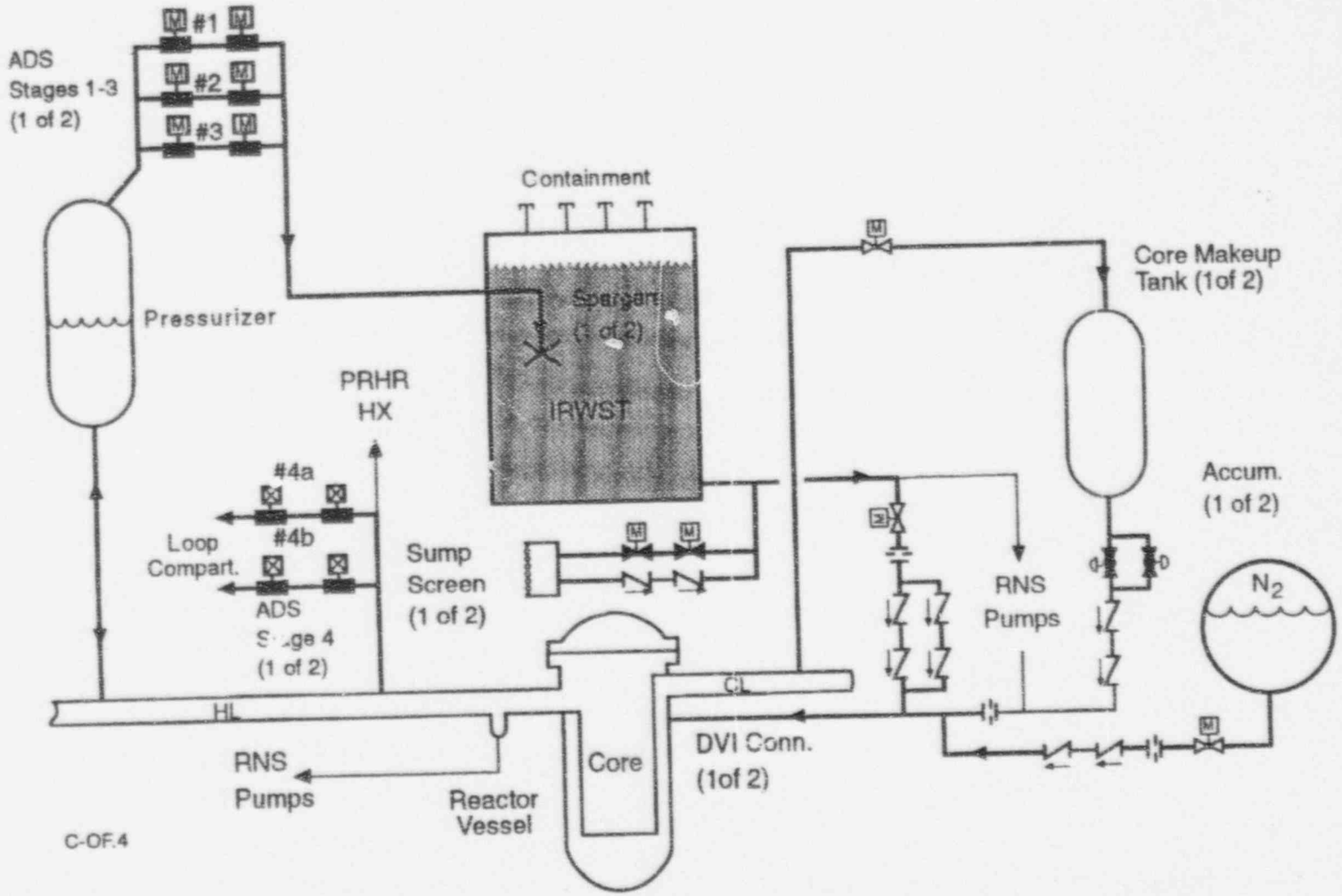

Figure 1.1-2 AP600 Passive Safety System Design

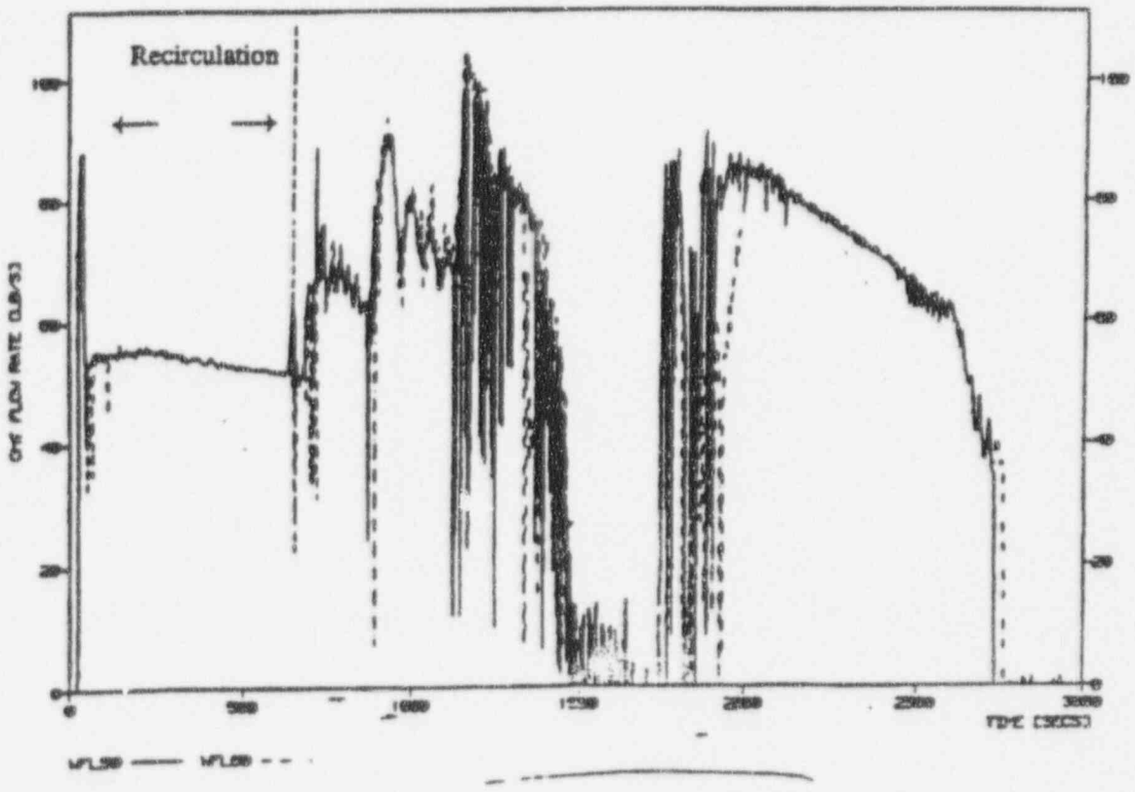

Figure 1.1-3 AP600 SSAR Calculation of CMT Draining Flow for 2-In. Cold Leg Break

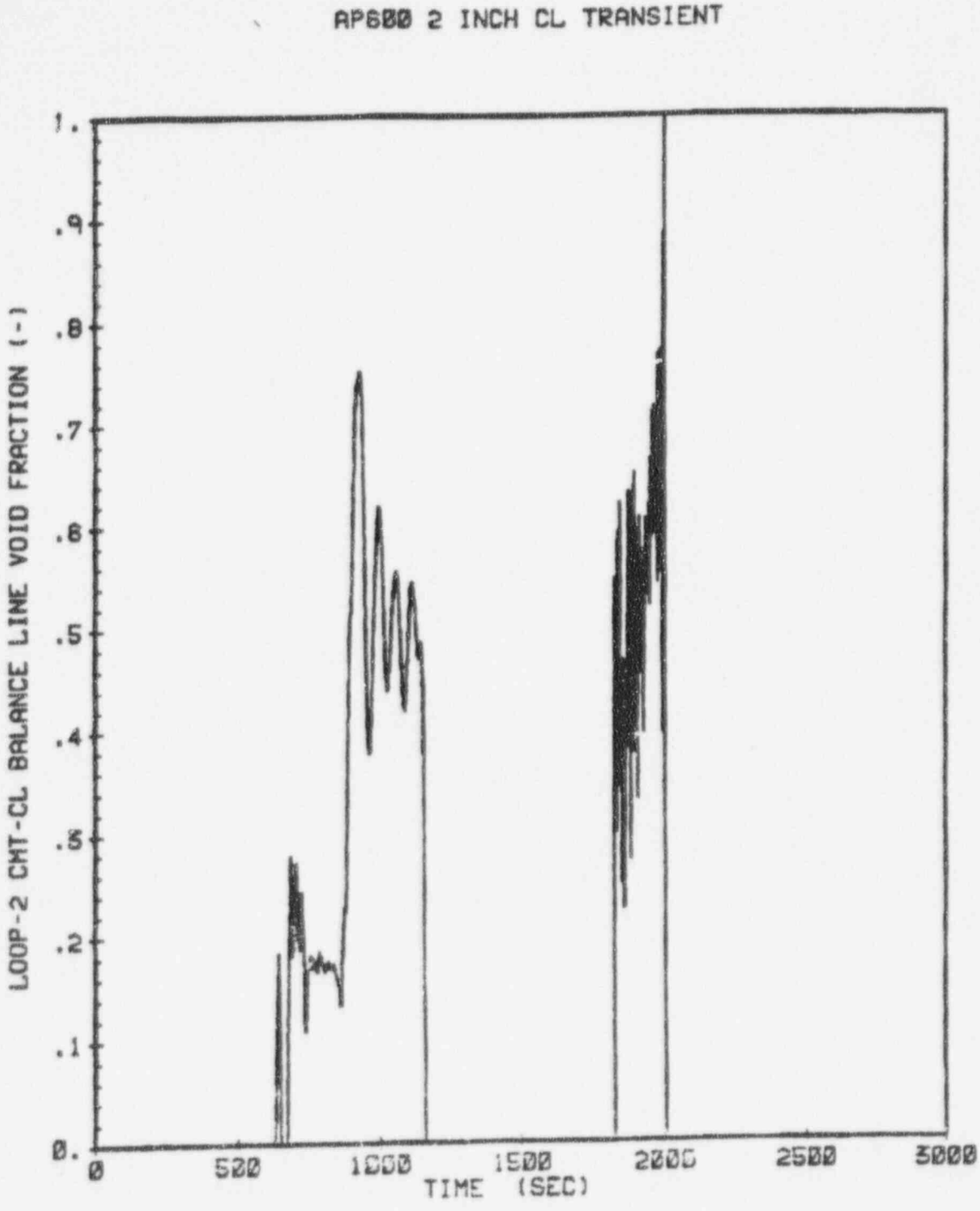

Figure 1.1-4 AP600 SSAR Cold Leg Balance Line Void Fraction for 2-In. Cold Leg Break

1.2 Analysis Objectives

The CMT Scaling Report[2] evaluates the key thermal-hydraulic phenomena that are required to model each type of a transient. Table 1.2-1 provides a phenomena identification and ranking table (PIRT) that indicates the key CMT thermal-hydraulic phenomena that should be modeled for AP600 design basis transients. Both the draining and recirculation phases of the CMT operation require safety analysis computer code validation.

The objective of the CMT test data analysis is to reduce and analyze the separate effects CMT test data to obtain the information on the phenomena listed in Table 1.2-1. The analysis of the data will be used to develop and verify specific heat transfer models in the NOTRUMP, WCOBRA/TRAC, and LOFTRAN safety analysis computer codes. Once verified, these specific models will then be used for the analysis of the SPES and Oregon State University experiments to verify their system response. After the validation, these codes will be used to assess the performance of the AP600 passive safety systems.

The instrumentation used on the CMT tests was designed to provide thermal-hydraulic data that could be used to develop and verify safety analysis computer codes for the AP600. The methods of data reduction and analysis are described in Section 2.0, whereas the results of applying these analysis methods to the data are described in Section 3.0, and the application of the data to thermal-hydraulic models and modeling is described in Section 4.0.

TABLE 1.2-1
PHENOMENA IDENTIFICATION AND RANKING TABLE (PIRT) FOR THE AP600 CMT

Phenomena	LBLOCA	SBLOCA	MSLB	SGTR
CMT Draining Effects				
• Condensation on cold thick steel surfaces	H	H	L	L
• Transient conduction in CMT walls	H	H	L	L
• Interfacial condensation on CMT water surface	H	H	M	M
• Dynamic effects of steam injection and mixing with CMT liquid and condensate	H	H	M	M
• Thermal stratification and mixing of warmer condensate with colder CMT water	H	H	M	M
CMT Recirculation				
• Natural circulation of CMT and cold leg balance leg	L	H	H	H
• Liquid mixing of cold leg balance leg, condensate, and CMT liquid	L	H	H	H
• Flashing effects of hot CMT liquid layer	L	H	L	L
• CMT wall heat transfer	L	M	M	M

L = Low Importance
M = Medium Importance
H = High Importance

1.3 CMT Test Matrix

There were four series of tests that were performed in the CMT separate effects test program.

The 100-series tests were designed as wall condensation tests at different pressures, with and without the effects of noncondensible gases. These data have been analyzed to obtain the local wall condensation heat transfer coefficients and have been compared to existing correlations in the literature. The test matrix for these tests is given in Table 1.3-1.

The 300-series tests investigated the mixing effects of steam from the cold leg balance line condensing in the initially cold water in the CMT and the resulting effects on the CMT drain rate. These tests simulated the effects of a very large small-break or a large-break LOCA since there is no recirculation period simulated that would heat the CMT liquid at the top of the CMT. The test matrix for these tests is shown in Table 1.3-2.

The 400-series tests investigated the steam mixing and CMT drain behavior with a superimposed depressurization transient. Therefore, items of interest were the development of the axial temperature distribution in the CMT and how the tank drained with the depressurization. The test matrix for these tests is given in Table 1.3-3.

The 500-series tests investigated the recirculation behavior of the CMT and the balance lines. The tests were allowed to recirculate until a fraction of the tank was heated to the cold leg balance line temperature. At that time, steam was allowed to enter the balance line, and the tank was drained during depressurization. These tests more accurately simulate the expected conditions for the CMT following a postulated small-break LOCA. The test matrix for these tests is given in Table 1.3-4.

The analyses of the data from these different series of tests are contained in this report and will be used to assess the CMT models in the NOTRUMP, WCOBRA/TRAC, and LOFTRAN AP600 safety analysis computer codes.

TABLE 1.3-1 100-SERIES TEST MATRIX					
Nominal Pressure (psig) --->	**10**	**135**	**685**	**1085**	**2235**
Air Partial Pressure (psi)					
0	C047101*	C078102	C079103	C042104	C002105
0.2	C044106				
1.	C045107				
2.	C046108				

*Specific CMT test run number.

TABLE 1.3-2 300-SERIES TEST MATRIX					
Nominal Pressure (psig) --->	**10**	**45**	**135**	**685**	**1085**
Nominal Drain Rate (gpm)					
6	C037301	C048317	C036302	C051320	C038303
11	C027304	C049318	C080305	C052321	C029306
16	C031307	C050319	C034308	C053322	C039309
17	C032310		C033311		
24				C054323	

TABLE 1.3-3 400-SERIES TEST MATRIX		
Test Number	**Pressure (psig)**	**Depressurization Rate (psi/sec)**
C055401	1085	1
C056402	685	1
C057403	685	2 to 3
C058404	685	0.5

TABLE 1.3-4
500-SERIES TEST MATRIX

Test Number	Pressure (psig)	Depressurization Rate (psi/sec)	Initial Drain Rate (gpm)
C059502	1085	N/A	16
C061504	1085	N/A	16
C064506	1085	N/A	16
C065506	1085/685*	1.5/0.5*	16
C066501	1085	N/A	6
C067501	1085/685*	1.5/0.5*	6
C068503	1085	N/A	6
C069503	1085/685*	1.5/0.5*	6
C070505	1085	N/A	6
C071505	1085/685*	1.5/0.5*	6
C072509	1835	N/A	16
C073509	1835/685**	1.5/0.5**	16
C074508	1835	N/A	16
C075508	1835/685**	1.5/0.5**	16
C076507	1835	N/A	16
C077507	1835/685**	1.5/0.5**	16

* Initial steam pressure of 1085 psig. Initial depressurization rate of 1.5 psi/sec. When steam pressure reached 685 psig, the depressurization rate was reduced to 0.5 psi/sec.

** Initial steam pressure of 1835 psig. Initial depressurization rate of 1.5 psi/sec. When steam pressure reached 685 psig, the depressurization rate was reduced to 0.5 psi/sec.

2.0 CMT ANALYSIS METHODOLOGY

2.1 Analysis Modeling Introduction

Detailed data analysis methods were developed to evaluate 100- and 300-series tests. Some methods apply to both types of tests, while others are tailored for each test type. Sections 2.2 through 2.8 provide a description of these methods and the differences between analyses of the 100- and 300-series tests. To enhance understanding, these sections provide detailed results for two specific tests: C047101 and C053322. The tests and related plots were selected to provide representative discussions for all 100- and 300-series tests.

Analysis of the 400- and 500-series tests were limited to the use of methods developed for the 100- and 300-series tests as appropriate. The application of these methods to the 400- and 500-series tests is discussed in Section 2.9.

Key differences that impact the analyses of the four test types are shown in Table 2.1-1. The primary difference between 100- and 300-series tests is the initial water level and variations in the water level. The 400-series tests extend the 300-series tests by adding depressurization. The 500-series tests extend the 400-series tests by adding recirculation prior to draindown.

TABLE 2.1-1 COMPARISON OF TEST SERIES				
	100	**300**	**400**	**500**
Initial Water Level	nearly empty	full	full	full
Final Water Level	nearly empty	nearly empty	nearly empty	nearly empty
Test Part 1				recirculation
pressure	N/A	N/A	N/A	constant
inlet flow	N/A	N/A	N/A	hot liquid
level change	N/A	N/A	N/A	none
Test Part 2		draindown	draindown	draindown
pressure	constant	constant	depressurizes	depressurizes
inlet flow	steam	steam	steam	steam
level change	limited change	drains	drains	drains

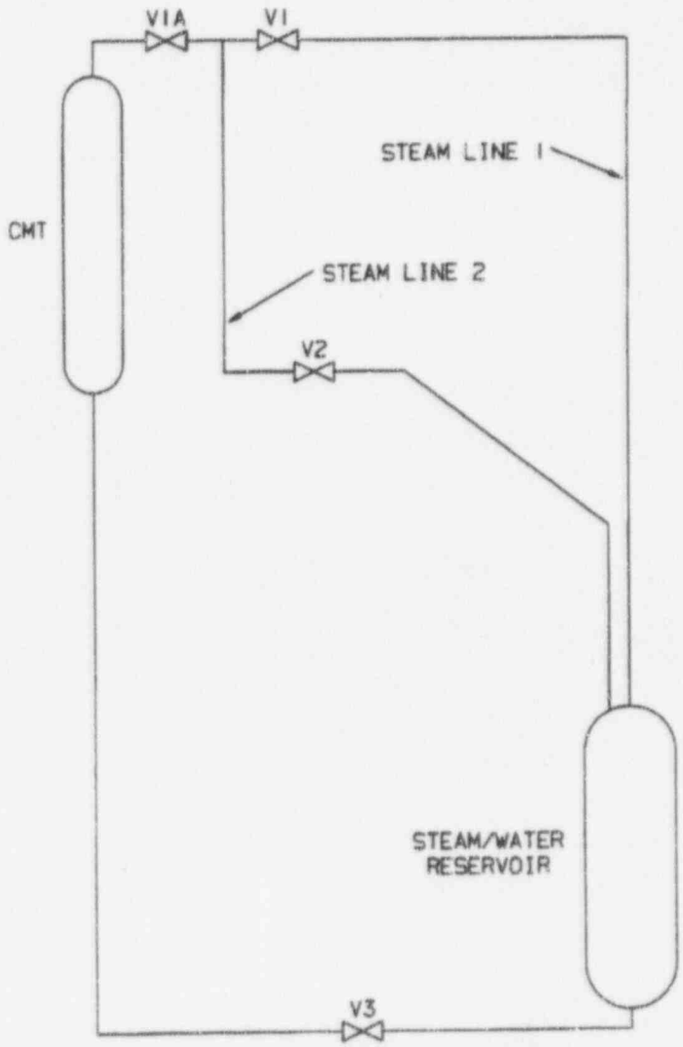

Figure 2.1-1 CMT Test Control Valves

2.2 Facility Characterization

The characteristics of the test facility components, instrumentation, and piping runs were determined for use in the analysis. The key facility characteristics are:

Thermocouples: Thermocouple and thermocouple data channel calibrations were performed.[3] The results of these measurements were fitted with a different quadratic function of apparent temperature for each thermocouple. From recorded temperatures, the best-estimate temperatures used in the analyses are found using these functions.

Discharge Line Flowmeters: Correction curves were measured for the discharge line turbine flowmeters FM1 and magnetic flowmeter FM6.[3] These curves were used in the analyses to obtain the best-estimate flow for each instrument, along with a test-specific bias on FM6 based on the initial no-flow condition. Flow correction curves used are given in Appendix A.

Steam Line Pressure Losses: During cold and hot pre-operational tests, water was pumped at various rates through the steam lines. Curves of pressure loss factors across various sections of the steam lines versus flow Reynolds number for liquid flow were measured.[3] This information was used in the matrix test analysis to supplement the measurement of steam line flow. The DP cells used for this purpose and their tap locations are:

PDT8	From just above the steam/water reservoir to upstream of the steam line 1 isolation valve V1 (actually two cells, PDT8A and PDT8B, with opposite polarity)
PDT11	From upstream of the steam line 1 isolation valve V1 to just above the CMT top nozzle
PDT13	From just above the CMT top nozzle to inside the top of the CMT

Pressure loss factor curves used are given in Appendix A.

CMT Region Volumes: During cold pre-operational tests, water was drained from the CMT and weighed, and weight versus water level was recorded.[3] These data were used with nominal geometric data to determine the best-estimate CMT cylindrical inner diameter, cross-sectional area, and interior volume versus elevation needed for mass balance calculations.

CMT Wall Thermal Properties: Samples of the pipe from which the CMT wall cylindrical section was made were tested to determine thermal diffusivity, using a laser flash diffusivity apparatus, and specific heat capacity, using a differential scanning calorimeter, as functions of temperature.[4] These functions were used in the calculation of wall inner surface heat flux from measured wall temperatures. Thermal property curves used are given in Appendix A.

2.3 Flow Calculations

This section discusses methods of calculating mass flow rates in the steam line and CMT discharge line.

Discharge Line Flow: For those tests with FM6 installed in the horizontal section of the CMT discharge pipe, FM6 was used in the analyses to determine the best-estimate flow because of its sensitivity to low flow rates. In the other tests, the turbine flowmeter FM1 was used for volume flow. Fluid density is based on drainline fluid temperature and CMT pressure.

Steam Line 1 Flow: The method of determination of steam line 1 flow is outlined here and described in detail in Appendix B.

One of the bases of the analysis method is to allow the calculation to proceed even if certain instrument signals are absent or temporarily out of range. Thus, as shown in Appendix B, there are choices between different sources for data, such as either the measured atmospheric pressure or a constant if that signal is missing. In practice, the base measurements were almost always available. If certain instruments were over-ranged or under-ranged during part of a transient, redundant instruments were used in their place.

The vortex flowmeter FM4 in the vertical section of steam line 1 above the steam/water reservoir (S/WR) was used for the primary measurement of steam line 1 flow. The indicated volume flow was converted to mass flow using the pressure and temperature indicated by PT7 and TC72A, respectively, located at the flowmeter. To determine the validity of the FM4 flow, the formula for the lower bound of accurate measurement specified by the manufacturer was used, as was the upper range limit of volumetric flow recorded in the test notes.

If the flow was outside the valid range of FM4, steam line pressure drop information was used instead. Values for steam line 1 flow were determined independently from each of the pressure drop channels PDT8, PDT11, or PDT13, as follows.

For each PDT, the applicable fluid density and viscosity were determined using the enthalpy of fluid (usually dry saturated steam) calculated from the pressure and temperature in the top of the S/WR and an average pressure over the span measured, assuming homogeneous flow in the pipe.

Pressures and pressure losses were calculated from PT and PDT gage readings accounting for the reference leg height, which is assumed to contain water at measured room temperature and system pressure; measured atmospheric pressure; and elevation head of the flowing fluid.

For PDT8 and PDT13, measured pressure drop was biased by a constant, determined for each test, which was the average calculated pressure loss during an initial period of assumed zero flow. The time period was determined for each PDT span based on the positions of steam line

1 valves and the discharge valve V3. The valve positions, in turn, were based on the start time recorded in the test notes and (usually) assumed opening times, with time margins allowed for uncertainty. The tests were performed in such a way as to obtain valid time periods for this purpose. PDT11 is not biased in this way because it spans valves V1 and V2, which are usually only opened at about the time of initiation of steam line flow.

The total pressure loss factor versus Reynolds number determined from pre-operational tests, shown in Appendix A, is used in an iterative search for flow rate for each recorded time, using the Bernoulli equation.

Each steam line flow calculation based on pressure drop is invalidated when either:

- A valve, within the measured span, is not fully open
- Valves in both steam lines 1 and 2 are open, except for the steam distributor pressure drop PDT13
- The indicated pressure difference is out of the instrument range, i.e. either negative or greater than its upper range limit indicated in the test notes

Best-estimate steam line flow, which is used as the flow into the CMT for any other calculations, was selected from the first valid calculated flow using instruments in this order of priority:

FM4 PDT13 PDT8 PDT11

In conducting each test, an attempt was made to select the instrument spans for a test in such a way that FM4 measures the high range, PDT13 measures flow in the lowest range, FM8 overlaps both FM4 and PDT13, and PDT11 is a backup.

An example of the application of this method is given for a typical 300-series test in Figures 2.3-1 through 2.3-4. Time is measured relative to the start of the opening of discharge valve V3. Figure 2.3-1 shows the recorded readings of FM4 flow rate and the differential pressures PDT13 and a combination of PDT8A, PDT8B, and PDT11. Before steam line valves V1 and V1A both open, PDT11 is over-ranged due to the difference between the reservoir side and the CMT side of the steam and drain valves. During the period of maximum flow after discharge valve V3 is opened, PDT13 is obviously over-ranged, but other instruments are well within range (FM4 upper range is 40 $ft.^3$/min for this test). When the high steam flow period ends, FM4 drops out as flow briefly goes below its range of sensitivity. As the flow tapers off at the end of the test, FM4 drops out again, and other pressure drops are very small compared to their ranges. Finally, valve V3 is closed, the system is depressurized, and flow approaches zero again.

Figure 2.3-2 shows the mass flow calculated for each of the four instruments as a dashed line, each compared to the best-estimate flow (solid line) selected from different measurements at different times.

FM4 is used as the best estimate when it is within range. PDT13 and FM8 agree well with FM4. PDT11 agrees well at high flow, but is increasingly low at lower flows, characteristic of a negative bias on pressure difference. Figure 2.3-3 shows, for each instrument, the period during which its flow was considered valid. On this plot, a value of 1 indicates validity, and 0, invalidity. This run is unusual in that all indicators are considered valid for most of the transient, with the exceptions already noted.

Figure 2.3-4 shows the integrated values of all flows, including the best estimate. The curves are for best estimate, FM4, PDT13 (steam line 1), PDT8 (steam line 1, up-stream of valves), and PDT11 (steam line 1, down-stream of valves). The curves differ most during the period of high flow when PDT13 is out of range; after that the previous observations hold. The bottom plot of Figure 2.3-4 indicates which indication was used for the best-estimate flow, with a value of 4 indicating FM4, 8 being FM8, 11 being FM11, and 13 being FM13. As previously observed, FM4 was used over most of the periods of significant flow, with PDT13, the second choice, filling most of the remainder, and PDT 8 used only in the initial period before the valves are fully open.

Figures 2.3-1 through 2.3-4 are not included in the non-proprietary version of this document.

2.4 CMT Level and Mass Balance

The CMT level and mass calculations employ two sets of instruments: DP cells and thermocouples. The DP cells and CMT fluid thermocouples are shown in Figure 2.4-1. The level and mass are determined by using these instruments to determine the pressure gradient in the CMT, as shown in Figure 2.4-2.

The DP cells provide differential pressures over their spans. The readings are corrected for the elevation head in vertical connecting tubing (reference legs) to provide differential pressures as a function of elevation over the total span of DP cells. Either the combination of narrow-range cells or the wide-range cell can be used to determine levels.

The 39 fluid thermocouples are grouped in to 32 elevations. Steam and liquid densities for each of these elevations were determined based on pressure tap PT5. Differential pressures for a given water level are determined by using integration cells centered around the 32 elevations. Temperatures are assumed uniform in the cells. The differential pressure for a given water level can then be determined by integration of the density.

The level for a specific test time is determined by equating the differential pressures:

$$\Delta P_{DP\ cells} = \int_{bottom\ DP\ tap}^{level} \rho_{\ell}\,(P,T)\,dx + \int_{level}^{top\ DP\ tap} \rho_{v}\,(P,T_{sat})\,dx \qquad (2.4\text{-}1)$$

where:

$\Delta P_{DP\ cells}$	=	differential pressure over total span of DP cells
$\rho_{\ell}\,(P,T)$	=	liquid density
$\rho_{v}\,(P,\ T_{sat})$	=	steam density

A sample plot of the calculated level using each of the narrow-range and wide-range DP cells is shown for a 100- and 300-series test in Figures 2.4-3 and 2.4-4, respectively. As shown in the figure, the narrow-range and wide-range cells are generally consistent. Results provided in this report are exclusively based on the narrow-range cells.

Figure 2.4-3 shows the behavior of the DP cells for test C047101. Figure 2.4-4 also exhibits the two distinct draining periods of 300-series tests: a rapid condensation and mixing period that reduces the drain flow and a free gravity drain period. Only limited draining occurs during the period as steam is condensing and the water at the top of the CMT is heated. Drain rate, as shown by the slope of the

level curve, is relatively constant during the drain period. Performance of the DP cells tends to be erratic during the condensation period, and very stable during the gravity drain period.

The vapor and liquid mass in the CMT for a time t is then determined by:

$$M_v = \sum_{\text{fluid TCs}} \rho_v \, (P,T_{sat}) \, \Delta V_{vap} \qquad (2.4\text{-}2)$$

$$M_\ell = \sum_{\text{fluid TCs}} \rho \, (P,T) \, \Delta V_{liq} \qquad (2.4\text{-}3)$$

where:

M_v = steam mass
M_ℓ = liquid mass

The mass balance for a specific test time is determined by comparing the current mass in the CMT to an expected mass based on the initial mass and the inlet and outlet flows. The flow rates are discussed in Section 2.3.

The integrated steam inlet flow at time t is defined by:

$$M_{v\text{-}in_t} = \int_{t_o}^{t} W_{in} \, dt \qquad (2.4\text{-}4)$$

where:

W_{in} = steam inlet flow rate
$M_{v\text{-}in_t}$ = integrated steam inlet flow at time t

The integrated liquid outlet flow at time t is defined by:

$$M_{\ell\text{-}out_t} = \int_{t_o}^{t} W_{out} \, dt \qquad (2.4\text{-}5)$$

where:

W_{out} = liquid outlet flow rate

$M_{l\text{-}out_t}$ = integrated liquid outlet flow at time t

The mass balance error is defined as the excess mass in the CMT. The mass balance error for a time t is:

$$\text{mass balance error}_t = \left[M_{v_t} + M_{l_t}\right] - \left[M_{v_{t_0}} + M_{l_{t_0}}\right] - \left[M_{v\text{-}in_t} + M_{l\text{-}out_t}\right] \qquad (2.4\text{-}6)$$

The mass balance error sensitivities to changes in measured data are shown below.

Change in Measured Value	**Effect on Calculated Mass Balance Error**
Increase steam inlet flow	More negative
Increase liquid outlet flow	More positive
Increase calculated initial CMT level	More negative
Increase calculated current level	More positive

A sample mass balance error plot for a series 300 test is shown in Figure 2.4-5. The integrated inlet and outlet flows and a corresponding level error are also shown. With a height of ~115 in. and a volume of ~1100 lb of water, the cylindrical portion of the CMT contains ~10 lb per in. of water. Thus, the mass balance error can be converted to level error as shown in Figure 2.4-5.

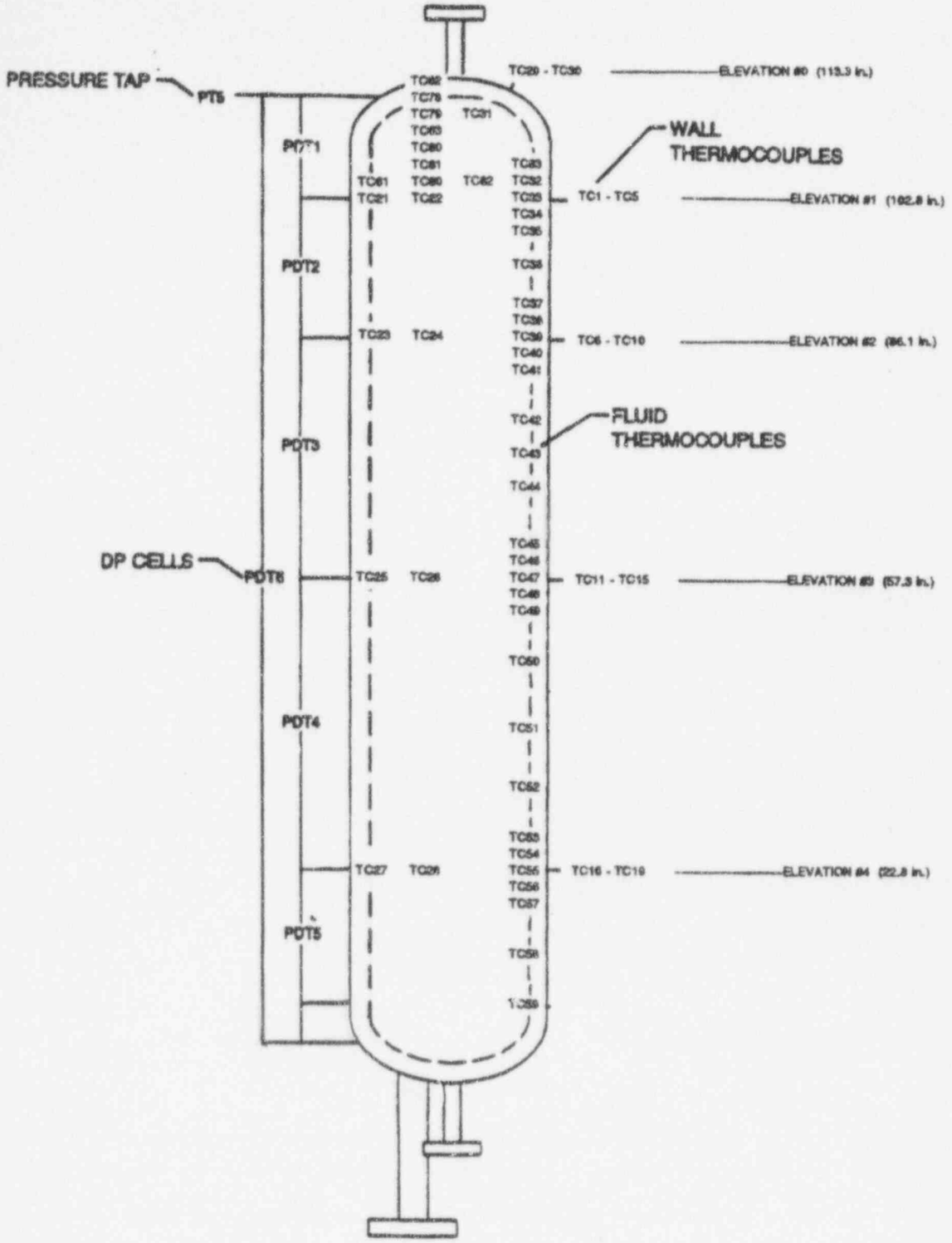

Figure 2.4-1 CMT DP Cells and Thermocouples

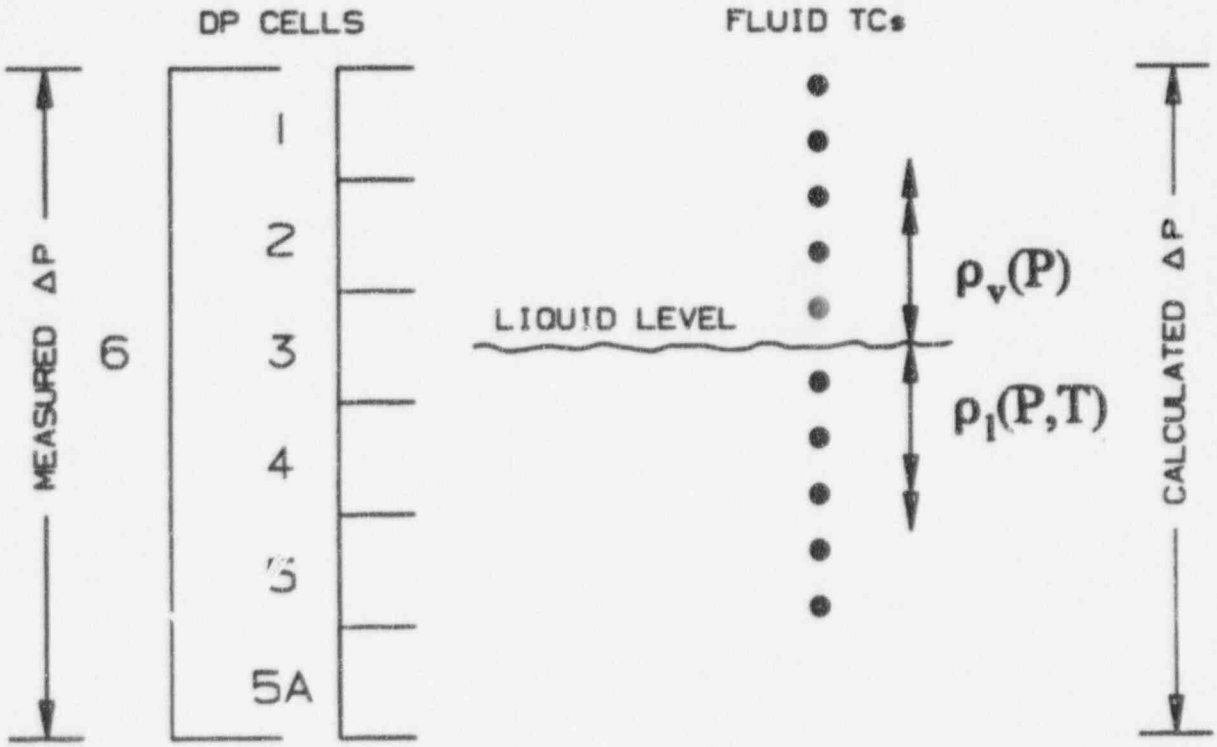

Figure 2.4-2 CMT Level and Mass Modeling

Figures 2.4-3 through 2.4-5 are not included in the non-proprietary version of this document.

2.5 CMT Local Heat Transfer

The CMT is instrumented for wall heat transfer calculations at five elevations, as shown in Figure 2.4-1. Each of these analysis elevations has one fluid thermocouple and between two and five wall thermocouples. The elevations were selected to provide data over the length of the CMT.

All elevations have thermocouples located on the inside and outer surfaces. As shown in Figure 2.5-1, the inside-surface thermocouple is approximately flush with the inside surface, whereas the other thermocouples are located relative to the outside surface. Wall thickness measurements were employed during manufacture to accurately position the thermocouples. This analysis employs nominal thermocouple locations, which includes an inside-surface location of 1/2 of the thermocouple wire diameter.

A sensitivity study of local heat transfer to the positioning of the thermocouples and the wall thickness is provided in Appendix D. Changes in wall thickness, thermocouple positioning, and properties at the surface are shown to have a small effect on heat flux.

An inverse conduction heat transfer analysis was performed using a version of the CONTA program,[5] which had been modified to include radial coordinates, heat generation, and an annular geometry. This version of the program is called CONTRA. The wall is modeled as a one-dimensional cylinder with an outside boundary condition defined by a thermocouple. The wall geometry in the elliptic head is approximated.

The analysis method selects a heat flux on the inside surface to best fit the wall thermocouple data. The inside surface temperature is also calculated. The heat transfer coefficient is then calculated using the fluid thermocouple and the calculated surface temperature.

The initial water levels of the 100- and 300-series tests directly impacted the local heat transfer. The 100-series tests started with a water level well below the lowest wall heat transfer analysis elevation; steam reached these elevations with very little delay after the start of the test. The 300-series tests started with the water level above the top analysis elevation; steam reached the elevations with the systematic delay due to draining. The effects of these differences are addressed below.

These analysis methods can also be applied to 400- and 500-series tests. The impact of the water level on local heat transfer is addressed in Section 3.0.

2.5.1 100-Series Local Wall Heat Transfer

A representative 100-series test was selected. The plots for this test are shown in Figures 2.5-2 through 2.5-8 and are typical of the 100-series tests.

Fluid and wall thermocouple data for the five elevations are shown in Figure 2.5-2. Measured temperature gradients between the fluid and surface thermocouple and between the surface and

adjacent wall thermocouples are shown in Figure 2.5-3. Gradients for only the three intermediate elevations are shown in Figure 2.5-3, because the top elevation has only two thermocouples and the bottom elevation had a defective inside surface thermocouple. The deflective thermocouple is not shown in Figure 2.5-1.

Calculated heat flux and surface temperature for the five analysis elevations are shown in Figures 2.5-4 and 2.5-5, respectively. No elevation-dependant time delay is evident; significant heat transfer started at all elevations shortly after the CMT steam supply and drain valves were opened. The heat flux curves also exhibit the same shape and trends, rising very quickly to a peak and then gradually declining.

Differences between analysis elevations can be further explored by overlaying heat flux of adjacent elevations, as shown in Figure 2.5-6. The heat flux curves are clearly similar. As a function of elevation, the peak heat flux is shown to decrease with decreasing elevation with minor increasing delay with decreasing elevation. Overall, the heat flux curves have the same characteristics; these curves can be viewed as a family of curves with some elevation dependance.

Measured fluid temperature and calculated saturated steam temperature for the analysis elevations are shown in Figure 2.5-7. The saturated steam temperature was calculated from the CMT pressure tap, PT5. The fluid thermocouples are located ~3 in. from the wall and clearly tracked the steam temperature shortly after the valve opened. The observation that these thermocouples were exposed to steam is consistent with the water level, which was well below the lowest analysis elevation.

Calculated wall temperatures for the analysis elevations are compared in Figure 2.5-8. These curves also have the same characteristics and can be viewed as a family of curves with some elevation dependance.

Therefore, the data indicate:

- heat flux and wall temperatures are from a family of curves with some elevation dependance
- the fluid is saturated steam

The ability to extend these trends from the analysis elevations to the entire CMT wall is explored in Section 2.6.

2.5.2 300-Series Local Wall Heat Transfer

A representative 300-series test was selected for this discussion. The plots for this test are shown in Figures 2.5-9 through 2.5-18 and are typical of 300-series tests.

Fluid and wall thermocouple data for the five analysis elevations are shown in Figure 2.5-9. Measured temperature gradients between the fluid and surface thermocouple and between the first two wall thermocouples are shown in Figure 2.5-10. Gradients for only the three intermediate elevations are

shown in Figure 2.5-10, because the top elevation has only two thermocouples and the bottom elevation had a defective inside surface thermocouple.

A CMT level plot with the analysis elevations and uncovery times identified is shown in Figure 2.5-11. The uncovery time is the time the water level reaches an elevation.

Calculated heat flux and surface temperature for the five analysis elevations are shown in Figures 2.5-12 and 2.5-13, respectively. Both heat flux and surface temperature show a clear elevation dependance. The uncovery times are also shown in the figures. Relative to the uncovery times, these curves are very similar; the times shifts are time delays associated with the water level.

The axial heat flux profile is related to heat flux at the analysis locations as shown in Figure 2.5-14. The axial profile follows the decreasing water level, and its vertical movement maps into, and from, the time delay.

Differences between analysis elevations can be explored by time shifting and overlaying heat flux of adjacent elevations, as shown in Figure 2.5-15. The heat flux curves are clearly similar and can be viewed as a family of curves with the time shifting adjustment and with some elevation dependance.

Time-shifted calculated wall temperatures for all analysis elevations are shown in Figure 2.5-16. As with heat flux, these curves can be viewed as a family of curves with the time-shifting adjustment and with some elevation dependance.

Measured fluid temperature and calculated saturated steam temperature for the analysis elevations are shown in Figure 2.5-17. Fluid thermocouples clearly track the steam temperature shortly after the uncovery time.

Thus, the general trends are a family of curves for heat flux wall temperatures time shifting due to water level and with some elevation dependance, and the fluid above the water level is saturated steam. The ability to extend these trends from the analysis elevations to the entire CMT wall is explored in Section 2.6.

The heat flux curves of Figure 2.5-12 also exhibit three characteristic regions: an initial period of inactivity, a period of moderate heat flux just before the uncovery time when exposed to water, and a final period of high heat flux when exposed to steam. The period of moderate heat flux is attributed to two effects: heating at the top analysis elevation, which is in the top head, during the condensation period before the water level began to drop, and a mixing layer of heated water. The ability to extend these trends from the analysis elevations to the entire CMT wall is explored in Section 2.6.

The existence and depth of the mixing layer can be determined by investigating the measured fluid temperatures as a function of elevation. Figure 2.5-18 plots fluid temperature versus elevation for a series of times during the drain period. As shown in the figure, the mixing depth can be determined by comparing the elevation of the heated region to the water level. The mixing depth of ~1 ft. to 2 ft.

is shown by the gradient of the temperature curves for different times in Figure 2.5-18 and is typical of 300-series tests.

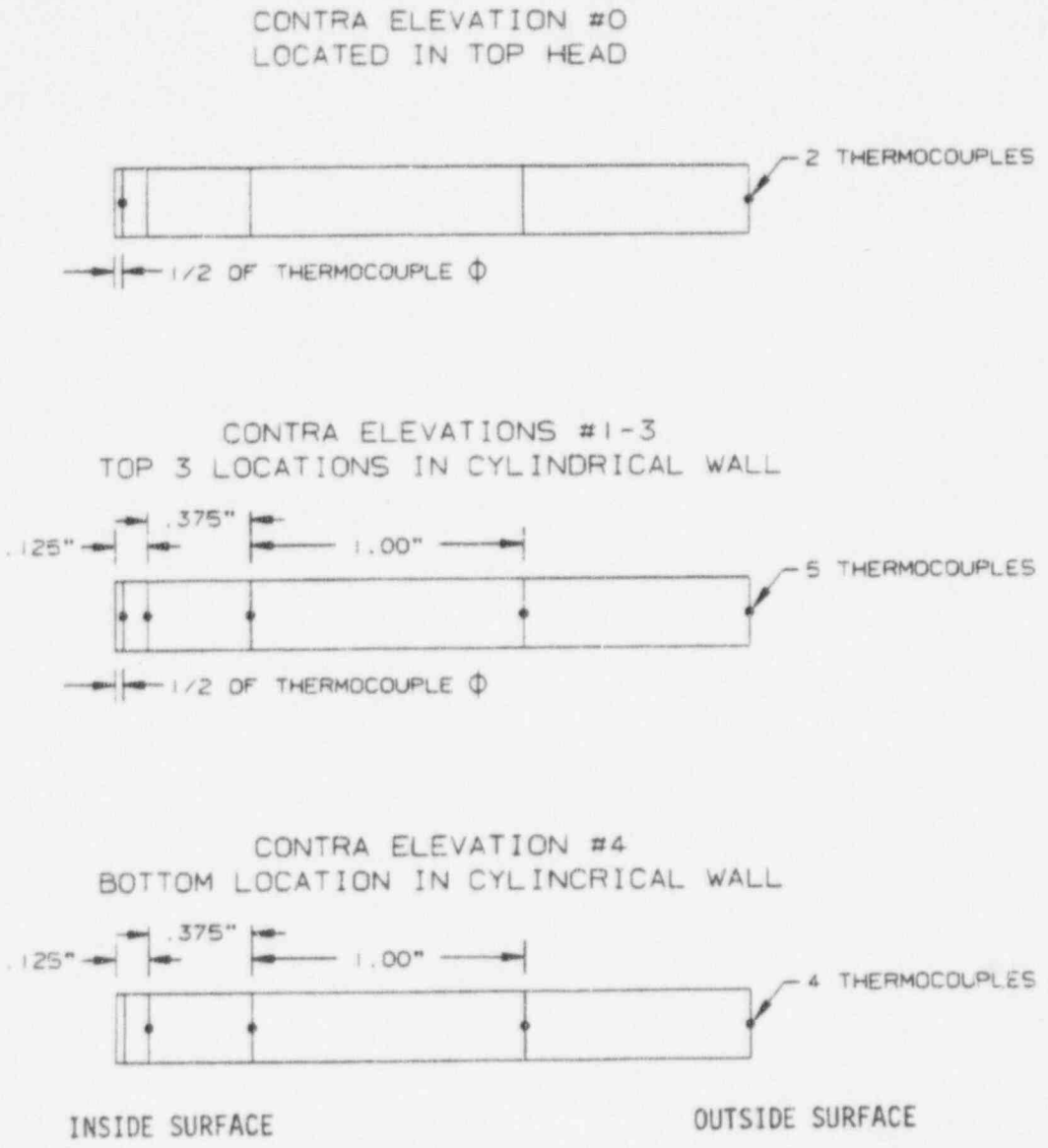

Figure 2.5-1 Local Wall Heat Transfer Modeling

Figures 2.5-2 through 2.5-13 are not included in the non-proprietary version of this document.

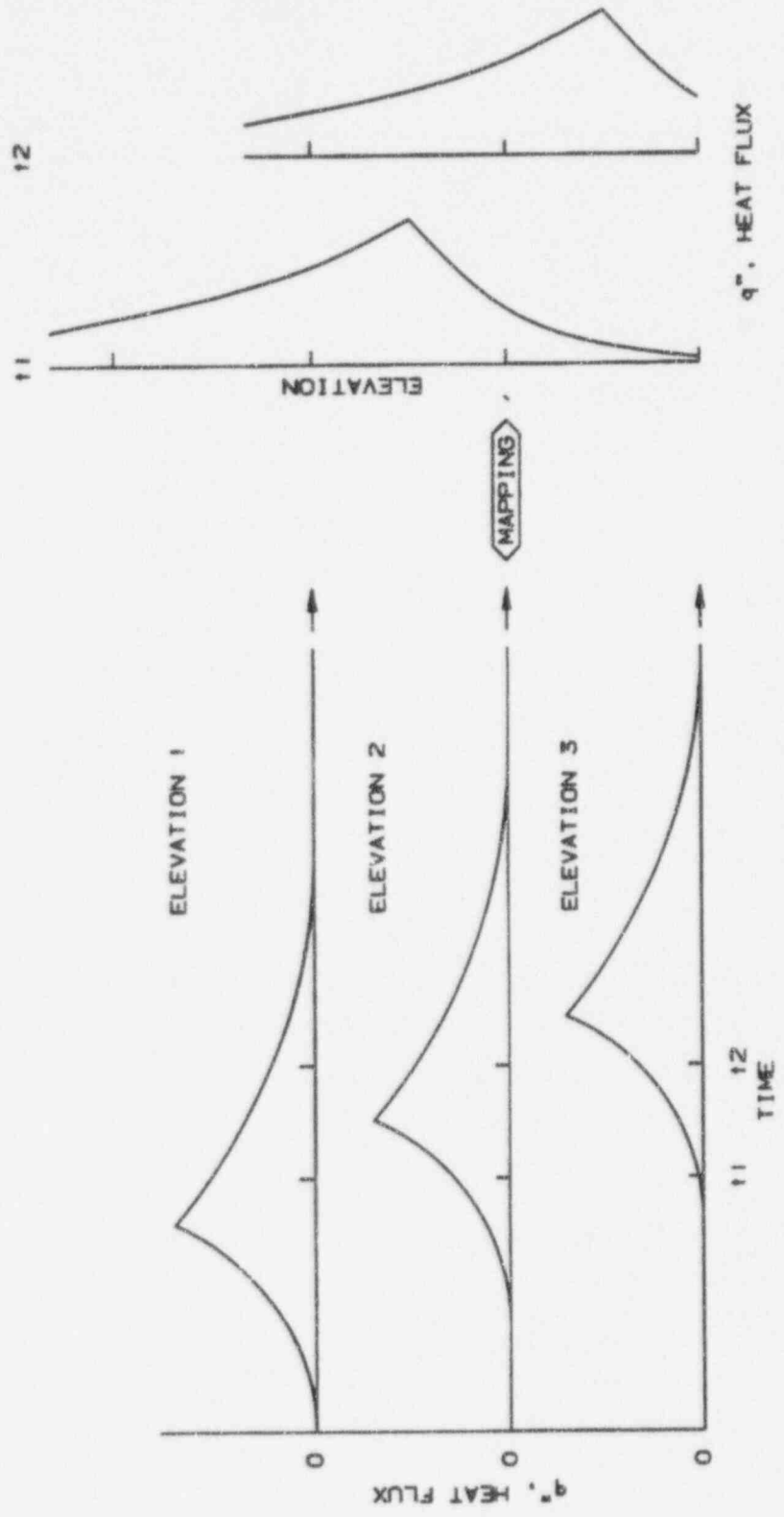

Figure 2.5-14 **Mapping of Heat Flux at Analysis Elevations to and from Axial Heat Flux Profile**

Figures 2.5-15 through 2.5-18 are not included in the non-proprietary version of this document.

2.6 CMT Wall Effects Modeling

This section provides the translation of local wall heat flux and surface temperature into overall effects of vapor wall heat transfer, liquid wall heat transfer, vapor wall heat transfer coefficient, and wall condensation. Section 2.5 demonstrates that wall heat flux and surface temperature can be treated as a family of curves. This family of curves is interpolated and extrapolated to develop the overall effects.

The CMT wall is modeled by subdividing into 366 integration cells, as shown in Figure 2.6-1. Calculations involving heat flux and surface temperature are based on this model. The maximum integration cell size of 1/3 in. was selected to be smaller than the characteristic length of the wall condensation equations of Section 2.7.

The method of determining heat flux and surface temperature at the integration cells for the 100- and 300-series test differs as discussed below. In both cases, interpolation is used to calculate values at the center of the integration cells; the values are then applied uniformly to these cells.

Steam and fluid wall heat transfer is determined by integration of the heat flux at the integration cells. The heat transfer in a cell is subdivided into steam and fluid heat transfer based on the fraction of the cell's wall surface above the water level.

2.6.1 100-Series Test Interpolation and Heat Transfer

The 100-series tests started with a nearly empty CMT; the tests did not provide sufficient heat flux data below the water level to perform fluid region calculations. These calculations are, therefore, limited to the steam region only.

Section 2.5 demonstrates the heat flux and surface temperature curves are from a family of curves and no time shifting is required. Heat flux and surface temperature at the integration cells are determined by using distance-weighted averaging of the nearest analysis elevations. Results at the top analysis elevation are applied uniformly to the region of that elevation. Similarly, results at the bottom analysis elevation are applied uniformly to the region below that elevation.

The steam wall heat transfer for the test discussed in Section 2.5 is provided in Figure 2.6-2.

2.6.2 300-Series Test Interpolation and Heat Transfer

The 300-series tests started with a full or nearly full CMT. The tests provided sufficient heat flux data above and below the water level to perform fluid and steam region calculations.

Section 2.5 demonstrates the heat flux and surface temperature curves are from a family of curves with time shifting based on water level is required. Heat flux and surface temperature at the integration cells are determined by first time shifting the curves for the nearest analysis elevations and then averaging the shifted curves using distance weighting, as shown in Figure 2.6-3. The region below the

lowest water level reached during a test is not evaluated; the region does not experience any steam heat transfer and only minor fluid heat transfer at the end of the test.

The steam and fluid wall heat transfer for the test discussed in Section 2.5 is provided in Figure 2.6-4.

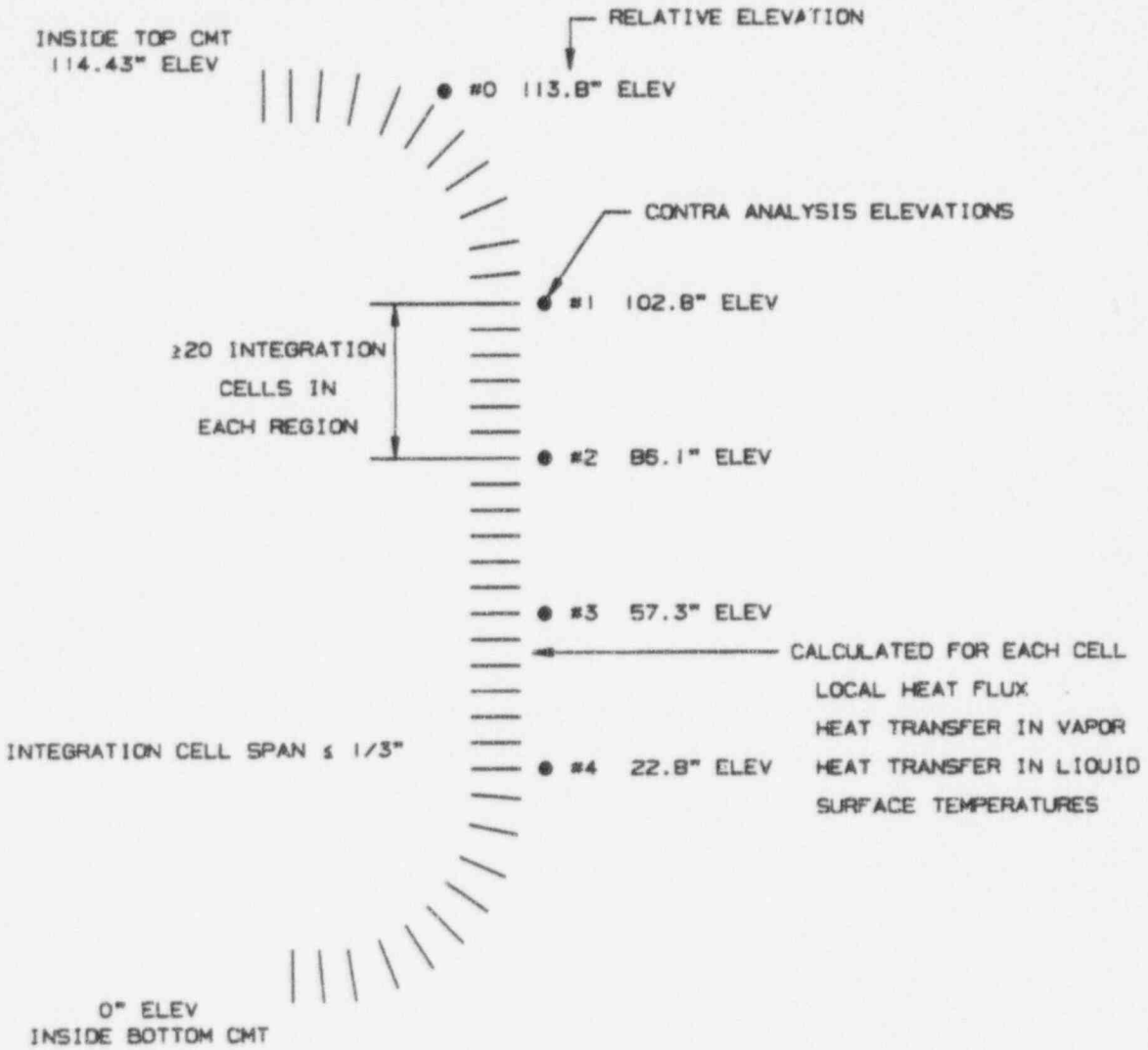

Figure 2.6-1 Modeling of CMT Wall Effects

Figures 2.6-2 through 2.6-4 are not included in the non-proprietary version of this document.

2.7 CMT Wall Condensation

Wall condensation rate is calculated based on wall heat transfer rates, which are calculated from wall temperature measurements at five different elevations in the CMT and interpolated to describe the entire wall surface, as described in Section 2.6. The conversion from heat transfer rate to condensation rate consists simply of dividing the entire wall heat transfer rate at any time by the energy required to be removed from each unit of condensate mass to convert it from steam into condensate ready to run off the wall at the water line. The first approximation to this energy is the latent heat of vaporization; the second approximation would account for the subcooling of condensate at equilibrium between uniform wall and steam temperatures. This section discusses the method of calculation used to apply a third, non-equilibrium approximation. This effect turns out to be a small correction on the much simpler second approximation.

Nusselt[6] made an early evaluation of film condensation on planar and cylindrical surfaces with the following assumptions:

a) flow of condensate in film is laminar
b) film properties are constant
c) subcooling of the condensate may be neglected
d) momentum changes through the film are negligible; there is essentially a static balance of forces
e) the vapor is stationary and exerts no drag on the downward motion of the condensate
f) heat transfer is by conduction only
g) steady-state solution is assumed

A basic result of Nusselt's analysis is an expression of film flow rate as a function of thickness. Film thickness relates to heat transfer directly through assumption (f). Thus, Nusselt also provides closed-form solutions for the local heat transfer coefficient as a function of the film Reynolds number and for the average heat transfer coefficient above the elevation of interest for the case of uniform wall temperature.

In subsequent extensions of this theory, others considered subcooling and non-linear temperature distribution in the condensate film. In converting heat flow to condensate flow, the heat transferred to the wall per unit mass, for which Nusselt used the latent heat of vaporization, should be replaced by the difference between the steam enthalpy and the enthalpy at an intermediate film temperature. Rohsenow[7] showed that this intermediate temperature can be approximated by a temperature that is below the film surface (i.e., saturation) temperature by a factor of 0.68°F of the temperature difference between the film surface temperature and the wall surface temperature. For the transport properties of the fluid used in determining heat conduction and film flow versus thickness, Drew[8] showed that they should be evaluated at a temperature evaluated in the same way but with 0.75 instead of 0.68, whereas Minkowicz and Sparrow[9] arrived at a factor of 0.69.

These existing evaluations of film condensation employ closed-form solutions. This report expands on those methods by employing a numeric solution with a less restrictive assumption specified below.

The assumption of uniform wall temperature was found not to apply strictly to the CMT test conditions, particularly for the 300-series tests. The water level is continually receding, exposing to the hot steam a band of relatively cold wall, which subsequently heats up. To calculate the total condensate flow from the wall into the liquid region at the water level, the enthalpy of the film directly adjacent to the water level must be defined. Because of the sharp wall temperature gradient and fairly high film velocity (on the order of 1 ft./sec), the film temperature may not reach the equilibrium relationship with the steam and adjacent wall temperatures, i.e., the film is warmer than would be expected if the entire wall surface were at the same temperature as the wall surface at the water level.

Consequently, the model used calculates the film temperature and tracks its enthalpy increase as it flows down the wall to the water level. Section 2.6 describes a model of the CMT wall with 366 integration cells and wall heat flux and surface temperature at each of the integration cells in the steam region for both 100- and 300-series tests. This section extends that model and the associated results to calculate film condensation.

The integration cells are modeled as control volumes containing the wall condensation film layer, as shown in Figure 2.7-1. The term definitions are:

T_w	=	wall surface temperature
q_2''	=	wall heat flux
W_{in}, W_{out}	=	film flow rate
T_{fin}, T_f, T_{fout}	=	film temperature
T_g	=	saturated steam temperature
W_c	=	condensation rate for integration cell
q_1''	=	steam-to-film heat flux
A_s	=	wall surface area for integration cell
h_g, H_{in}, h_{out}, h_f	=	enthalpies
u_1 u_2	=	heat transfer coefficients defined in Equations 2.7-5 and 2.7-7

This modeling enhances Nusselt's assumptions as follows:

- Film properties vary, and fluid properties are uniform for each of the integration cell's three boundaries. Average integration cell temperature is used for film properties.

- Steady-state mass and energy balances are used to capture variations in film temperatures.

- Convection heat transfer from the steam to the wall is modeled separately as conduction between the steam and the film associated with condensation and conduction between the film and the wall. The relationship between the two film coefficients is based on existing evaluations of steady-state conditions, i.e., as required to achieve a defined equilibrium film temperature for given steam and wall surface temperatures. This relationship is constant.

Conduction between the steam and film is defined by:

$$q_1'' = u_1 (T_g - T_f) \tag{2.7-1}$$

and the associated condensation rate is:

$$\frac{W_c}{A_s} = q_1'' / (h_g - h_f) \tag{2.7-2}$$

Conduction between the wall and film is defined by:

$$q_2'' = u_2 (T_f - T_w) \tag{2.7-3}$$

With uniform film surface and wall surface temperatures, the heat fluxes are equal, and the average film temperature is defined by:

$$T_f = T_{av} = k\, T_g + (1 - k)\, T_w \tag{2.7-4}$$

Equating the heat fluxes and substituting the average film temperature defines the relationship between the two heat transfer coefficients:

$$u_1 = \frac{k}{1 - k}\, u_2 \tag{2.7-5}$$

This analysis employs a representative k equal to 0.32, based on the work of Rohsenow and supported by the work of Drew.

A six-step iterative solution for each integration cell is required. Starting at the top of the CMT, the cell exit temperature, T_{fout}, is solved using the bisection method and the mass and energy balances. Given an initial value for T_{fout}, the exit enthalpy is determined directly via the mass and energy balances as shown below:

The boundary conditions are T_w and q_2'' defined per Section 2.6, as well as, T_{fin} and W_{in} defined by adjacent integration cell. Also:

$$T_{fin} = T_w \text{ when } W_{in} = 0$$

Given an initial value of T_{fout}, and assuming linearity, then:

$$T_f = \frac{T_{fin} + T_{fout}}{2} \tag{2.7-6}$$

The condensation is calculated as:

$$u_2 = \frac{q_2''}{T_f - T_w} \tag{2.7-7}$$

$$u_1 = \frac{k}{1 - k} u_2 \tag{2.7-8}$$

$$q_1'' = u_1 (T_g - T_f) \tag{2.7-1}$$

from p. 2-50

$$W_c = q_1'' \frac{A_s}{h_g - h_f} \tag{2.7-9}$$

Applying the mass balance gives:

$$W_{out} = W_{in} + W_c \tag{2.7-10}$$

Applying the energy balance:

$$h^*_{out} = \frac{W_{in}\, h_{in} + W_c\, h_g - q''_2\, A_s}{W_{out}} \qquad (2.7\text{-}11)$$

Test is performed for convergence as:

$$B = h_{out} - h^*_{out} \qquad (2.7\text{-}12)$$

The bisection method[10] solves for the zero of B.

To ensure reasonableness and convergence, the following are also imposed:

$$T_g \geq T_f \geq T_w$$

$$T_{fout} \geq \text{lesser of } T_w \text{ and } 40$$

$$W_{out} \geq 0$$

The bisection method was selected because it reliably generates converged solutions for large ΔTs. Calculational problems can occur when wall ΔTs or steam-to-wall ΔTs are small. These problems occur only near the end of tests when wall heat flux is markedly reduced due to the very small ΔTs.

Two approaches are used when ΔTs are small and the bisection method fails to produce converged solutions: film temperatures may be set to the equilibrium value, or a simplified condensation equation may be used:

- Film temperatures are set to equilibrium values when the small ΔTs are consistent with the limited heat flux and the iterative method is nonconvergent.

- A simplified condensation equation is used when the small ΔTs are inconsistent with the limited heat flux or are inconsistent with the assumption that steam is condensing. The simplified equation is:

$$h_{out} = h_f = h_{in}$$

which results in:

$$W_c = \frac{q_2'' \; A_s}{h_g - h_{in}} \qquad (2.7\text{-}13)$$

As discussed in Section 2.6, local heat flux at the analysis elevations is calculated only when the ΔTs are consistent with the heat flux and the heat flux is sufficiently large to produce reliable results.

The method described, based on laminar flow, is applied in all cases, including rare cases in which the film Reynolds number indicates that flow would be turbulent. If it is turbulent, then the energy-effective film temperature would be closer to the steam temperature than this method implies, and thus, the calculated condensate flow would be slightly low compared to a calculation assuming turbulence.

Representative condensation rates for 100- and 300-series tests are shown in Figures 2.7-2 and 2.7-3. The steam-region wall surface area and steam-region heat transfer rate are also shown.

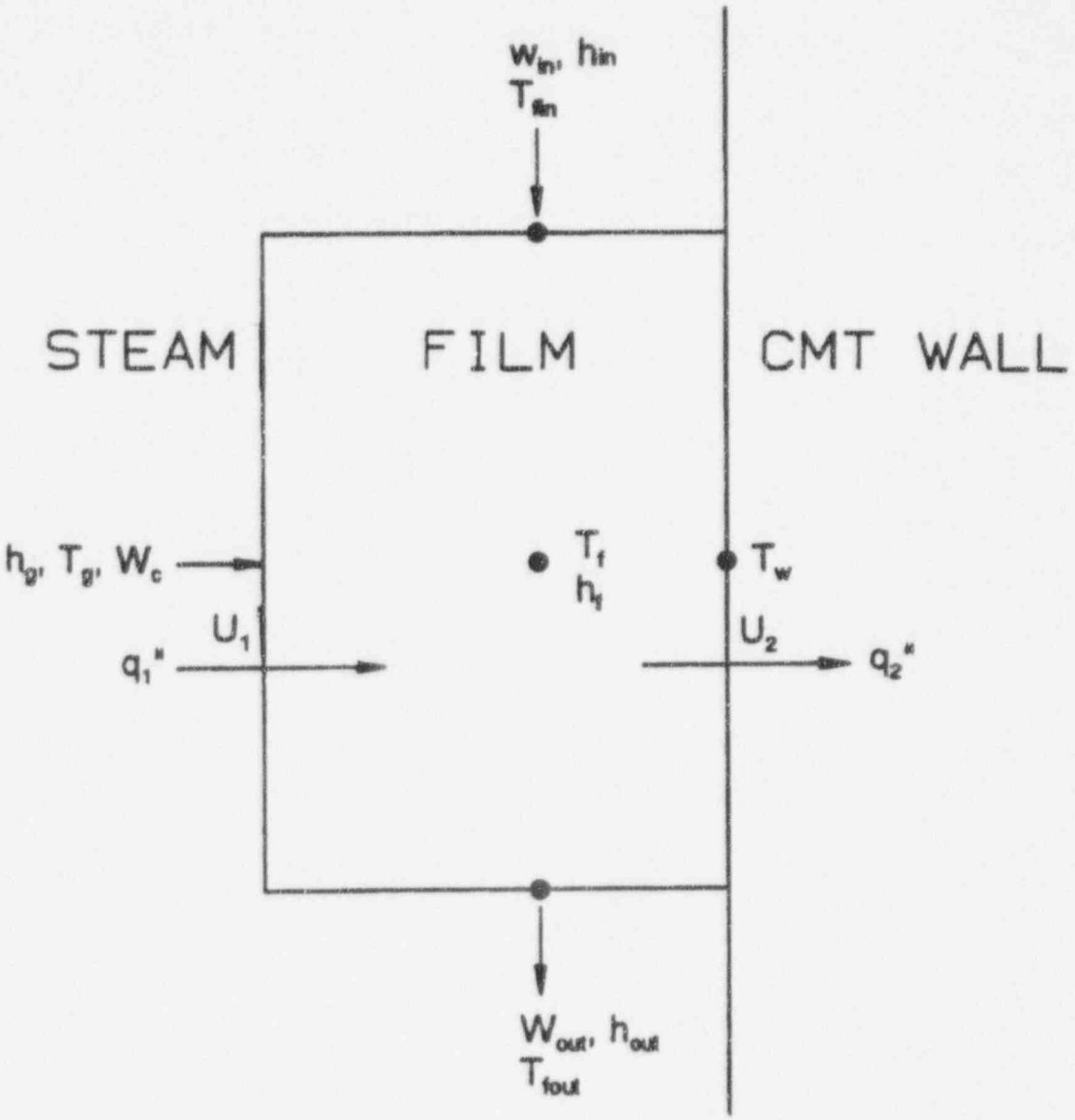

Figure 2.7-1 Wall Condensation Model - Control Volume for an Integration Cell

Figures 2.7-2 and 2.7-3 are not included in the non-proprietary version of this document.

2.8 CMT Interface Modeling

The CMT steam-to-liquid interface modeling considers two effects: draining of wall condensation into the interface, and steam condensation on the interface. Section 2.6 provides the wall condensation methodology, while this section provides three methods for determining interfacial condensation: steam mass balance, liquid mass balance, and liquid energy balance.

The term definitions are:

M_{cond_t} = integrated total condensation at time t
$M_{v\text{-}in_t}$ = integrated steam inlet flow at time t
M_{v_t} = vapor mass in CMT at time t
M_{ℓ_t} = liquid mass in CMT at time t
W_c^t = total wall condensation rate
J = conversion factors
h_g = steam enthalpy
t_c = start of test

2.8.1 Interfacial Condensation Based on Steam Mass Balance

Interfacial condensation based on a steam mass balance is calculated as the difference between total condensation and wall condensation.

Total condensation is determined by a steam-side mass balance. The total condensation at time t is defined by:

total condensation = steam flow into CMT - change of steam mass

$$M_{cond_t} = M_{v\text{-}in_t} - \left[M_{v_t} - M_{v_{t_0}}\right] \qquad (2.8\text{-}1)$$

The wall condensation at time t, $M_{wall\ cond_t}$, is defined in Section 2.6.

Interfacial condensation at time t is then defined by:

interfacial condensation = total condensation - wall condensation

$$M_{int\ cond_t} = M_{cond_t} - M_{wall\ cond_t} \qquad (2.8\text{-}2)$$

2.8.2 Interfacial Condensation Based on Liquid Mass Balance

Interfacial condensation based on a liquid mass balance is calculated as the difference between total condensation and wall condensation.

Total condensation is determined by liquid-side mass balance. The total condensation at time t is defined by:

total condensation = drain flow from CMT + change in liquid mass

$$M_{cond_t} = M_{\ell\text{-}out_t} + \left[M_{\ell_t} - M_{\ell_{t_o}}\right] \tag{2.8-3}$$

The wall condensation at time t, $M_{wall\ cond_t}$, is defined in Section 2.6.

Interfacial condensation at time t is then defined by:

interfacial condensation = total condensation - wall condensation

$$M_{int\ cond_t} = M_{cond_t} - M_{wall\ cond_t} \tag{2.8-4}$$

2.8.3 Interfacial Condensation Based on Liquid Energy Balance

Condensation based on the liquid energy balance considers the liquid internal energy, drain flow energy, total wall heat transfer, and work at the interface. The control volume for the liquid energy balance is shown in Figure 2.8-1.

Condensation based on liquid energy balance is defined by:

Total condensation rate = W_{cond} = (rate of change of liquid internal energy + rate of drain flow * enthalpy + total wall heat transfer above and below water level + pressure * rate of change of liquid volume / J) h_g

The total condensation at time t is defined by:

$$M_{cond_t} = \int_{t_o}^{t} W_{cond}\ dt \tag{2.8-5}$$

The wall condensation at time t, $M_{wall\ cond_t}$, is defined in Section 2.6.

Interfacial condensation is the difference between total condensation and wall condensation. Interfacial condensation at time t is defined by:

interfacial condensation = total condensation - wall condensation

$$M_{\text{int cond}_t} = M_{\text{cond}_t} - M_{\text{wall cond}_t} \quad (2.8\text{-}6)$$

2.8.4 Comparison of Condensation Models

The three methods for calculating interfacial condensation rely on the ability to determine either water level or liquid internal energy. Thus, the effectiveness of this approach will differ for 100- and 300-series tests due to the water level.

Since the objective of the 100-series tests is to investigate wall condensation heat transfer, the tests start with a nearly empty CMT and the condensate is drained out of the tank. As shown in Section 2.4, the level generally rises only slightly and can be accurately determined for a small time period. This severely restricts the ability to determine interfacial condensation. Since only limited instrumentation is provided at the bottom of the CMT, the ability to calculate condensation based on liquid energy balance will be most severely impacted. Liquid-energy-based condensation was therefore not investigated for 100-series tests.

Figure 2.8-2 compares the interfacial condensation based on steam mass balance to steam flow and wall condensation for a 100-series test. As shown in the figure, interface condensation is substantially smaller than both steam flow and wall condensation. Thus, the calculational uncertainty in interface condensation would be expected to be large. The water level is also shown in Figure 2.8-2. Since the total condensation calculation depends on water level, the time period when interfacial condensation can be accurately determined is also limited.

The 300-series tests start with an essentially full CMT. As shown in Section 2.4, the level generally falls at a nearly constant rate after an initial condensation period. After this initial condensation period, level and liquid energy can be reliably determined. Thus, calculation of condensation and the comparison of the three methods are far more meaningful for the 300- than the 100-series tests.

Figure 2.8-3 compares the interfacial condensation based on steam mass balance to steam flow and wall condensation for a 300-series test. Initially, interfacial condensation dominates wall condensation since the CMT is nearly full. (The level instrumentation does not provide the ability to determine if the CMT is completely filled. Thus, some wall condensation could be calculated in a full CMT.) At the end of the test, interfacial condensation is substantially smaller than both steam flow and wall condensation. Thus, the calculational uncertainty in interfacial condensation would be expected to range from small at the start of the test to large at the end of the test, since it is determined by a different method.

Interfacial condensation for a 300-series test based on the three methods is shown in Figure 2.8-4. As shown in the figure, the three methods are relatively consistent.

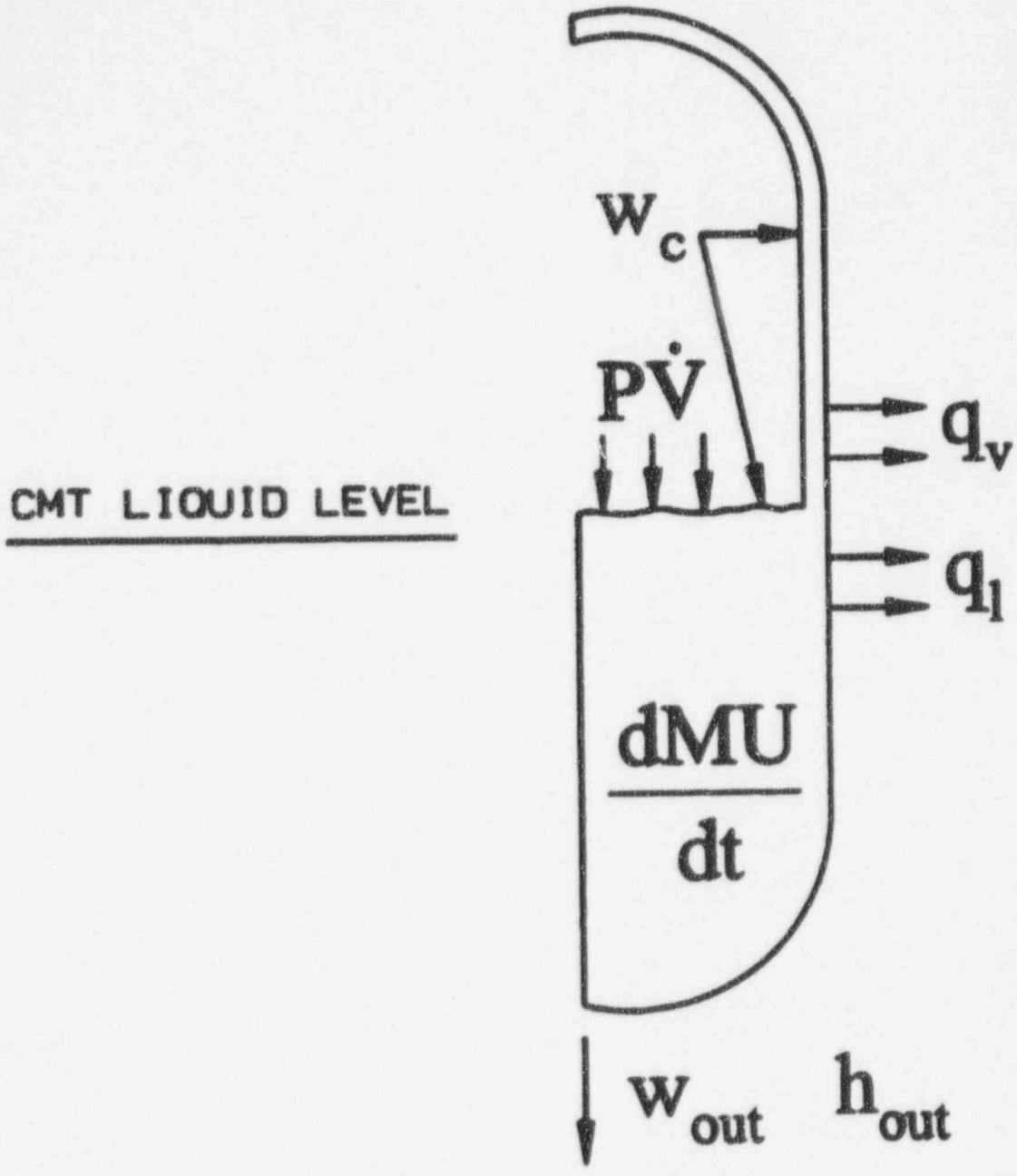

Figure 2.8-1 Liquid Energy Balance Control Volume

Figures 2.8-2 through 2.8-4 are not included in the non-proprietary version of this document.

2.9 Assessment of CMT Recirculation Tests

In the recirculation mode of operation, there is volume replacement of the cold borated CMT water with hot water that flows up the cold leg balance line to the top of the CMT. The CMT remains full during this time period. This process continues until the CMT is fully heated and the natural circulation driving head for flow decreases to zero.

The ability of the CMT test facility to model the recirculation performance of the plant CMT is examined. The recirculation phase of the series 500 tests is analyzed using a model that accounts for the thermal driving head due to the density difference in the cold CMT and the hot steam/water reservoir (S/WR), and the non-recoverable pressure losses around the circular path. This model was developed as part of the scaling assessment for the CMT test.[2] For this model, both top-down and bottom-up scaling analyses were performed to assess the capability of the test CMT to provide the key thermal-hydraulic data for the recirculation period. The governing equations for the recirculation model are presented in the following sections.

2.9.1 CMT Recirculation Behavior—Simplified Prediction Model

A simplified model of the CMT test facility was developed to study natural circulation flow. Figure 2.9-1 shows a sketch of the CMT test relative to the AP600 plant. Note that the actual pipe routing is not fully represented in this sketch.

The assumptions used in this analysis are:

- Single-phase recirculation
- One-dimensional flow
- Linear interpolation of the density gradient in the CMT
- Linear interpolation of the density gradient in the CMT test reservoir
- Essentially zero velocity in the reactor vessel downcomer annulus
- Loss coefficients are independent of Reynolds number
- Quasi-steady state conditions

The generalized mechanical energy balance equation (see Bennett and Meyers)[11] for the generated system is given as:

$$\frac{\Delta P}{\rho} + \frac{\Delta U^2}{2g_c} + \left(\frac{fL_f}{D_h} + K\right)\frac{U^2}{2g_c} + \frac{g}{g_c}\Delta L + W_s = 0 \qquad (2.9\text{-}1)$$

where:

- P = fluid pressure
- ρ = fluid density
- U = fluid velocity
- f = Darcy friction factor
- L_f = hydraulic diameter
- D_h = hydraulic diameter
- K = form loss coefficient
- g = acceleration due to gravity
- g_c = Newton's law conversion factor
- ΔL = height of the driving head for CMT flow
- W_s = shaft work, which is zero

Since the starting point and end point of the calculations are the same, then:

$$\frac{\Delta P}{\rho} = 0 \tag{2.9-2}$$

Expanding Equation 2.9-2 around the piping network using the component density gives:

$$\frac{\rho_2 U_{DVI}^2}{2g_c} - \frac{\rho_1 U_{CL}^2}{2g_c} + \left(K_{CL_N} + \frac{fL_f}{D_h}\right)_{CL} \rho_1 \frac{U_{CL}^2}{2g_c} + \left(K_T + K_{CMT_N} + \frac{fL_f}{D_h}\right)_{BL} \rho_1 \frac{U_{BL}^2}{2g_c} + \tag{2.9-3}$$

$$\left(K_{CMT_{EX}} + K_{CKV} + K_{DVI_N} + \frac{fL_f}{D_h}\right)_{DVI} \rho_2 \frac{U_{DVI}^2}{2g_c} + \frac{g}{g_c}\rho_1 L - \frac{g}{g_c}\rho_2 L = 0$$

where:

- DVI = direct vessel injection line
- CL = cold leg
- CMT = core makeup tank
- BL = balance line
- CL_N = cold leg nozzle
- DVI_N = DVI nozzle
- T = cold leg balance line tee
- CKV = CMT discharge line check valve

CMT_{EX} = CMT discharge line nozzle
ρ_1 = hot RCS fluid density
ρ_2 = cold CMT fluid density

Equation 2.9-3 can be further simplified noting that the volume flow is preserved, that is:

$$U_{CL}A_{CL} = U_{BL}A_{BL} = U_{DVI}A_{DVI} = Q_\ell \tag{2.9-4}$$

where:

A = cross-sectional flow area
Q_ℓ = volumetric flow rate

Transposing the gravity head term to the left side of the equation and using Equation 2.9-4; the system Equation 2.9-3 becomes:

$$\frac{g}{g_c}L(\rho_2 - \rho_1) = \frac{Q_\ell^2}{2g_c}\left\{\left[\left[K_{CLN} + \frac{fL_f}{D_h}\right)_{CL} - 1\right]\frac{\rho_1}{A_{CL}^2} + \right.$$

$$\left[K_T + K_{CMT_N} + \frac{fL_f}{D_h}\right)_{BL}\Bigg]\frac{\rho_1}{A_{BL}^2} + \tag{2.9-5}$$

$$\left.\left[K_{CMT_{EX}} + K_{CKV} + 1\ K_{DVI_N} + \frac{fL_f}{D_h}\right)_{DVI}\Bigg]\frac{\rho_2}{A_{DVI}^2}\right\}$$

As the CMT recirculates, the top of the CMT will fill with the less dense, hot fluid from the cold leg at density ρ_1. Recirculation will end when all of the denser liquid, ρ_2, has been replaced with the less dense ρ_1 fluid. To represent the decrease in the driving head, the buoyant term becomes:

$$\frac{g}{g_c}\left[\left\{(L - L_1)\rho_2 + L_1\rho_1\right\} - \rho_1 L\right] \qquad (2.9\text{-}6)$$

which simplifies to:

$$\frac{g}{g_c}\left[(L - L_1)(\rho_2 - \rho_1)\right] \qquad (2.9\text{-}7)$$

where L_1 is the height of less dense liquid ρ_1 in the CMT, and L is the overall height. This expression has the correct limits since at the beginning of recirculation, L_1=0, and the full driving head is available; while when L_1=L, there is no driving head and recirculation ends.

The value of L_1 can be calculated as:

$$L_1 = \int_0^t \frac{\dot{m}(t)\,dt}{\rho_1 A_{CMT}} \qquad (2.9\text{-}8)$$

where A_{CMT} is a function of L_1 for the CMT heads and $\dot{m}(t)$ is the mass flow into the CMT. Equation 2.9-8 must be solved in an iterative fashion for the CMT head volume, but can be directly solved for the cylindrical portion.

A similar calculation is used for the S/WR in the CMT test since the volume is much smaller than the volume of the reactor system. In this case, the driving head will also decrease as the reservoir fills with the denser ρ_2 fluid.

The hydraulic resistances for the experiment were measured in the pre-operational tests and were found to be very close to standard textbook values. Equations 2.9-5, 2.9-7, and 2.9-8 were programmed for the CMT test facility.

Figure 2.9-2 shows the mean flow rate as a function of time for the CMT test facility. Figure 2.9-3 shows the development of the hotter, less dense fluid level in the CMT as it drains. The dominant terms in the CMT test are the line frictional losses since there are many more length-to-diameter ratios in the test facility compared to the plant.

The dimensionless ratio of interest in the recirculation phase is the mass flux ratio (ρv) in the cold leg balance line. Since full height and full pressure simulation is preserved, this ratio should be close to unity if the resistances were maintained between the test and the plant.

A comparison of the natural circulation predictions and the actual recirculation test results is presented in Section 4.5.

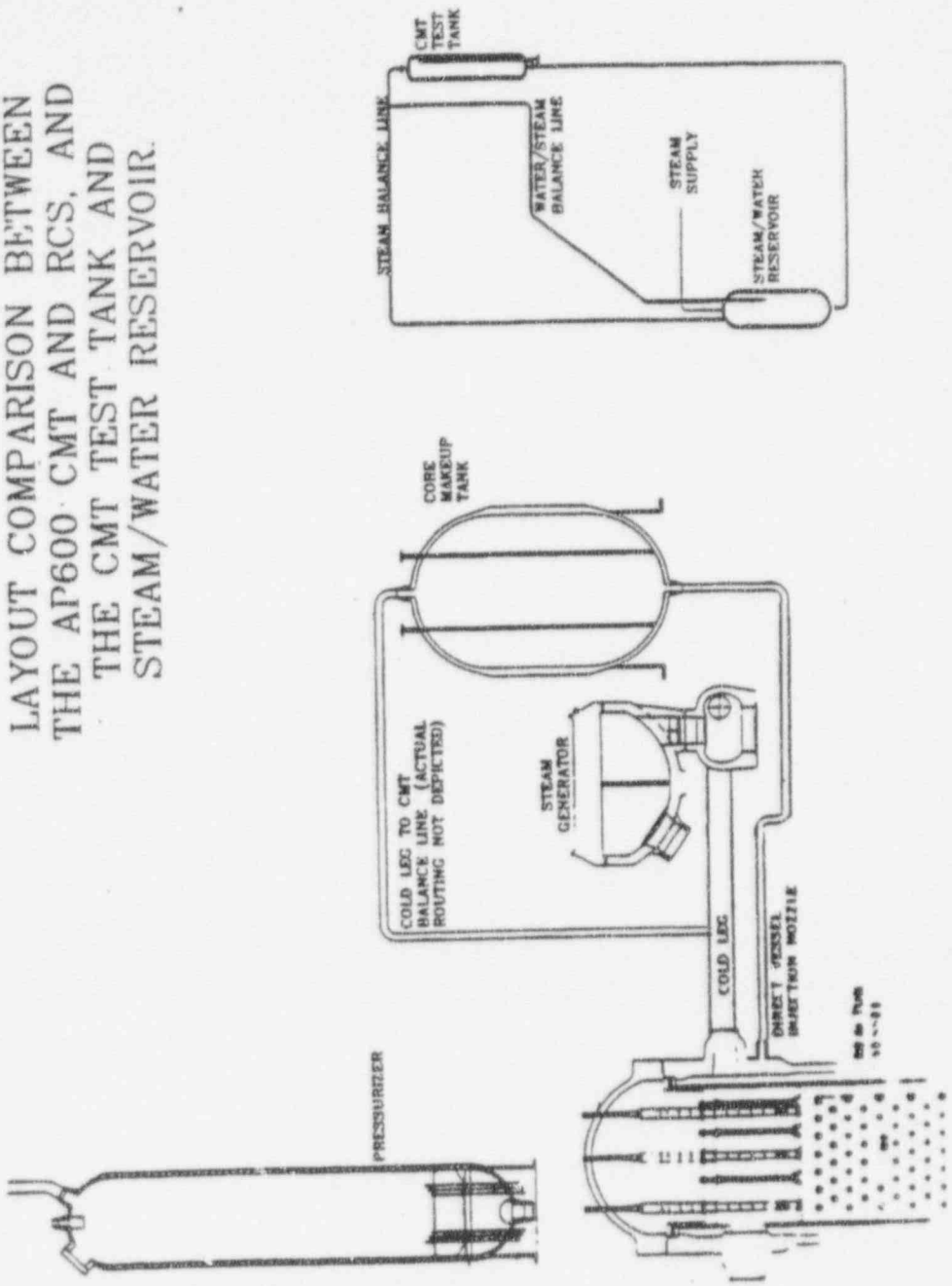

Figure 2.9-1 CMT Test Facility and AP600 Plant

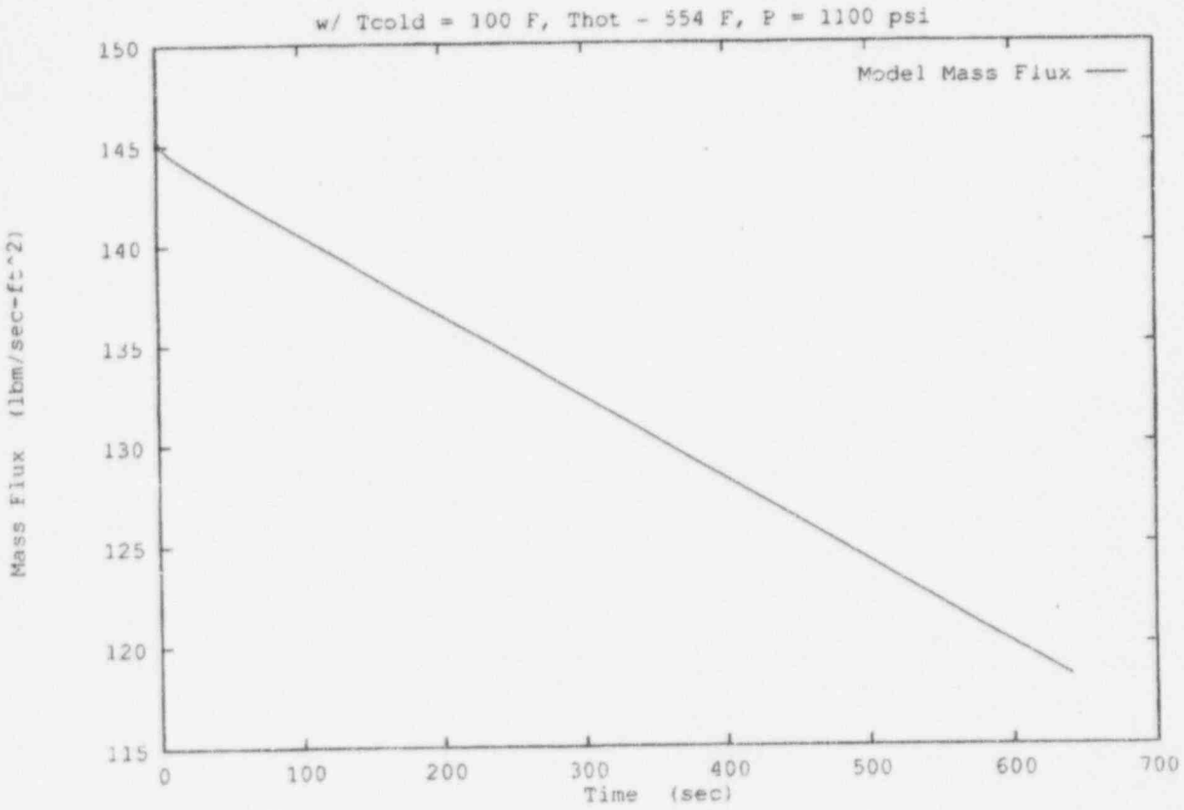

Figure 2.9-2 Calculation of the Recirculation Flow for the CMT Test Facility at 1100 psia

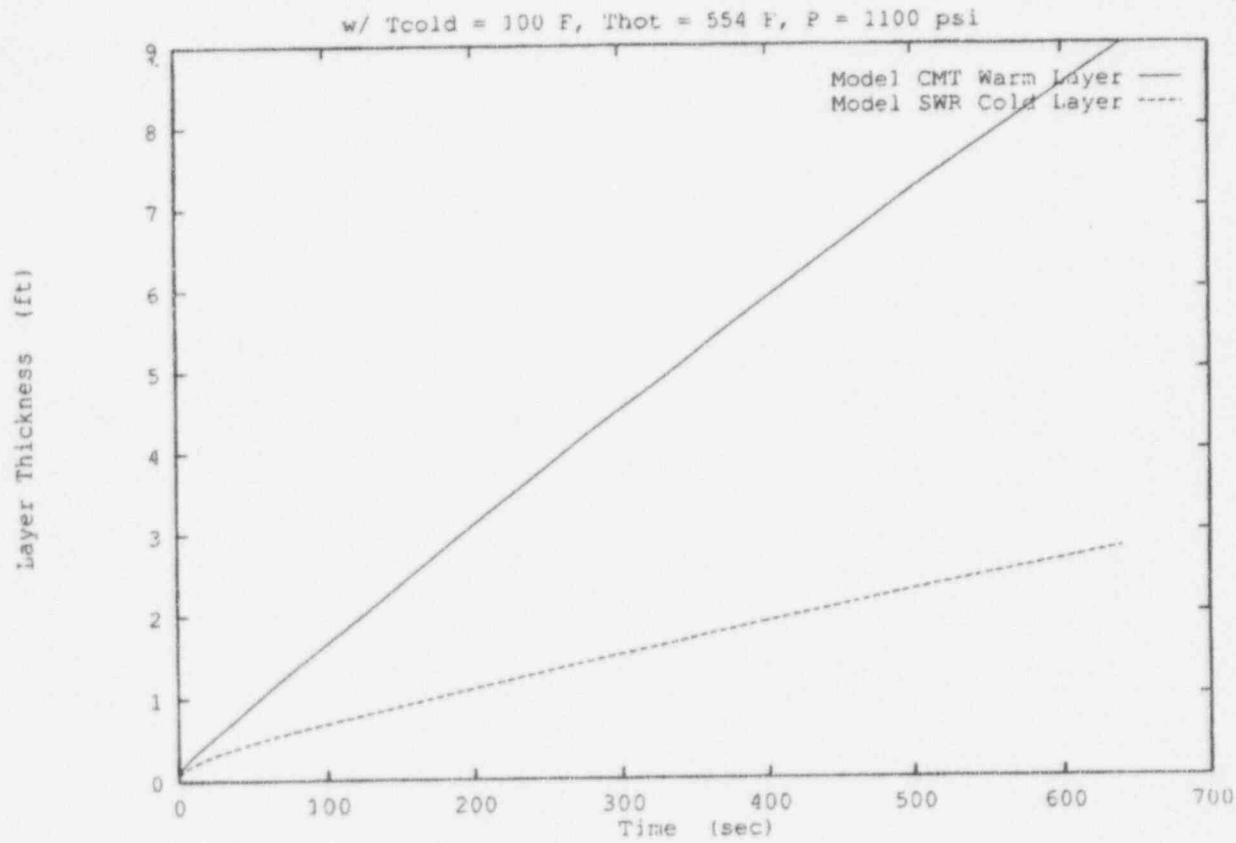

Figure 2.9-3 **Calculation of the Hot Liquid Layer Thickness for the CMT Test Facility and Cold Liquid Layer Thickness in the Reservoir at 1100 psia**

3.0 ANALYSIS OF CORE MAKEUP TANK TEST DATA

3.1 Introduction

The instrumentation used on the CMT tests was designed to provide thermal-hydraulic data that could be used to develop and verify safety analysis computer codes for the AP600. The methods of data reduction and analysis are described in Section 2.0, whereas the results of applying these analysis methods to the data are described in this section, and the application of the data to thermal-hydraulic models and modeling is described in Section 4.0.

3.2 Analysis of the 100-Series Tests

The objectives of the 100-series CMT tests were to:

- Observe and record the pressurization rate and heat up of the CMT walls at each of the specified test steam pressures and corresponding temperatures with the CMT initially empty and evacuated of all air and noncondensible gases

- Observe and record the amount of steam condensed on the CMT walls and collected in the steam/water reservoir (S/WR), using CMT discharge line flowmeters and level measurement in the S/WR

- Observe and record heating of the CMT walls at the specified test steam pressure with the CMT initially filled with a predetermined quantity of noncondensible gas, established by pressurizing the evacuated CMT with air to the specified internal pressure

The tests that were analyzed are given in Table 3.2-1 and cover a range of system pressures and amounts of noncondensible gases. Note that test C002105, a 2235-psig test, was not analyzed because of the design change that eliminated the pressurizer balance line.

3.2.1 Analysis Results for Test C047101, 10 psig (25 psia)

The system pressure, drain flow, and inlet steam flow for this test are shown in Figure 3.2-1. Since the CMT was initially evacuated, the tank pressure was nearly zero. Once the steam flow began, the pressure recovered to the preset system pressure and was relatively constant. As the plot of steam flow indicates, the steam flow was initially very high as the steam flowed into the initially evacuated CMT. The steam flow may have been initially choked until the CMT pressurized. Once the tank is pressurized and the condensation heat transfer is established, the steam flow then began to slowly decrease as the CMT walls heated up. The plot of drain flow in Figure 3.2-1 indicates a time delay, relative to the steam flow until the CMT pressure was close enough to the S/WR pressure to allow gravity drain. After the steam flow was established and as the condensation occurred, the drain flow was nearly a constant flow and then slowly decreased, similar to the steam flow.

The mass balance for this test is shown in Figure 3.2-2. The curves in Figure 3.2-2 include: the integrated steam flow into the tank, the integrated outlet drain flow, the change in measured liquid mass in the tank as the tank drains, the change in steam mass in the tank as it drains, and the mass imbalance that is the excess in measured mass in the tank compared to the difference between calculated inflow and outflow. The majority of the imbalance was caused by the rapid variation in the steam flow that occurred during the initial period of the test. The steam flow was measured using the vortex meter in the simulated cold leg balance line. If the vortex meter was out of range, the calibrated pressure drop measurements in the cold leg balance line were used to calculate the steam flow. The level in the CMT was also used in the initial period to calculate the mass accumulation in the tank before the condensate drained out of the tank. The liquid drain flow was measured using a turbine meter at the low point of the tank discharge line. The mass imbalance was about 12 percent of the total measured drain flow at 500 seconds, which was the last time that the local heat transfer coefficients were calculated from the data.

The analysis methods described in Section 2.0 were applied to the wall thermocouple measurements to determine the calculated wall heat flux values. Figure 3.2-3 shows the measured wall temperatures at each measuring location along the CMT. The first location is in the dome region of the CMT, while the remaining four locations are in the cylindrical portion of the CMT. The exact location of the thermocouples is given in the CMT Test Data Report,[3] and the elevations relative to the inside bottom of the CMT are indicated on the figure. As the figures indicate, as the steam entered the CMT, the wall temperature began to rise as the steam was condensed. The wall temperature eventually approached the saturation temperature. The inside surface temperature was calculated from the data using the CONTRA program, described in Section 2.0. The saturation temperature is also plotted on the figures to indicate that the inside wall quickly heated up toward the saturation temperature, while the bulk of the metal lagged due to its thermal inertia. (Note that a minimum was set on the calculated absolute pressure to avoid problems in calculating fluid properties. Thus, there was an artificial minimum saturation temperature.)

The calculated wall heat flux at each of the analysis elevations is shown in Figure 3.2-4. The heat flux had its highest value when the steam initially entered the tank and condensed on the cold walls. As the temperature gradient became established in the thick CMT walls, the heat flux slowly decreased and approached zero as the walls heated up due to the condensation. Examining the heat flux profile at a given time along the tank wall indicates that the lower elevations on the CMT had a somewhat lower value of the heat flux, most likely due to the thicker condensate layer at the lower elevations of the CMT.

The heat transfer coefficient is calculated at each analysis elevation using the CONTRA calculated heat flux and the difference between the extrapolated inside wall temperature and the bulk fluid, which was the saturation temperature for these tests. The resulting calculated heat transfer coefficient is shown in Figure 3.2-5 for this test. The calculated condensation heat transfer coefficient tends to be fairly constant, whereas the heat flux slowly decreased as the thermal front penetrated into the thick CMT walls. The condensation heat transfer coefficient was larger on the dome region of the CMT because the steam was jetting out of the diffuser holes, parallel to the top of the dome surface. It is postulated

that this created a thinner condensate film and hence higher heat transfer at the dome. The coefficient in the dome decreased as the steam flow decreased. The heat transfer to the CMT wall quickly became limited by the conduction heat transfer in the CMT metal. The heat transfer coefficient calculation was terminated when the wall temperature approached the saturation temperature.

Figure 3.2-6 shows the axial distribution of the fluid temperatures within the CMT. As time progressed, the axial fluid temperatures rose nearly uniformly within the tank. Since this test was performed at a constant pressure without noncondensible gases present, the axial temperature gradient of the fluid temperature was nearly uniform.

3.2.2 Analysis of Test C078102, 135 psig (150 psia)

The same overall trends were observed in this test at 150 psia as compared to the previous test, C047101. Figure 3.2-7 shows the CMT system pressure and indicates that while the tank was initially evacuated, the higher pressure rapidly filled the tank with steam and brought it to the preset operating pressure for the test. Figure 3.2-7 also shows the steam flow for this test and indicates the initial steam flow spike at the beginning of the test as the steam flowed into the evacuated tank. As the tank pressurized, the steam flow began to decrease with time as the wall temperature gradients were established. The drain flow is also shown in Figure 3.2-7 and indicates the same behavior as the previous test. The magnitude of the drain flow was larger than test C047101 since the mass of steam condensed was larger because of the higher pressure.

The mass balance for this experiment is shown in Figure 3.2-8 and indicates that the overall mass balance had a larger uncertainty than the 10-psig test, approximately 23 percent of the integrated drain flow at 500 seconds when the calculation of the heat transfer coefficient ended.

The wall temperatures are shown in Figure 3.2-9, and the resulting calculated heat flux is given in Figure 3.2-10. The heat flux values increased as the test pressure increased since temperature differences were larger, which resulted in more energy being transferred to the wall. The resulting condensation heat transfer coefficients are shown in Figure 3.2-11 and indicate that as the system pressure increased, the condensation heat transfer coefficients were similar to the previous test. As the temperature distribution became established in the CMT wall, the heat transfer to the wall was conduction-limited, and the heat flux decreased and heat transfer coefficients became nearly constant. Again, the calculation of the heat transfer coefficient was terminated when the calculated wall temperature approached the saturation temperature. The CMT axial fluid temperature plot is shown in Figure 3.2-12 and indicates that the axial temperature distribution became uniform.

3.2.3 Analysis of Test C079103, 685 psig (700 psia)

The data for this test were reduced and analyzed in the same fashion as the previous tests. The results are shown in Figures 3.2-13 to 3.2-18. As these figures indicate, the behavior was the same as the previous tests with the exception that the heat flux values again were larger as the pressure increased. The mass imbalance for this test was approximately 13 percent of drain mass at 500 seconds when the

heat transfer coefficient calculation ended. The calculated condensation heat transfer coefficients were also similar to the previous tests at this higher pressure. The axial distribution of the fluid temperatures in the CMT was also uniform.

3.2.4 Analysis of Test C042104, 1085 psig (1100 psia)

The data for this experiment were reduced and analyzed in the same fashion as the previous tests. The results are shown in Figures 3.2-19 to 3.2-24. The mass imbalance for this test was approximately 6 percent of drain mass at 600 seconds when the calculation of the heat transfer coefficient ended. The mass imbalance improved as the system pressure increased since the mass flow of the steam into the CMT and the drain flow out of the tank were larger, so measurement errors were a smaller fraction of the total. As these figures indicate, the behavior was the same as the previous tests, including the trend that the condensation heat flux was higher at the higher pressure. The calculated condensation heat transfer coefficients were about the same as the previous low pressure tests toward the end of the heat transfer calculation. The calculated heat transfer coefficients were larger early in the test compared to the previous tests.

3.2.5 Analysis of the Effects of the Initial Noncondensible Gas on the CMT Wall Heat Transfer

When the primary system depressurizes due to the activation of the ADS system or the break, a potential exists for some of the nitrogen gas from the accumulators to flow into the CMTs from the cold leg balance line. Data from the literature indicate that even small amounts of noncondensible gases can have a significant effect on the condensation coefficients. It is postulated that the noncondensible gas will form a layer on the wall, through which the steam vapor must diffuse to be condensed. The added resistance from the noncondensible layer reduces the effective condensation heat transfer coefficient.

Three separate tests were performed to analyze the effects of the addition of noncondensible gases on the wall condensation heat transfer. The tests were performed at 10 psig (25 psia), since this is the most likely pressure at which the noncondensible gases would be present in the CMT at the end of accumulator injection.

The results of the data reduction and analysis for the three tests with noncondensible gases, tests C044106, C045107, and C046108, are shown in Figures 3.2-25 to 3.2-42. The same figures are presented for these tests as were presented for the reference test with no initial air, test C047101. The mass balances for all three noncondensible injection tests were within 10 percent. The inlet steam flow and drain flow behavior was very similar to test C047101, such that almost no effect of the noncondensible gases could be observed. The calculated heat fluxes for the tests with the noncondensible gas were almost the same as the reference test. The difference that can be observed in the test data is the axial fluid temperature distribution in the CMT. If the axial fluid temperature distribution for the reference test is compared to the tests with the initial noncondensible gases (compare Figure 3.2-6 to Figures 3.2-30, 3.2-36, and 3.2-42), it is apparent that the initial noncondensible gas was pushed to the bottom of the CMT. The figures indicate that as the steam

entered and pressurized the tank, the noncondensibles were displaced to the bottom of the tank. The figures show that after approximately 200 seconds, the majority of the noncondensibles were in the bottom 40 in. of the tank. After 1000 seconds, the noncondensibles were concentrated in the bottom 20 in. of the tank.

The calculated heat transfer coefficients at the top of the tank were nearly the same as the reference test with no initial air in the tank. For test C046108, a difference in the heat transfer coefficients can be observed early in time for the first 200 seconds. The heat transfer at the dome location also shows an effect of the noncondensibles, as seen in Figures 3.2-35 and 3.2-41 as compared to Figure 3.2-5. The heat transfer coefficients at the other elevations show an initially lower value for the first 200 seconds, as seen in comparing Figures 3.2-35 and 3.2-41 versus 3.2-5. If the axial plots of the fluid temperature are examined in Figures 3.2-36 and 3.2-6, it can be seen that the fluid temperature distribution was being established during the first 200 seconds as the pressure rose. The noncondensible gases were present at all elevations in the CMT but tended to be at a higher concentration at lower elevations. Therefore, there is an effect of the noncondensible gases on the local heat transfer coefficient, as seen in Figures 3.2-35 and 3.2-5. However, as time progressed, the noncondensible gases were pushed to the bottom of the CMT, and the wall heat transfer at the upper elevations became the same as the test without the noncondensibles.

TABLE 3.2-1 100-SERIES TESTS MATRIX				
Nominal Pressure psig--->	**10**	**135**	**685**	**1085**
Nominal Air (psi)				
0	C047101	C078102	C079103	C042104
0.2	C044106			
1.0	C045107			
2.0	C046108			

Figures 3.2-1 through 3.2-42 are not included in the non-proprietary version of this document.

3.3 Analysis of the 300-Series Tests

3.3.1 Introduction

The 300-series tests examined the draining behavior of the CMT when steam was allowed to flow into the liquid-filled tank as it drained. A similar situation would exist in a postulated large small-break accident or in a large-break LOCA where the CMT has very little time to recirculate before steam is admitted, such that the CMT liquid is subcooled. The line from the steam/water reservoir (S/WR), which simulated the cold leg balance line, was filled with steam and the test was initiated by opening the drain valve on the discharge line of the CMT. As the CMT drained, steam flowed to the top of the tank and was rapidly condensed by the cold water, decreasing the pressure at the top of the tank, thereby reducing the tank drain flow rate. As the water layer at the top of the CMT heated up to near the saturation temperature, the rapid condensation ceased, and the tank drained normally. As the tank drained, the hot liquid layer on the top of the CMT transferred heat to the initially cold CMT walls by convection. The liquid level in the tank decreased as the tank drained and there was steam condensation on the tank walls and condensate collected in the tank.

The test matrix for the 300-series tests that were analyzed is shown in Table 3.3-1. The 300-series tests were conducted over a full-pressure range, characterizing the CMT draining behavior for the small-break and large-break LOCA performance of the CMT. Several different preset drain line flow resistances characterized by their nominal free-flow drain rates were investigated to observe the effects on the steam/water condensation as well as the wall condensation. The test results were grouped by pressure and discussed. The drain flow effects were secondary as compared to the pressure effects.

3.3.2 Analysis of 10-psig (25-psia) 300-Series Tests

There were four 300-series tests performed at 10 psig (25 psia), as shown in Table 3.3-1. The parameter that was varied for these tests was the nominal CMT drain rate, which varied from 6 to 17 gpm. Test C027304, the 11-gpm test, will be discussed in detail since the other 10-psig tests behave similarly. Figure 3.3-1 shows the measured inlet steam flowrate, the drain rate, and the pressure in the CMT and in the S/WR. When the drain valve on the CMT discharge line was opened, starting at time zero, the CMT started to drain by gravity into the S/WR. As the tank began to drain, steam flowed from the top of the S/WR to the CMT where it was rapidly condensed by the cold water at the top of the tank. The CMT pressure decreased, as seen in Figure 3.3-1, inducing additional steam to flow into the CMT, resulting in sustained high steam flow, as also seen in Figure 3.3-1. The steam pressure in the CMT dropped to approximately 50 percent of the upstream S/WR pressure, indicating that choking occurred in the inlet to the CMT. The choking limited the amount of steam flow and hence its velocity and momentum flux into the CMT.

The rapid condensation at the top of the tank retarded the drain flow, as shown in Figure 3.3-1, to approximately 0.4 lbm/sec. The rapid condensation process continued in this test for approximately 60 seconds, at which time the liquid in a thin top layer was quickly heated to near the saturation temperature, as shown in Figure 3.3-2. This figure plots the axial distribution of fluid temperatures at

selected times during the experiment. The top-most point, shown at 120 in. for convenience, was in the inlet nozzle to the CMT. As the figure indicates, a hot liquid layer was developed at the top of the tank due to the rapid condensation process occurring there. The initial water level was filled to this elevation as indicated on the top plot in Figure 3.3-2 at zero seconds. At 60 seconds, the water at the top of the CMT heated up to near the saturation temperature from the thermocouple in the inlet nozzle down to an elevation of 109 in. This corresponds to a hot layer thickness 5 in. from the top of the CMT. This is shown in the second from the top plot in Figure 3.3-2. As the tank drained, the hot liquid layer moved down the tank, as seen in the other plots shown in Figure 3.3-2. Once the hot liquid layer was established, the CMT began to drain, as seen in the level plots shown in Figure 3.3-3 and in the drain flow plot, previously shown in Figure 3.3-1, with a drain flow of 1.4 lbm/sec, as compared to the initial drain flow of 0.4 lbm/sec.

Figure 3.3-2 also indicates that until 60 seconds there was a thicker mixing layer, extending down to the 101" elevation, or 13 in. from the top. This deeper mixing layer heated only about 50°F to 120°F, then diffused a little as it was carried down by the draining of the tank.

During the draining process, cold water drained out the bottom of the CMT, followed by a cold/hot water interface, followed by a hot water layer, followed by a hot water/steam interface. As the CMT drains and the cold water/hot water interface passes a wall thermocouple location, the hot water was detected by these thermocouples, and the walls heated up. The walls were further heated as the hot water/steam interface passed the instrumented locations. This behavior is seen in Figure 3.3-4 for the different wall instrumented locations. The top solid line curve on each of these plots was the calculated saturation temperature from the local pressure in the CMT. The local fluid temperature is also shown on these figures and indicates that the hot liquid layer was initially transferring heat to the walls. As the hot liquid layer drained past the instrumentation location and steam began to condense on the CMT walls, the wall temperatures began to heat up more rapidly.

The wall heat fluxes at the instrumented locations were calculated from the CONTRA program, as described in Section 2.0, and are shown in Figure 3.3-5 for each instrumented location. The hot liquid heat transfer to the cold CMT walls is clearly shown in the second plot in Figure 3.3-5 as the plateau in the heat flux before the sharp heat flux spike. The spike in the heat flux occurred when the hot water/steam interface passed the instrumented location. The convective heat transfer coefficients from liquid to the cold CMT walls can be calculated from the plateau value of the heat flux along with the local wall and fluid temperature values, as will be discussed in Section 4.4.

The local heat transfer coefficient was calculated from the measured heat flux and was plotted in Figure 3.3-6 for each instrumented elevation. The heat transfer calculation was not performed when the temperature difference between the inside wall and the fluid temperature was too small, such that the uncertainty in the heat transfer coefficient became unrealistically large. The heat transfer coefficients that were calculated for the steam periods were normalized, as shown in Section 3.3.1, as a function of the film Reynolds number and were found to be bounded by the Nusselt laminar film correlation.[6]

As described in Section 2.0, the mass and energy calculations performed on the CMT tests result in the calculation of the heat transfer rates to the CMT walls, from convective heat transfer below the water level, and from condensation at the water level as well as to the liquid interface. Figure 3.3-7, the top plot, shows the heat transfer rates to the CMT walls from the condensation (vapor heat transfer, the top curve in the first plot) and liquid heat transfer (the bottom curve in the same plot). As the figure indicates, the majority of the heat transfer to the CMT wall was by condensation. The second plot on Figure 3.3-7 is the condensate mass (lbm) that is calculated from the condensation heat transfer to the CMT walls and at the steam/liquid interface. The condensate mass for the steam/water interface was calculated as the closure term in the steam mass balance and was the difference between the total steam flow into the CMT and the wall condensation plus steam storage in the CMT. As Figure 3.3-7 indicates, for the first 200 seconds the majority of the heat transfer was to the steam/liquid interface by direct condensation and mixing of the incoming steam and the subcooled CMT liquid. Once the interface was heated up by the condensation and the mixing ends, there was very little additional direct interfacial heat transfer, and the majority of the heat transfer was due to wall condensation. Figure 3.3-7 was consistent with the previous figures and indicates that the initial period of the test was dominated by the direct interfacial heat transfer at the top of the tank. However, once the top liquid layer was heated to the saturation temperature, the tank drained, and the wall condensation became dominant.

Figure 3.3-8 shows the calculated transient mass balance for this test. The mass imbalance at the end of the test is approximately 10 lbm or 0.9 percent of the initial CMT mass or total outflow mass. Mass imbalance is the measured change in CMT mass storage plus mass flow out minus mass flow in. Table 3.3-2 gives the tabulated mass imbalance for all the valid 300-series CMT tests. All of the 300-series tests have mass imbalances of less then 10 percent and the majority are under 3 percent, thus, the data can be used with confidence.

The other 10-psig (25-psia) 300-series tests show the same behavior as test C027304. Tests C031307 and C032310 are the higher drain flow tests at 16 and 17 gpm, respectively. Both of these tests indicate that the rapid condensation time period is somewhat longer than test C027304, an 11-gpm drain test. The rapid condensation period lasts 70 and 75 seconds, respectively, in the faster drain tests, however, the characteristics are the same as test C027304.

3.3.3 Analysis of the 45-psig (60-psia) 300-Series Tests

There were three tests performed at 45 psig (60 psia) with different preset drain rates, as seen in Table 3.3-1. The behavior of the 45-psig tests was very similar to the 10-psig tests, except that the steam/water interaction at the top of the CMT continued for a longer time as the resulting mixing depth was larger at 45 psig. Test C049318 will be examined in detail, however, the other 45-psig tests at different drain rates behaved similarly.

The inlet steam flow, CMT drain flow, and the CMT and S/WR pressure are shown in Figure 3.3-9. As this figure indicates, the rapid condensation was prolonged for this system pressure and the CMT pressure was approximately 15 psi below the S/WR pressure. As a result, the steam flow into the

CMT was large and extended for a longer period. The flow into the CMT was not choked in this test resulting in larger steam flows into the tank. The rapid condensation, which induced the steam flow and reduced the CMT pressure, also resulted in a delay of 163 seconds before the CMT drain flow is established. It was observed that the 6-gpm drain rate test did have a shorter delay time before full drain flow was established (60 seconds) as compared to the other 45-psig tests.

The development of the hot liquid layer at the top of the CMT is seen in Figure 3.3-10 from the fluid thermocouples in the CMT, which are plotted as temperature versus elevation. As this figure indicates, at the time that the CMT began to freely drain, the hot liquid layer was approximately 20-in. thick as seen by comparing the liquid level plot in Figure 3.3-11 with the 160-second curve given in Figure 3.3-10. The increased thickness of the hot liquid layer was due to the increased steam flow into the tank at 45 psig, as compared to 10 psig. The steam flow for the 45 psig test was not choked and was twice as large as the 10-psig tests. As a result, the increased steam flow causes increased mixing of the subcooled CMT liquid, such that the mixing depth, or hot liquid layer, was larger for the 45-psig cases. The liquid level shown in Figure 3.3-11 indicates that the level is just beginning to drop as the CMT liquid temperature is reaching saturation.

The wall temperatures, calculated heat flux values, and the CMT wall heat transfer coefficients are shown in Figures 3.3-12 to 3.3-14. The behavior for this pressure was similar to the 10-psig cases, except that there was a more clearly denoted heat flux value for the convective heat transfer to the walls from the hot liquid layer at the top of the CMT. These heat flux values are the plateau values of heat flux that occur before the heat flux spike, which is due to the hot liquid layer/steam interface passing the measurement point. There was also a lower, near constant value of the heat transfer coefficient during this time period at 102 in. and below, as seen in Figure 3.3-14, which represents the convective heat transfer to the CMT walls.

In Figure 3.3-15, the top plot shows the calculated heat transfer rate from the vapor to the CMT wall as well as the liquid to the CMT wall. As this figure indicates, there was a significant heat transfer from the liquid to the wall until the CMT drained and the walls were exposed to the steam after 160 seconds. This was consistent with the delay in the draining of the CMT, which exposed the CMT walls to condensation. The calculated condensate masses for the wall condensation and the interfacial condensation are shown in the lower plot in Figure 3.3-15. Since the steam/water mixing was increased for this pressure, the amount of condensate formed at the steam/water interface in the CMT was also increased. It took until 600 seconds before the condensate from the wall condensation exceeded the interfacial condensate. As with the 10-psig tests, once the top liquid layer was at the saturation temperature, the interfacial condensation was greatly reduced.

The mass balance for this experiment is shown in Figure 3.3-16 and indicates that the mass imbalance at the end of the drain period was 14 lbm or 1.1 percent of the drain mass.

3.3.4 Analysis of the 135-psig (150-psia) 300-Series Tests

There were four 135-psig 300-series tests at different drain rates. The behavior of these tests is similar to the previous series of tests at the lower pressures. One trend that was noticed was that as the drain flow increased, the amount of mixing also increased, which resulted in longer draining delays. The figures for test C080305 will be presented and discussed.

Figure 3.3-17 shows the inlet steam flow, CMT drain flow, and the CMT and S/WR pressures. As the figure indicates, there was only a small delay in both the CMT drain flow and the steam spike into the CMT. The tank pressure was only about 10 psi below the reservoir pressure, so the steam flow into the CMT was not choked. Test C034308, with a 16-gpm preset drain rate, did show a longer delay time and a lower pressure in the CMT than test C080305 with the 11-gpm drain rate.

The axial fluid temperature distribution in the CMT is shown in Figure 3.3-18 and is similar to the other tests. Water level is shown in Figure 3.3-19. The wall temperature measurements are shown in Figure 3.3-20, and the resulting calculated heat flux values are shown in Figure 3.3-21. There was a plateau of the heat flux value before the heat flux spike, which represents the convective heat transfer to the CMT walls. The calculated heat transfer coefficient is shown in Figure 3.3-22 and is similar to the 45-psig tests.

The top plot in Figure 3.3-23 shows the calculated heat transfer from the vapor phase to the CMT walls and the liquid phase to the CMT walls. As this figure indicates, the majority of the heat transfer was from the vapor to the walls. The lower plot shows the calculated condensate from the wall condensation and from the interfacial heat transfer at the steam/water interface. The amount of mixing was not large in this test and the amount of condensate from the interfacial heat transfer was only significant early in time when the steam/water mixing occurred at the top of the CMT.

Figure 3.3-24 shows the mass balance for this test and indicates a mass imbalance of approximately 10 lbm or 0.8 percent at the end of the test.

3.3.5 Analysis of the 685 psig (700 psia) 300-Series Tests

There were four 685-psig (700-psia) tests performed with different drain rates, as indicated in Table 3.3-1. The same thermal-hydraulic behavior was observed for these tests as compared to the previous tests. For test C052321, at 11 gpm, Figures 3.3-25 to 3.3-32 show the same set of plots as previously shown for the lower pressures. As the figures show, there is a moderate delay time of 70 seconds before full CMT drain, which indicates that the steam/water mixing effects at the top of the CMT were less for this pressure. The early mixing depth was only about 5 in. The amount of interfacial heat transfer was smaller, relative to the wall heat transfer, for this pressure. The mass imbalance for this test was 8 lbm or 0.6 percent. There was not a noticeable effect of the preset CMT drain rate in this set of tests.

3.3.6 Analysis of the 1085 psig (1100 psia) 300-Series Tests

There were three 1085-psig (1100-psia) tests performed at different drain rates, as shown in Table 3.3-1. The 1085-psig tests showed the same behavior as the 685-psig tests. Figures 3.3-33 to 3.3-40 for test C029306 at 11 gpm are similar to the 685-psig test at 11 gpm (C052321). The time delay for this test was short, similar to the 685-psig test, and the steam/water mixing effects at the top of the CMT were less pronounced. There were delays in the CMT free drain due to the condensation at the top of the CMT, but the times were short, similar to the 685-psig test. The mass imbalance for this test was 11 lbm or 0.8 percent. There were no noticeable effects of the preset CMT drain rate in this set of tests.

TABLE 3.3-1
300-SERIES TESTS MATRIX

Nominal Pressure (psig) --->	**10**	**45**	**135**	**685**	**1085**
Nominal Drain Rate (gpm)					
6	C037301	C048317	C036302	C051320	C038303
11	C027304	C049318	C080305	C052321	C029306
16	C031307	C050319	C034308	C053322	C039309
17	C032310		033311		
24				C054323	

TABLE 3.3-2 CMT 300-SERIES TESTS MASS BALANCE RESULTS			
Test Run	**Mass Imbalance (lb)**	**Drain Mass (lb)**	**Imbalance Percentage of Drain Mass (%)**
C037301	-2	1209	0
C036302	21	1267	2
C038303	110	1465	8
C027304	-10	1119	-1
C080305	10	1269	1
C029306	11	1374	1
C034308	-15	1131	-1
C039309	-28	1390	-2
C032310	-17	1164	-2
C033311	2	1087	0
C048317	15	1249	1
C049318	4	1242	0
C050319	9	1220	1
C051320	27	1402	2
C052321	-8	1365	-1
C053322	-16	1378	-1
C054323	-33	1345	-3
C054323	-33	1345	-3

Note: Mass imbalance is calculated between the time the drain valve starts to open and 15 seconds before the water level reaches its minimum, i.e., the drain valve starts to close.

Figures 3.3-1 through 3.3-40 are not included in the non-proprietary version of this document.

3.4 Analysis of the 400-Series Tests

This section covers the AP600 CMT 400-series matrix tests, which addresses CMT draindown during depressurization. These tests are similar to the 300-series tests, except that once the rapid condensation period was over and the CMT was gravity-draining at a constant pressure, the tank pressure decreased at a preset rate to simulate the depressurization effects. There are four tests in the series, C055401, C056402, C057403, and C058404, covering a range of depressurization rates. The tests are run to study CMT draindown while the steam supply pressure is decreasing, similar to the expected plant depressurization with the AP600 automatic depressurization system (ADS).

A complete list of all the analyzed 400-series tests is provided in Table 3.4-1. Figure 3.4-1 shows the facility configuration for the 400- and 500-series tests.

The objectives of the 400-series tests are:

- Observe and record the rate at which water drains from the CMT during depressurization
- Characterize the CMT draindown rate as a function of steam pressure (or temperature) and depressurization rate
- Characterize the CMT wall and water heat-up during draindown while the steam supply pressure is decreased

3.4.1 Test Results for C055401

This test examined the effects of CMT draindown during depressurization. The CMT is initially full of water, and the initial pressure was 1085 psig. The system was depressurized at a rate of 1 psi/sec.

The liquid level in the CMT is shown as a function of time in Figure 3.4-2. At time zero, valve V3 was opened, and the tank drained. The tank was completely empty at 660 seconds.

The CMT pressure is shown in Figure 3.4-3. The pressure was at the target pressure of 1085 psig when valve V3 was opened. The tank was held at a constant pressure until 140 seconds at which time the depressurization begins. The depressurization rate was approximately 1 psi/sec. The final pressure was 440 psia when the CMT was empty. The steam flow into the CMT is also shown in Figure 3.4-3. After an initial flow spike, the steam flow was established at 0.38 lbm/sec 100 seconds after valve V3 was opened. The steam flow decreased as the tank drained due to the lower rate of discharge flow, reaching 0.2 lbm/sec at the end of draindown. The CMT discharge flow is also shown in Figure 3.4-3. The flow reached a maximum of 2.5 lbm/sec 50 seconds after valve V3 was opened. The flow then decreased due to the decreasing hydrostatic head, reaching 1.5 lbm/sec when the tank was empty.

The axial fluid temperature is shown in Figure 3.4-4. At time zero, the entire tank was at the initial temperature of 80°F. The temperature history at various elevations shows the progression of the liquid/steam interface and the development of a hot liquid layer. The vapor temperature, which was measured at each elevation as the interface passed, decreased from 550°F at the start of draindown to 465°F when the tank was empty. This was consistent with the reduction of the system pressure.

The passing of the liquid/steam interface is also shown in Figures 3.4-5 and 3.4-6, which show the wall heat transfer coefficient and heat flux, respectively, as a function of elevation in the CMT vessel. Condensation of the hot steam on the cold vessel wall occurred as the interface passed a certain elevation. It was in this region that the maximum wall heat flux occurred.

3.4.2 Test Results for C056402

This test also examined the effects of CMT draindown during depressurization. The CMT was initially full of water, and the initial pressure was 685 psig. The system was depressurized at a rate of 1 psi/sec.

The liquid level in the CMT is shown as a function of time in Figure 3.4-7. At time zero, valve V3 was opened, and the tank drained. The tank was completely empty at 655 seconds.

The CMT pressure is shown in Figure 3.4-8. The tank pressure was stabilized at 685 psig during the initial period, and the tank started to gravity-drain. The pressure was set to the target pressure of 685 psig when valve V3 was opened. The depressurization was initiated at 210 seconds after the test began. The depressurization rate was approximately 1 psi/sec. The final pressure was 198 psia when the CMT was empty. The steam flow into the CMT is also shown in Figure 3.4-8. After an initial flow spike, the steam flow was established at 0.34 lbm/sec 200 seconds after valve V3 was opened. The flow decreased as the tank drained due to the lower rate of discharge flow, reaching 0.12 lbm/sec at the end of draindown. The CMT discharge flow is also shown in Figure 3.4-8. The flow reached a maximum of 2.4 lbm/sec 50 seconds after valve V3 was opened. The flow then decreased due to the decreasing hydrostatic head, reaching 1.7 lbm/sec when the tank was empty.

The axial fluid temperature is shown in Figure 3.4-9. At time zero, the entire tank was at the initial temperature of 78°F. The temperature history at various elevations shows the progression of the liquid/steam interface and the development of a hot liquid layer. The vapor temperature, which was measured at each elevation as the interface passed, decreased from 498°F at the start of draindown to ~410°F when the tank was empty. This was consistent with the reduction of the system pressure. Also shown is the superheating of the steam to temperatures above saturation from the hot tank wall.

The passing of the liquid/steam interface is also shown in Figures 3.4-10 and 3.4-11, which show the wall heat transfer coefficient and heat flux, respectively, as a function of elevation in the CMT vessel. Condensation of the hot steam on the cold vessel wall occurred as the interface passed a certain elevation. It was in this region that the maximum wall heat flux occurred.

Comparing this test to the higher pressure test, it is apparent that the CMT drain rate is not significantly affected by the system pressure.

3.4.3 Test Results for C057403

This test also examined the effects of CMT draindown during depressurization. The CMT was initially full of water, and the initial pressure was 685 psig. For this test, the system was depressurized at a rate of 2-3 psi/sec.

The liquid level in the CMT is shown as a function of time in Figure 3.4-12. At time zero, valve V3 was opened, and the tank drained. The tank was completely empty at 660 seconds.

The CMT pressure is shown in Figure 3.4-13. The pressure was set to 740 psia, which is above the target pressure of 685 psig, when valve V3 was opened. The depressurization was initiated at 240 seconds into the transient after the CMT had started to gravity-drain. The pressure was then reduced at a rate of approximately 1.4 psi/sec, reaching a final pressure of 70 psia when the tank was empty. The steam flow into the CMT is also shown in Figure 3.4-13. After an initial flow spike, the steam flow was established at 0.32 lbm/sec 200 seconds after valve V3 was opened. The steam flow decreased as the tank drained due to the lower rate of discharge flow, reaching 0.04 lbm/sec at the end of draindown. The CMT discharge flow is also shown in Figure 3.4-13. The flow reached a maximum of 2.4 lbm/sec 75 seconds after valve V3 was opened. The flow decreased due to the decreasing hydrostatic head, reaching 1.7 lbm/sec when the tank was empty.

The axial fluid temperature is shown in Figure 3.4-14. At time zero, the entire tank was at the initial temperature of 70°F. The temperature history at various elevations shows the progression of the liquid/steam interface and the development of a hot liquid layer. The vapor temperature, which was measured at each elevation as the interface passed, decreased from 505°F at the start of draindown to 375°F when the tank is empty. This was consistent with the reduction of the system pressure. Also shown is the superheating of the steam to temperatures above saturation from the hot tank wall.

The passing of the liquid/steam interface is also shown in Figures 3.4-15 and 3.4-16, which show the wall heat transfer coefficient and heat flux, respectively, as a function of elevation in the CMT vessel. Condensation of the hot steam on the cold vessel wall occurred as the interface passed a certain elevation. It was in this region that the maximum wall heat flux occurred.

Comparing this test to the previous test with the lower depressurization rate, it is apparent that the CMT drain rate is not significantly affected by the higher rate of depressurization.

3.4.4 Test Results for C058404

This test also examined the effects of CMT draindown during depressurization. The CMT was initially full of water, and the initial pressure was 685 psig. For this test, the system was depressurized at a rate of 0.5 psi/sec.

The liquid level in the CMT is shown as a function of time in Figure 3.4-17. At time zero, valve V3 was opened, and the tank drained. The tank was completely empty at 710 seconds.

The CMT pressure is shown in Figure 3.4-18. The pressure was set to 765 psia, which is above the target pressure of 685 psig, when valve V3 was opened. The depressurization was initiated 230 seconds after the test began at a rate of approximately 0.6 psi/sec, reaching a final pressure of 400 psia when the tank was empty. The steam flow into the CMT is also shown in Figure 3.4-18. After an initial flow spike, the steam flow was established at 0.34 lbm/sec 200 seconds after valve V3 was opened. The steam flow decreased as the tank drained due to the lower rate of discharge flow, reaching 0.2 lbm/sec at the end of draindown. The CMT discharge flow is also shown in Figure 3.4-18. The flow reached a maximum of 2.5 lbm/sec 65 seconds after valve V3 was opened. The flow decreased due to the lower hydrostatic head, reaching 1.5 lbm/sec when the tank was empty.

The axial fluid temperature is shown in Figure 3.4-19. At time zero, the entire tank was at the initial temperature of 75°F. The temperature history at various elevations shows the progression of the liquid/steam interface and the development of a hot liquid layer. The vapor temperature, which was measured at each elevation as the interface passed, decreased from 505°F at the start of draindown to 460°F when the tank was empty. This is consistent with the reduction of the system pressure. For this case, no superheating of the steam to temperatures above saturation from the hot tank wall was found to occur.

The passing of the liquid/steam interface is also shown in Figures 3.4-20 and 3.4-21, which show the wall heat transfer coefficient and heat flux, respectively, as a function of elevation in the CMT vessel. Condensation of the hot steam on the cold vessel wall occurred as the interface passed a certain elevation. It was in this region that the maximum wall heat flux occurred.

Comparing this test to the previous tests, it was found that the CMT draindown time is slightly longer than for the tests with higher depressurization rates.

3.4.5 Conclusions

The following conclusions can be drawn from these analyses of the 400-series tests:

- The CMT draindown rate is not significantly affected by the initial pressure or by the rate of depressurization and is consistent with results obtained from the constant-pressure 300-series tests

- Depressurization causes a reduction in the saturation temperature, which allows the steam to be superheated when coming in contact with the hotter tank wall

TABLE 3.4-1 400-SERIES MATRIX TESTS		
Test Number	**Pressure (psig)**	**Depressurization Rate (psi/sec)**
C055401	1085	1
C056402	685	1
C057403	685	2 to 3
C057404	685	0.5

Figures 3.4-1 through 3.4-21 are not included in the non-proprietary version of this document.

3.5 Analysis of the 500-Series Tests

This section covers the AP600 CMT 500-series matrix tests, which simulate natural circulation prior to CMT draindown and depressurization. The nine tests in the series were run to study the heat-up of the CMT water (natural circulation) and the subsequent behavior of the heated CMT water during CMT draindown and depressurization. The tests were repeated with different drain line resistances, different steam supply pressures, and different fractions of the CMT heated before draindown.

A complete list of the analyzed 500-series tests is provided in Table 3.5-1.

The objectives of the 500-series tests are to:

- Observe and record the rate at which water drains from the CMT during depressurization preceded by heating of the CMT by natural circulation

- Characterize the CMT drain rate as a function of steam pressure (or temperature), depressurization rate, and degree to which the CMT is heated by natural circulation

- Observe and record the behavior of the heated CMT water during draindown and depressurization

3.5.1 Analysis of Test C059502

This test was a natural circulation test conducted at a system pressure of 1085 psig. The drain valve was assumed to be fully opened. The test was terminated when the CMT was one-fifth heated.

The drain flow rate as a function of time, shown in Figure 3.5-1, was considerably lower than the flow expected at the fully open condition. Using the natural circulation model shown in Section 2.9, the expected drain flow was 1.7 lbm/sec. The difference between the expected flow and the measured flow was likely due to the drain line valve V3 being less than fully open. The CMT inlet liquid flow rate is also shown in Figure 3.5-1. The flow was measured at PDT13 and was less than the CMT drain flow by approximately the ratio of the hot-to-cold fluid density. The CMT vessel pressure is also shown in Figure 3.5-1 and remained near the target pressure over the course of the test.

The axial fluid temperature distribution as a function of time is shown in Figure 3.5-2. From these plots, it is possible to determine the position and thickness of the hot fluid layer as the natural circulation transient progressed.

This hot liquid layer development is also shown in Figures 3.5-3 and 3.5-4, which show the wall heat transfer coefficient and heat flux, respectively, as a function of elevation in the CMT vessel. Heat transfer was at a maximum as the hot liquid layer passed the cold CMT wall and was nearly zero in the hot region of the CMT and in the cold region of the CMT.

3.5.2 Analysis of Test C061504

This test was a natural circulation test conducted at a system pressure of 1085 psig. The drain valve was assumed to be fully opened. The test was to be terminated when the CMT was one-half heated.

The drain flow rate as a function of time, shown in Figure 3.5-5, was considerably lower than the flow expected at the fully open condition. Using the natural circulation model shown in Section 2.9, the expected drain flow was 1.7 lbm/sec. The difference between the expected flow and the measured flow was likely due to the drain line valve V3 being less than fully open. The CMT inlet liquid flow rate is also shown in Figure 3.5-5. Where available, the flow was measured at PDT13 and was less than the CMT drain flow by approximately the ratio of the hot-to-cold fluid density. The CMT vessel pressure is also shown in Figure 3.5-5 and remained near the target pressure over the course of the test.

The axial fluid temperature distribution as a function of time is shown in Figure 3.5-6. From these plots, it is possible to determine the position and thickness of the hot fluid layer as the natural circulation transient progressed.

This hot liquid layer development is also shown in Figures 3.5-7 and 3.5-8, which show the wall heat transfer coefficient and heat flux, respectively, as a function of elevation in the CMT vessel. Heat transfer was at a maximum as the hot liquid layer passed the cold CMT wall and was nearly zero in the hot region of the CMT and in the cold region of the CMT.

3.5.3 Analysis of Test C064506

This test was a natural circulation test conducted at a system pressure of 1085 psig. The drain valve was assumed to be fully opened. The test was to be terminated when the CMT was fully heated.

The drain flow rate as a function of time, shown in Figure 3.5-9, was initially 1.7 lbm/sec, which was predicted by the natural circulation model. The flow dropped rapidly as the hot water from the S/WR replaced the cold CMT water, and the buoyancy driving head was reduced. The CMT inlet liquid flow rate is also shown in Figure 3.5-9. Where available, the flow was measured at PDT13 and was less than the outlet flow by approximately the ratio of the hot-to-cold fluid density. The CMT vessel pressure is also shown in Figure 3.5-9 and remained near the target pressure over the course of the test.

The axial fluid temperature distribution as a function of time is shown in Figure 3.5-10. From these plots, it is possible to determine the position and thickness of the hot fluid layer as the natural circulation transient progressed. At the end of the test, the tank was fully heated to near-saturation conditions.

This hot liquid layer development is also shown in Figures 3.5-11 and 3.5-12, which show the wall heat transfer coefficient and heat flux, respectively, as a function of elevation in the CMT vessel. Heat transfer was at a maximum as the hot liquid layer passed the cold CMT wall and was nearly zero in the hot region of the CMT and in the cold region of the CMT.

3.5.4 Analysis of Test C065506

This test was a draindown test conducted at a system pressure of 1085 psig. The tank was to be drained while depressurizing at a rate of 1.5 psi/sec followed by a slower rate of 0.5 psi/sec. The drain valve was to be fully opened to produce a target initial drain rate of 16 gpm. The test was to be terminated when the CMT vessel was completely drained. The CMT was assumed to be fully heated initially.

The drain flow rate as a function of time, shown in Figure 3.5-13, was initially 2.2 lbm/sec and decreased to 1.7 lbm/sec at the end of draindown. The CMT inlet steam flow rate is also shown in Figure 3.5-13. The flow was measured in steam line 1 and was quite noisy. This may have been due to fluctuations in the system pressure resulting from the depressurization. The CMT vessel pressure is also shown in Figure 3.5-13 and remained constant during the first 100 seconds. The pressure then dropped rapidly to approximately 700 psia at 220 seconds. There was considerable variation in the pressure during the time period from 220 seconds to 300 seconds. The pressure dropped at a similar rate reaching 500 psia at 500 seconds, which was the end of the CMT draindown.

The CMT liquid level is shown in Figure 3.5-14. The level dropped at a constant rate, and the CMT was empty at approximately 520 seconds.

The axial fluid temperature distribution as a function of time is shown in Figure 3.5-15. The temperatures were nearly constant throughout the draindown, since the tank was initially at saturated conditions. Temperatures at the end of the transient were lower due to the reduction in the saturated temperature resulting from the depressurization.

Condensation of the hot steam on the cold vessel occurred as the interface passed a certain elevation. It was in this region that the maximum wall heat flux occurred.

3.5.5 Analysis of Test C066501

This test was a natural circulation test conducted at a system pressure of 1085 psig. The drain valve was assumed to be partially opened.

The drain flow rate as a function of time, shown in Figure 3.5-18, was initially 1.5 lbm/sec., which was predicted by the natural circulation model. The flow then dropped as the hot water from the S/WR replaced the cold CMT water, and the buoyancy driving head was reduced. The CMT inlet liquid flow rate is also shown in Figure 3.5-18. The flow was measured at PDT13 and was less than the outlet flow by approximately the ratio of the hot-to-cold fluid density. The CMT vessel pressure is also shown in Figure 3.5-18 and fluctuated around the target pressure over the course of the test.

The axial fluid temperature distribution as a function of time is shown in Figure 3.5-19. From these plots, it is possible to determine the position and thickness of the hot fluid layer as the natural circulation transient progressed. At the end of the test, the tank was one-fifth heated.

This hot liquid layer development is also shown in Figures 3.5-20 and 3.5-21, which show the wall heat transfer coefficient and heat flux, respectively, as a function of elevation in the CMT vessel. Heat transfer was at a maximum as the hot liquid layer passed the cold CMT wall and was nearly zero in the hot region of the CMT and in the cold region of the CMT.

3.5.6 Analysis of Test C067501

This test was a draindown test conducted at a system pressure of 1085 psig. The tank was to be drained while depressurizing at a rate of 1.5 psi/sec followed by a slower rate of 0.5 psi/sec. The drain valve was assumed to be partially opened to produce a target initial drain rate of 6 gpm. The CMT was assumed to be one-fifth filled with hot water initially. The test was to be terminated when the CMT vessel was completely drained.

The drain flow rate as a function of time, shown in Figure 3.5-22, was initially 0.8 lbm/sec and dropped to 0.6 lbm/sec at the end of draindown. The CMT inlet steam flow rate is also shown in Figure 3.5-22. The flow was measured in steam line 1 and was quite noisy. The CMT vessel pressure is also shown in Figure 3.5-22 and remained constant during the first 250 seconds. The pressure then dropped rapidly to approximately 650 psia at 500 seconds, raised rapidly to 800 psia, then dropped again reaching 50 psia at the end of the CMT draindown.

The CMT liquid level is shown in Figure 3.5-23. The level dropped at a constant rate, and the CMT was empty at approximately 1530 seconds. There was essentially no effect of depressurization on the draindown rate.

The axial fluid temperature distribution as a function of time is shown in Figure 3.5-24. The temperature at the top of the tank was equal to the saturation temperature of the steam. As the tank drained, the liquid in the bottom of the tank increased in temperature due to the interfacial heat transfer between the steam and liquid and the axial heat conduction from the hot tank walls at the top of the tank.

The passing of the liquid/steam interface is also shown in Figures 3.5-25 and 3.5-26, which show the wall heat transfer coefficient and heat flux, respectively as a function of elevation in the CMT vessel. Condensation of the hot steam on the cold vessel occurred as the interface passed a certain elevation. It was in this region that the maximum wall heat flux occurred.

3.5.7 Analysis of Test C068503

This test was a natural circulation test conducted at a system pressure of 1085 psig. The drain valve was assumed to be partially opened.

The drain flow rate as a function of time, shown in Figure 3.5-27, was initially 1.7 lbm/sec. The flow dropped as the hot water from the S/WR replaced the cold CMT water, and the buoyancy driving head was reduced. The CMT inlet liquid flow rate is also shown in Figure 3.5-27. The flow was measured at PDT13 and was less than the CMT drain flow by approximately the ratio of the hot-to-cold fluid density. The CMT vessel pressure is also shown in Figure 3.5-27 and was nearly constant at the target pressure over the course of the test.

The axial fluid temperature distribution as a function of time is shown in Figure 3.5-28. From these plots, it is possible to determine the position and thickness of the hot fluid layer as the natural circulation transient progressed. At the end of the test, the tank was one-half heated.

This hot liquid layer development is also shown in Figures 3.5-29 and 3.5-30, which show the wall heat transfer coefficient and heat flux, respectively, as a function of elevation in the CMT vessel. Heat transfer was at a maximum as the hot liquid layer passed the cold CMT wall and was nearly zero in the hot region of the CMT.

3.5.8 Analysis of Test C069503

This test was a draindown test conducted at a system pressure of 1085 psig. The tank is to be drained while depressurizing at a rate of 1.5 psi/sec followed by a slower rate of 0.5 psi/sec. The drain valve is assumed to be partially opened to produce a target initial drain rate of 6 gpm. The CMT is assumed to be half-filled with hot water initially. The test is to be terminated when the CMT vessel is completely drained.

The drain flow rate as a function of time, is shown in Figure 3.5-31, was initially 0.85 lbm/sec. and dropped to 0.62 lbm/sec at the end of draindown. The CMT inlet steam flow rate is also shown in Figure 3.5-31. The flow was measured in steam line 1 and was quite noisy. This may have been due to fluctuations in the system pressure, resulting from the depressurization. The CMT vessel pressure is also shown in Figure 3.5-31 and remained constant during the first 200 seconds. The pressure dropped rapidly to approximately 610 psia at 400 seconds and then dropped again reaching 330 psia at the end of the CMT draindown.

The CMT liquid level is shown in Figure 3.5-32. The level dropped at a constant rate, and the CMT was empty at approximately 1220 seconds. There was no significant change in the draindown rate after the initiation of depressurization.

The axial fluid temperature distribution as a function of time is shown in Figure 3.5-33. The temperature at the top of the tank was equal to the saturation temperature of the steam. As the tank drained, the liquid in the bottom of the tank increased in temperature due to the interfacial heat transfer between the steam and liquid and the axial heat conduction from the hot tank walls at the top of the tank.

The passing of the liquid/steam interface is also shown in Figures 3.5-34 and 3.5-35, which show the wall heat transfer coefficient and heat flux, respectively, as a function of elevation in the CMT vessel. Condensation of the hot steam on the cold vessel occurred as the interface passed a certain elevation. It was in this region that the maximum wall heat flux occurred.

3.5.9 Analysis of Test C070505

This test was a natural circulation test conducted at a system pressure of 1085 psig. The drain valve was assumed to be partially opened.

The drain flow rate as a function of time, shown in Figure 3.5-36, was initially 1.7 lbm/sec. The flow drops as the hot water from the S/WR replaced the cold CMT water, and the buoyancy driving head was reduced, reaching about 0.25 lbm/sec at 2000 seconds. The CMT inlet liquid flow rate is also shown in Figure 3.5-36. The flow was measured at PDT13 and was less than the CMT drain flow by approximately the ratio of the hot-to-cold fluid density. The CMT vessel pressure is also shown in Figure 3.5-36 and was nearly constant at the target pressure over the course of the test.

The axial fluid temperature distribution as a function of time is shown in Figure 3.5-37. From these plots, it is possible to determine the position and thickness of the hot fluid layer as the natural circulation transient progressed. At the end of the test, the tank was fully heated.

This hot liquid layer development is also shown in Figures 3.5-38 and 3.5-39, which show the wall heat transfer coefficient and heat flux, respectively, as a function of elevation in the CMT vessel. Heat transfer was at a maximum as the hot liquid layer passed the cold CMT wall and was nearly zero in the hot region of the CMT.

3.5.10 Analysis of Test C071505

This test was a draindown test conducted at a system pressure of 1085 psig. The tank was to be drained while depressurizing at a rate of 1.5 psi/sec followed by a slower rate of 0.5 psi/sec. The drain valve was assumed to be partially opened to produce a target initial drain rate of 6 gpm. The CMT was assumed to be completely filled with hot water initially. The test is to be terminated when the CMT vessel was completely drained.

The drain flow rate as a function of time, shown in Figure 3.5-40, was initially 0.79 lbm/sec and dropped to 0.62 lbm/sec at the end of draindown. The CMT inlet steam flow rate is also shown in Figure 3.5-40. The flow was measured in steam line 1 and was quite noisy. This may be due to fluctuations in the system pressure, resulting from the depressurization. The CMT vessel pressure is also shown in Figure 3.5-40 and remained constant during the first 200 seconds. The pressure dropped rapidly to approximately 530 psia at 570 seconds and then dropped again less rapidly, reaching 300 psia at the end of the CMT draindown.

The CMT liquid level is shown in Figure 3.5-41. The level dropped at a constant rate, and the CMT was empty at approximately 1260 seconds. Once again, there was no discernable effect of depressurization on the draindown rate.

The axial fluid temperature distribution as a function of time is shown in Figure 3.5-42. The temperatures were nearly constant throughout the draindown, since the tank was initially at saturated conditions. Temperatures at the end of the transient were lower due to the reduction in the saturated temperature resulting from the depressurization.

The wall heat transfer coefficient and heat flux are shown in Figures 3.5-43 and 3.5-44. Since the tank was initially hot and very little heat transfer occurred between the fluid and the tank walls.

3.5.11 Analysis of Test C072509

This test was a natural circulation test conducted at a system pressure of 1835 psig. The drain valve was assumed to be fully opened. The test was to be terminated when the CMT was fully heated.

The drain flow rate as a function of time, shown in Figure 3.5-45, was initially 1.9 lbm/sec and dropped to 0.2 lbm/sec at the end of the transient. This reduction was due to the decrease in the buoyancy driving head as the cold CMT water was replaced by the hot S/WR water. The CMT inlet liquid flow rate is also shown in Figure 3.5-45. The flow was measured at PDT13 and was less than the outlet flow by approximately the ratio of the hot-to-cold fluid density. The CMT vessel pressure is also shown in Figure 3.5-45 and fluctuated around the target pressure over the course of the test.

The axial fluid temperature distribution as a function of time is shown in Figure 3.5-46. From these plots, it is possible to determine the position and thickness of the hot fluid layer as the natural circulation transient progressed.

This hot liquid layer development is also shown in Figures 3.5-47 and 3.5-48, which show the wall heat transfer coefficient and heat flux, respectively, as a function of elevation in the CMT vessel. Heat transfer was at a maximum as the hot liquid layer passed the cold CMT wall and was nearly zero in the hot region of the CMT and in the cold region of the CMT.

3.5.12 Analysis of Test C073509

This test was a draindown test conducted at a system pressure of 1835 psig. The tank was to be drained while depressurizing at a rate of 1.5 psi/sec followed by a slower rate of 0.5 psi/sec. The drain valve was to be fully opened to produce a target initial drain rate of 16 gpm. The CMT was assumed to be completely filled with hot water initially. The test was to be terminated when the CMT vessel was totally drained.

The drain flow rate as a function of time, shown in Figure 3.5-49, was initially 2.1 lbm/sec and fell to 1.6 lbm/sec at the end of draindown. The CMT inlet steam flow rate is also shown in Figure 3.5-49.

The flow was measured in steam line 1. The CMT vessel pressure is also shown in Figure 3.5-49 and remained constant during the first 100 seconds. The pressure then dropped rapidly to approximately 520 psia at the end of draindown.

The CMT liquid level is shown in Figure 3.5-50. The level dropped at a constant rate, and the CMT was empty at approximately 480 seconds. No effect of the depressurization was observed on the draindown rate.

The axial fluid temperature distribution as a function of time is shown in Figure 3.5-51. The temperatures were nearly constant throughout the draindown, since the tank was initially at saturated conditions. Temperatures at the end of the transient were lower due to the reduction in the saturated temperature resulting from the depressurization.

The wall heat transfer coefficient and heat flux are shown in Figures 3.5-52 and 3.5-53. Condensation of the hot steam on the cold vessel occurred as the interface passed a certain elevation. It was in this region that the maximum wall heat flux occurred.

3.5.13 Analysis of Test C074508

This test was a natural circulation test conducted at a system pressure of 1835 psig. The drain valve was assumed to be fully opened. The test was to be terminated when the CMT was one-half heated.

The drain flow rate as a function of time, shown in Figure 3.5-54, was 1.9 lbm/sec initially and fell to 1.3 lbm/sec at the end of the test. This reduction was due to the decrease in the buoyancy driving head as the cold CMT water was replaced by the hot S/WR water. The CMT inlet liquid flow rate is also shown in Figure 3.5-54. Where available, the flow was measured at PDT13 and was less than the CMT drain flow by approximately the ratio of the hot-to-cold fluid density. The CMT vessel pressure is also shown in Figure 3.5-54 and remained near the target pressure over the course of the test.

The axial fluid temperature distribution as a function of time is shown in Figure 3.5-55. From these plots, it is possible to determine the position and thickness of the hot fluid layer as the natural circulation transient progressed.

This hot liquid layer development is also shown in Figures 3.5-56 and 3.5-57, which show the wall heat transfer coefficient and heat flux, respectively, as a function of elevation in the CMT vessel. Heat transfer was at a maximum as the hot liquid layer passed the cold CMT wall and was nearly zero in the hot region of the CMT and in the cold region of the CMT.

3.5.14 Analysis of Test C075508

This test was a draindown test conducted at a system pressure of 1835 psig. The tank was to be drained while depressurizing at a rate of 1.5 psi/sec followed by a slower rate of 0.5 psi/sec. The drain valve was to be fully opened to produce a target initial drain rate of 16 gpm. The CMT was

assumed to be one-half filled with hot water initially. The test was to be terminated when the CMT vessel was completely drained.

The drain flow rate as a function of time, shown in Figure 3.5-58, was 2.3 lbm/sec at the start of the test and fell to 1.5 lbm/sec at the end of draindown. The CMT inlet steam flow rate is also shown in Figure 3.5-58. The flow was measured in steam line 1. The CMT vessel pressure is also shown in Figure 3.5-58 and remained constant during the first 100 seconds. The pressure then dropped to approximately 900 psia at the end of draindown.

The CMT liquid level is shown in Figure 3.5-59. The level dropped at a constant rate, and the CMT was empty at approximately 520 seconds. There was no observed effect of the depressurization on the draindown rate.

The axial fluid temperature distribution as a function of time is shown in Figure 3.5-60. The temperature at the top of the tank was equal to the saturation temperature of the steam. At the start of draindown, the liquid in the bottom of the tank was heated to approximately 300°F. The top of the tank was at saturation temperature. Consequently, the tank fluid temperatures remained high throughout the test.

The passing of the liquid/steam interface is also shown in Figures 3.5-61 and 3.5-62, which show the wall heat transfer coefficient and heat flux, respectively, as a function of elevation in the CMT vessel. Condensation of the hot steam on the cold vessel occurred as the interface passed a certain elevation. It was in this region that the maximum wall heat flux occurred.

3.5.15 Analysis of Test C076507

This test was a natural circulation test conducted at a system pressure of 1835 psig. The drain valve was assumed to be fully opened.

The drain flow rate as a function of time, shown in Figure 3.5-63, was initially 1.95 lbm/sec and dropped to 1.8 lbm/sec at the end of the test. The CMT inlet liquid flow rate is also shown in Figure 3.5-63. Where available, the flow was measured at PDT13 and was less than the outlet flow by approximately the ratio of the hot-to-cold fluid density. The CMT vessel pressure is also shown in Figure 3.5-63 and remained near the target pressure over the course of the test.

The axial fluid temperature distribution as a function of time is shown in Figure 3.5-64. From these plots, it is possible to determine the position and thickness of the hot fluid layer as the natural circulation transient progressed. At the end of the test, the tank was one-fifth filled with hot water.

This hot liquid layer development is also shown in Figures 3.5-65 and 3.5-66, which show the wall heat transfer coefficient and heat flux, respectively, as a function of elevation in the CMT vessel. Heat transfer was at a maximum as the hot liquid layer passed the cold CMT wall.

3.5.16 Analysis of Test C077507

This test was a draindown test conducted at a system pressure of 1835 psig. The tank was to be drained while depressurizing at a rate of 1.5 psi/sec, followed by a slower rate of 0.5 psi/sec. The drain valve was to be fully opened to produce a target initial drain rate of 16 gpm. The CMT was assumed to be one-fifth heated initially. The test was to be terminated when the CMT vessel was completely drained.

The drain flow rate as a function of time is shown in Figure 3.5-67. The flow was initially 2.4 lbm/sec and decreased to 1.5 lbm/sec at the end of draindown. The CMT inlet steam flow rate is also shown in Figure 3.5-67. The flow was measured in steam line 1. The CMT vessel pressure is also shown in Figure 3.5-67 and remained constant during the first 150 seconds. The pressure then dropped rapidly to approximately 700 psia at the end of the CMT draindown.

The CMT liquid level is shown in Figure 3.5-68. The level dropped at a constant rate, and the CMT was empty at approximately 550 seconds. No effect on the draindown rate was observed due to the depressurization.

The axial fluid temperature distribution as a function of time is shown in Figure 3.5-69. The temperature at the top of the tank was equal to the saturation temperature of the steam. As the tank drained, the liquid in the bottom of the tank increased in temperature due to the interfacial heat transfer between the steam and liquid and due to axial heat conduction from the hot tank walls at the top of the tank.

The passing of the liquid/steam interface is also shown in Figures 3.5-70 and 3.5-71, which show the wall heat transfer coefficient and heat flux, respectively, as a function of elevation in the CMT vessel. Condensation of the hot steam on the cold vessel occurred as the interface passed a certain elevation. It was in this region that the maximum wall heat flux occurred.

3.5.17 Conclusions

- With the exceptions of tests C059502 and C061504, the natural circulation tests performed as expected.

- As was observed in the 300-series tests, the CMT drain rate is largely independent of system pressure.

- As was observed in the 400-series tests, the CMT drain rate is unaffected by system depressurization and is roughly the same regardless of the initial hot water fraction in the CMT.

TABLE 3.5-1 500-SERIES MATRIX TESTS				
Test Run Number	**Test Type**	**CMT Drain Rate (gpm)**	**Steam Supply Pressure(psig)**	**Conditions**
C059502	Natural Circ.	16	1085	Natural Circ. until 1/5 CMT heated
C061504	Natural Circ.	16	1085	Natural Circ. until 1/2 CMT heated
C064506	Natural Circ.	16	1085	Natural Circ. until CMT fully heated
C065506	Drain/Depress.	16	1085 followed by depress. to 20	1.5/0.5 psi/sec nominal depress. rate
C066501	Natural Circ.	6	1085	Natural Circ. until 1/5 CMT heated
C067501	Drain/Depress.	6	1085 followed by depress. to 20	1.5/0.5 psi/sec nominal depress. rate
C068503	Natural Circ.	6	1085	Natural Circ. until 1/2 CMT heated
C069503	Drain/Depress.	6	1085 followed by depress. to 20	1.5/0.5 psi/sec nominal depress. rate
C070505	Natural Circ.	6	1085	Natural Circ. until CMT fully heated
C071505	Drain/Depress.	6	1085 followed by depress. to 20	1.5/0.5 psi/sec nominal depress. rate
C072509	Natural Circ.	16	1835	Natural Circ. until CMT fully heated
C073509	Drain/Depress.	16	1835 followed by depress. to 20	1.5/0.5 psi/sec nominal depress. rate
C074508	Natural Circ.	16	1835	Natural Circ. until 1/2 CMT heated
C075508	Drain/Depress.	16	1835 followed by depress. to 20	1.5/0.5 psi/sec nominal depress. rate
C076507	Natural Circ.	16	1835	Natural Circ. until 1/5 CMT heated
C077507	Drain/Depress.	16	1835 followed by depress. to 20	1.5/0.5 psi/sec nominal depress. rate

Figures 3.5-1 through 3.5-71 are not included in the non-proprietary version of this document.

4.0 PHENOMENOLOGICAL MODELING RESULTS

4.1 Introduction

This section discusses the detailed analysis of the test data and comparisons of the data to literature correlations and models. The discussion also indicates the key thermal-hydraulic phenomena that were observed in the experiments and relates these phenomena back to the core makeup tank (CMT) phenomena identification and ranking table (PIRT) given in the CMT Scaling Report.[2] This discussion closes the process of identifying phenomena, performing the experiments to capture the phenomena, and the analysis of the data to describe and understand the key thermal-hydraulic phenomena for the CMT test.

4.2 Steam-Region Wall Heat Transfer

The test data from the 100-series tests were reduced and analyzed to obtain the local wall heat flux from an inverse conduction calculation using the measured temperature-time histories, as shown in Section 3.2. Condensation heat transfer coefficients at five different CMT elevations were determined from the local heat flux calculations for the tests. A fitting routine was used to interpolate the wall heat flux data between the measuring points, such that the integrated heat flux and heat transfer coefficient could be obtained for the tests. The calculated heat flux and temperature data were also used to obtain the condensate flow rates, so that quantities such as the film flow Reynolds number could be calculated from the data for each test. The film flow Reynolds number is defined as:

$$Re_\Gamma = \frac{4\Gamma_z}{\mu_f} \tag{4.2-1}$$

where:

Γ_z = film flow per unit of wall perimeter
μ_f = liquid viscosity

The data, when reduced into the format as described above, can then be compared to the Nusselt laminar film condensation correlation[5] for the wall condensation on the CMT walls. The correlation is given as:

$$\overline{h_f} = 0.925 \left[\frac{4\,\rho_f\,(\rho_f - \rho_g)\,g\,k_f^3}{\mu_f^2\,Re_\Gamma} \right]^{1/3} \tag{4.2-2}$$

where:

k_f = liquid thermal conductivity
ρ_f = liquid density

ρ_g = vapor density
h_{fg} = latent heat of vaporization
μ_f = liquid viscosity
T_w = wall temperature
T_{gi} = liquid-vapor interface temperature taken at saturation
Θ = angle between the wall and the horizontal
Z = height of the wall
g = acceleration due to gravity

The derivation of this equation includes the relationship between local and average heat transfer coefficients:

$$h_{local} = \frac{3}{4} \overline{h_f} \tag{4.2-3}$$

The 100-series CMT test data were analyzed to calculate the local wall condensation heat transfer coefficients. To eliminate the ambiguity of interpolation of heat transfer correlation between wall temperature measurement locations, the local heat transfer coefficients at those measurement locations were compared with the local coefficient form of Nusselt's correlation. The test local heat transfer coefficient was then normalized as:

$$\frac{h_{local}}{k_f}\left[\frac{\mu_f^2}{\rho_f(\rho_f-\rho_g)g}\right]^{1/3} \tag{4.2-4}$$

The heat transfer data from the 100-series tests are shown, plotted as the normalized heat transfer coefficient against the film Reynolds number, in Figures 4.2-1 to 4.2-7 for each of the instrumented locations on the CMT. These locations, designated REQ 0, 1, 2, 3, 4, are respectively 113.9 in. and 102.8 in., 86.1 in., 57.3 in., and 22.8 in. above the inside bottom of the CMT. The test data were normalized using the equations given above. The solid line is the Nusselt laminar film condensation correlation, and the data are seen to agree with this correlation or lie below the correlation. The data also tend to agree with the Nusselt correlation at film Reynolds numbers that are greater than 2000, which would be the transition to turbulent flow. The literature indicates that as the film Reynolds number exceeds 2000, the film becomes turbulent and the condensation heat transfer coefficient, which is just the inverse of the thermal resistance of the film, increases.[12,13,14] The heat transfer data from the CMT test indicate that instead of increasing with increased film Reynolds numbers, the heat transfer coefficient is constant.

In Figures 4.2-2, 4.2-3, and 4.2-4, the normalized heat transfer coefficient in the dome is shown starting at a value of unity, well above the correlation line, and dropping toward the line as the transient progresses. Some wall locations show this trend. For higher pressure 100-series tests, two effects tend to result in a high uncertainty in, and exaggeration of, the calculated heat transfer coefficient during the initial few tens of seconds while the CMT temperatures are rising rapidly. The first effect is the location of the steam distributor with respect to the fluid thermocouple used in the

heat transfer coefficient calculation. This thermocouple was chosen because of its proximity to the dome metal surface thermocouple. It is postulated that steam jetting from the distributor bypasses this thermocouple and impinges on the wall and on other fluid thermocouples. The temperature of this thermocouple is actually below the wall temperature and other nearby fluid temperatures for about 15 seconds in test C042104. During this period, the heat transfer coefficient is not calculated. However, immediately thereafter, the heat transfer coefficient is calculated based on a temperature difference rising from zero, which is probably a very small fraction of the difference between the true adjacent temperature and the wall surface. Thus, the calculated heat transfer coefficient is probably much larger than the true heat transfer coefficient at this time. A second effect is a small inaccuracy in the fluid and wall thermocouples, which results in large additional heat transfer coefficient uncertainty when the measured temperature difference is very small. After about 30 to 40 seconds into the transient, when the measured temperatures are more uniform, both of these effects are much less significant, and the normalized heat transfer coefficient is much closer to the correlation line.

Figures 4.2-8 to 4.2-11 show the composite plot of the normalized wall heat transfer for all the elevations for each 100-series test that does not have the noncondensible gas initially in the CMT. Figure 4.2-12 shows the composite plot of all these 100-series tests together. As Figure 4.2-12 indicates, the normalized wall condensation heat transfer data lie at or below the Nusselt film condensation correlation. The majority of the data are at film Reynolds numbers of less than 2000, such that the laminar film model of Nusselt should apply. The normalization process reduced the small pressure effects observed in the individual data sets at different pressures, such that the data can be considered as a single set. The Nusselt film condensation correlation is recommended for calculating the condensation heat transfer to the CMT walls.

The heat transfer coefficient data from the experiments with the initial air concentrations were also normalized in the same fashion as the previous 100-series test. Individual plots of the normalized heat transfer from the experiments with air initially in the tank are shown in Figures 4.2-13 to 4.2-15. There is no observable trend of the presence of the noncondensible gas on the wall condensation heat transfer.

The work by Sparrow, et al.[15] has shown the effects of noncondensible gases on the condensation heat transfer coefficient for stagnant steam situations as well as forced-convective steam situations. Figure 4.2-16 from Collier's book[16] shows the results of Sparrow's calculations where the y axis is the heat flux ratio, with ϕ being the heat flux with noncondensibles and ϕ_o the reference heat flux without noncondensibles. As the figure indicates, the effects of noncondensibles in stagnant conditions is to sharply reduce the condensation heat transfer coefficient. In a flowing situation, there was some reduction of the wall condensation heat transfer, but the effect was not as significant since the flow mixes, the boundary layer, and the heat transfer process were not dependent on the diffusion of the steam through the noncondensibles. In order to further investigate the noncondensible gas effects on the wall condensation heat transfer, the individual calculated wall heat flux values for the tests with air initially in the CMT, were compared to the heat flux from test C047101, which had no noncondensible gases in the tank. The effect of the initial air was most significant at the bottom of the tank, which is where the air was pushed by the steam. Therefore, the wall temperature at elevation no. 4 near the tank bottom was examined to see the effect of the noncondensible gas on the condensation heat flux. The heat flux at the bottom-most location was plotted for tests C044106, C045107, and C046108 and

was compared to the heat flux from test C047101. Comparisons of the heat fluxes are shown in Figures 4.2-17 to 4.2-19. As these figures indicate, the wall heat flux for the tests with noncondensibles was depressed early in time, and was less than the heat flux from test C047101, which did not have any air initially in the tank. The heat flux ratio was calculated for the early portion of the transient when the noncondensibles were present.

The ratio of initial air pressure to transient total CMT pressure was also calculated during the first 300 seconds of the transient to find the mass fraction of the air in the CMT. The heat flux ratios for the tests with air to the reference test were then be plotted against the air mass fraction and compared with the data from Sparrow's analysis. The key assumption was that the CMT was homogeneously mixed, while in reality, the air was being displaced toward the bottom of the tank. Figure 4.2-20 shows the plot of the ratio of the heat flux from the tests with air to the reference test with no air, plotted against the estimated air mass fraction that was calculated from the pressure ratio. Also shown on the plot are the lines from Sparrow's analysis taken from Figure 4.2-16. The majority of the data lie between the forced convection and the stagnant steam conditions calculated by Sparrow. As the data indicated, when the mass ratio of air was large, the heat flux ratio was small, indicating that wall condensation was impeded by the presence of the noncondensible gas. As time progressed, more steam entered the CMT and pushed the air below the measuring location, so that the effect of the air was reduced and the heat flux ratio approached unity. The heat flux plots shown in Figures 4.2-17 to 4.2-19 indicate that once the noncondensible gas had been pushed below the last CMT wall measuring elevation, the calculated wall heat flux for the tests with air in the tank could exceed the reference no-air test. This occurred because at early times, the air reduced the initial condensation heat transfer. After the air was pushed below the measuring station, the wall was colder, such that the condensing heat flux was larger.

Wall condensation heat transfer coefficients were also calculated from the 300-series tests once the CMT began to drain. During the initial period of the 300-series tests, the steam was injected into the CMT water, condensing and heating the water to near the saturation temperature. Once the water was hot, the rapid condensation at the top of the CMT ceased, and the CMT began to drain. As the CMT drained, the hot water layer at the top of the CMT transferred heat to the colder CMT walls. Steam condensed on the wall surface that was exposed above the receding water level. Once the hot liquid layer drained past a wall measuring position, the effect of steam condensing on the cooler CMT wall could be observed. The wall heat flux data from the 300-series tests were used to calculate the wall condensation heat transfer coefficients in the same manner as the 100-series tests. The normalized wall condensation heat transfer coefficients for all positions on the CMT and the corresponding film Reynolds numbers were calculated using Equations 4.2-1 to 4.2-4. The resulting normalized wall condensation heat transfer coefficients for the 300-series tests are shown in Figure 4.2-21 to 4.2-25 for pressures from 25 psia to 1100 psia. As the plots indicate, the majority of the normalized condensation heat transfer data lie below the Nusselt film condensation heat transfer correlation for nearly all film Reynolds numbers. Most of the data are for film Reynolds numbers that are less than 2000, making the Nusselt laminar film condensation correlation applicable. These results are consistent with the results for the 100-series tests.

Figures 4.2-1 through 4.2-15 are not included in the non-proprietary version of this document.

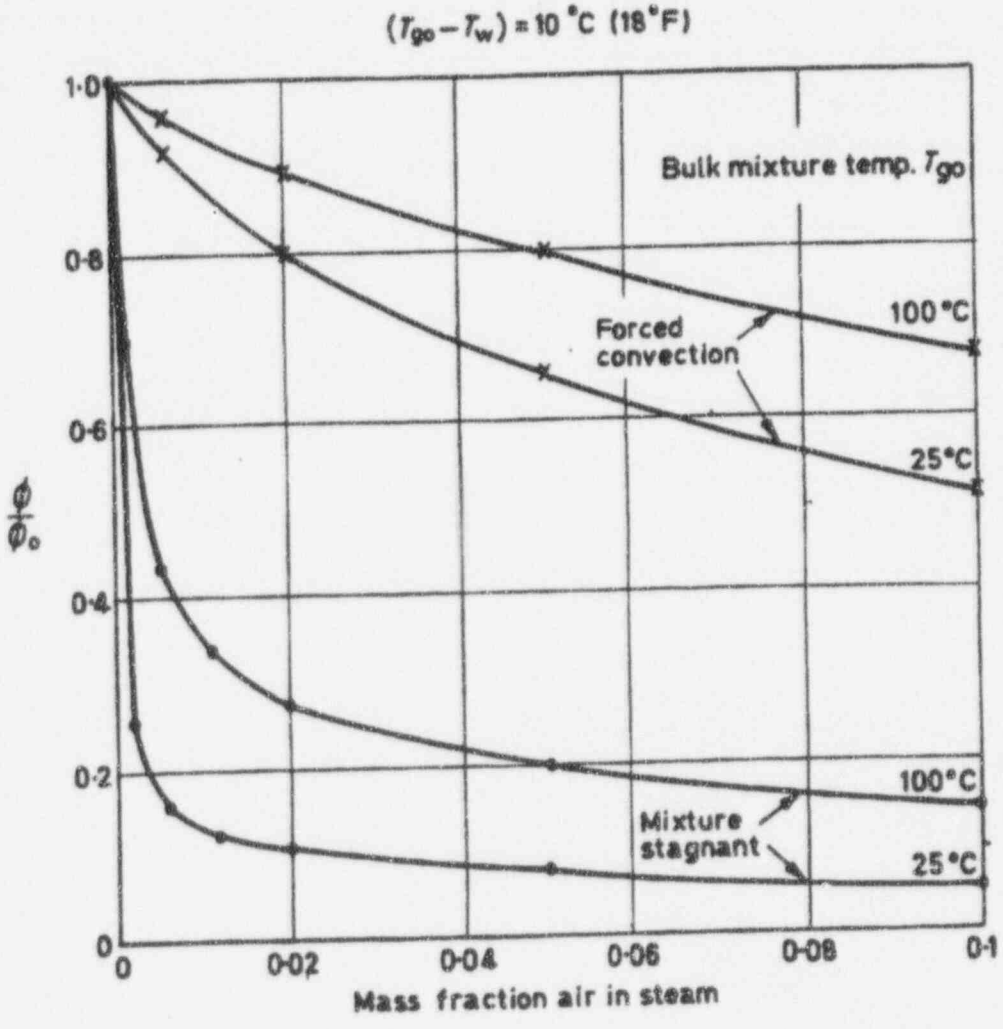

Figure 4.2-16 Effects of Noncondensible Gases on Wall Condensation from Sparrow, et al.

Figures 4.2-17 through 4.2-25 are not included in the non-proprietary version of this document.

4.3 Mixing Characteristics in 300-Series Tests

For CMT tests in which steam was injected to a CMT full of cold water from a nominally constant pressure source, one of the questions that arose was how to predict the time delay before rapid CMT draining began. This section discusses the trends observed and provides an explanation for some of these trends.

The following observations and comments are based on the plots of steam and drain flow rates, pressure, water level, and axial temperature distribution, in Section 3.3.

- There was a period of high-steam flow and low-drain flow, during which steam was mixed and condensed in the top of the CMT. During this time, most of the elevation head available to force fluid into and out of the CMT was consumed by steam flow, resulting in a reduction in CMT pressure. The depth of mixing affected the time delay before free draining and resulted in more subcooled water mixing with the steam and delaying the approach of the CMT water toward saturation.

  The top graph of Figure 4.3-1 summarizes the approximate mixing depth as a function of nominal reservoir pressure and nominal drain rate, which characterized drain line resistance. This mixing depth is taken from plots and transient fluid temperature graphs. The general trend was the mixing depth increased as the system pressure decreased.

  One explanation for the mixing depth behavior is that the momentum of steam entering the CMT radially through the holes in the steam distributor was transmitted to the CMT water and deflected into vertical momentum by the curvature of the CMT top dome. Thus, the mixing depth could be roughly proportional to the maximum momentum of steam entering the CMT. The trend of the steam momentum can be estimated independently as follows:

  - There was a pressure balance between the available elevation head, pressure drop through the steam line, and pressure drop through the drainline. The elevation head was roughly constant. The pressure drop through the steamline was related to steamline flow resistance and the momentum head of steam in the pipe. During the rapid condensation period, the drain volume flow rate matched the rate of condensation of steam plus the expansion of water heated by absorbing the latent heat of vaporization, if steam completely condensed and mixed. With constant steamline resistance, this balance dictated that steam momentum decreased continuously with increasing pressure. This is because at higher pressure and density, the steam momentum per unit mass flow was lower, reducing steamline pressure drop and allowing higher drain line pressure drop and thus, higher drain flow. Greater sensitivity to drain line resistance at high pressure rather than low pressure was expected because the drain flow was greater; however, the effect of the resistance was seen to be small.

  - At low pressure, critical flow could occur in the throat of the steam distributor, which was the minimum flow area. Also, momentum in the throat tended to be recovered adjacent to the lowest holes of the distributor (i.e., at the dead end of the pipe), so that the maximum steam

momentum entering the CMT was from those holes, and this maximum was limited to the critical velocity. In the CMT tests, the choking in the inlet pipe to the steam distributor imposed a limit on steam momentum at 25 psia. As the pressure increased, the flow was no longer critical, such that the steam momentum was not limited and the resulting mixing depth reached a maximum somewhere between 25 and 60 psia and dropped off with higher or lower pressures. At 700 and 1100 psia, however, the variation of mixing depth with drain resistance was approximately in the correct direction.

The above trend with the steam momentum indicated in the top graph of Figure 4.3-1 is that mixing depth increased as pressure dropped from 1100 psia, with one test at 60 psia showing the maximum depth. Again, since the flow was choked at 25 psia, the steam momentum flux was limited, such that the mixing depth was less than at 60 psia. The scatter between different drain resistances at constant pressure was greater than expected at low pressure, especially at 150 psia, and lower than expected at high pressure.

- The mixing and condensation ended suddenly while the bulk of the mixing region was well subcooled.

The second graph in Figure 4.3-1 shows the subcooling of the mixing region, relative to the saturation temperature at nominal reservoir pressure at the start of free drain. As is discussed in the next paragraph, this value was estimated from axial and temporal plots of fluid temperature, from the approximate average temperature in the mixed region just before the top temperature rises to saturation, i.e., just before the water level starts its orderly drop. The estimate was especially rough for very low mixing depth, because the separation between the mixing region and the surface was difficult to define.

For a case with substantial mixing, Figure 4.3-2 shows a more detailed axial temperature distribution plot than those shown in Section 3.3. This is for test C032310, at 25 psia nominal pressure and 17 gpm drain resistance. The temperature plotted at 120 in. is actually in the steam line; the top inside of the CMT is 114 in. from the bottom, and the highest fluid thermocouple is at 112 in. A mixing region extending to 101 in. or below is indicated. (There is a thermocouple at 99 in. level, but it was not plotted on this type of graph because it was occasionally unreliable.) Mixed heating in this region lasted until 80 seconds. At 85 seconds, the temperatures at 111 in. and 112 in. separated; a hotter surface layer formed, and heating of the larger mixed region slowed. At 90 seconds, the surface layer heated by another 30°F to 40°F. At 95 seconds, the surface was saturated, a steam region and water level formed at the top of the CMT, draining started, and the entire region moved down about 2 in. A rough average temperature of 147°F was chosen for the mixed temperature at 85 seconds, when the upper temperature has started its rise.

Figure 4.3-3 shows fluid thermocouple temperatures versus time for the same time period, along with CMT saturation temperature and calculated water level. As in the temperature distribution plot, a clear boundary between mixed and unmixed region forms in the first 20 seconds between the 99 in. and 95 in. elevations, with temperatures in the lower part of this region following but lagging behind those in the top. At 82 seconds, the top temperatures at 112 in. and 111 in. started

to rise much faster. At 87 seconds, the calculated water level, which had been oscillating above 111 in. (probably reflecting a void content in the mixed region) started its steady descent. At the same time, the steam flow started to drop. Steam flow was reflected in the depression of the CMT pressure below the reservoir pressure, and thus by the reduction in CMT saturation temperature. At 87 seconds, the temperature down to 111 in. was about 180°F, still 20°F subcooled. The temperature at 10 in. and below slowed its heating at 147°F or below, and the CMT saturation temperature is 203°F, thus, subcooling is 56°F. For this test, the characteristic time for start of drain was 91 seconds, corresponding to the maximum drain flow, which is reflected in the maximum on CMT saturation temperature. This illustration summarizes the method of selecting the "final" mixed temperature and subcooling.

Given an estimate of this terminal subcooling and the volume of the mixing region, the mixing delay might be estimated from the time taken to heat the mixing region up to this condition. In that regard, the fraction of the initial subcooling remaining at the end of the mixing period was a more pertinent parameter. As shown in the top of Figure 4.3-4 the wide scatter in subcooling at 110C psia becomes a small fraction of the total temperature span. The greater relative subcooling at 25 psia shortened the drain delay relative to the other pressures.

- The delay to free drain was a maximum for the 60-psia tests, and was fairly independent of drain line resistance except for one test at 150 psia, 11 gpm.

  The lower graph of Figure 4.3-4 shows the delay, measured from the time the drain valve began to open.

No reason has yet been found for the deviation of the 150-psia, 11-gpm test results from the well-grouped results of the other tests. With this exception, the trends reflect the postulated causes and conclusions discussed in the previous paragraphs.

- The delay at 25 psia is short because of the combination of choking in the steam distributor, which prevents very deep mixing, low initial subcooling, and relatively high subcooling at the end of mixing.

- The delay is long for the 60-psia tests because of deep mixing, caused by high steam momentum per unit drain flow at low pressure without choking, combined with relatively low final subcooling.

- The delay decreases as pressure goes above 60 psia because mixing depth decreases due to the reduction in steam momentum per unit drain flow. This effect overrides the opposing effect of increasing initial subcooling.

- Despite the postulated dependence of mixing depth and drain delay on the relationship between steam line and drain line head losses, the expected increase of sensitivity to drain line resistance with increasing pressure does not appear in the data.

Figures 4.3-1 through 4.3-4 are not included in the non-proprietary version of this document.

4.4 Liquid Region Wall Heat Transfer

As the CMT recirculated, hot liquid flowed to the top of the CMT, creating a hot liquid layer. Since the flows were small, there was very little mixing of this layer with the colder water in the CMT, and a thermally stratified hot liquid layer was formed. As the CMT drained, the hot liquid layer transferred heat to the cold CMT wall.

The CMT data from the 300-series tests were analyzed to obtain the local convective heat transfer coefficient between the hot liquid layer and the cold CMT walls. The locally calculated heat flux was used as a guide when the hot liquid layer passed the wall thermocouple positions. Figure 4.4-1 shows the locally calculated wall heat flux at the 86.1" elevation along the CMT wall. The sharp spike in the heat flux occurred when the top of the liquid layer passed the instrumented position and the steam began to condense on the CMT walls. The plateau of the heat flux plot before the spike is the convective heat transfer from the hot water layer to the cold CMT walls. The convective portion of the heat flux is circled on the figures.

The approach used to analyze the test data was to magnify the heat flux plot for improved resolution and plot the heat flux and level measurement from the pressure cells on the same plot as shown in Figure 4.4-2. The time when the heat flux increased from zero to the plateau value and the time when the heat flux increased to the value at the spike were read from the plot and used to intersect with the level graph on the same plot, as shown in Figure 4.4-2. The intersections on the time scale indicate the time it took for the hot liquid layer to pass the fixed wall thermocouple position. The intersection of the time scale indicates the time period it took for the hot liquid layer to pass the fixed wall thermocouple position. The intersection of the time periods with the level plot indicates the thickness of the hot liquid layer as it passes the instrumented position. Figure 4.4-2 indicates that the hot liquid layer is approximately 14-in. thick. The local wall temperature calculated from the CONTRA program as well as the local fluid temperature at the same axial position are shown in Figure 4.4-3. The figure indicates that as the hot liquid passes by the wall location, the fluid thermocouple and the wall temperature heat up as heat is transferred to the wall from the fluid.

The local heat transfer coefficient and Nusselt number were calculated directly from the data by performing a time average of the measured quantities. The heat flux plots were magnified to obtain improved resolution and were averaged over the time period of interest. The thickness of the hot layer was obtained directly from the combined heat flux and level plot as indicated above. A straight line was drawn through an expanded plot of the wall temperature and fluid temperature data, and the average temperature difference was obtained from the plots. The average local heat transfer coefficient was obtained by:

$$h = \frac{q_w''}{(T_w - T_b)} \qquad (4.4\text{-}1)$$

where:

q_w'' = averaged wall heat flux
T_w = wall temperature
T_b = bulk fluid temperature

The average Nusselt number was calculated as:

$$N_{exp} = \frac{q_w'' \, L}{(T_w - T_b)k_f} \tag{4.4-2}$$

where:

q_w'' = wall heat flux
L = mixing or hot liquid layer thickness
k_f = fluid thermal conductivity
T_w = wall temperature
T_b = bulk fluid temperature

The average Nusselt number for heat transfer from the hot liquid layer to the CMT walls was calculated at the different instrumented elevations for the 300-series tests.

Calculations were also performed to determine if the process was a natural convection or a forced convection. The bulk Reynolds number was calculated and found to be very small since the CMT drains so slowly, such that the Dittus-Boelter correlation[17] was not applicable. A forced convection correlation for flow along a flat plate from Kreith and Bohn[18] was also examined and found to give too low a Reynolds number. Therefore, the ratio of Gr/Re^2 indicates that the flow is natural-circulation-driven and an appropriate correlation is the McAdams natural convection correlation[19] given as:

$$\bar{h} = (0.13)\frac{k_f}{L}\left[(G_R * P_{r_f})\right]^{1/3} \tag{4.4-3}$$

where G_R is the Grashoff number based on the mixing length, and P_{r_f} is the fluid Prandtl number. The Grashoff number is given as:

$$G_R = g\frac{\beta(T_w - T_b)L^3\rho_f^2}{\mu_f^2} \qquad (4.4\text{-}4)$$

where:

- β = thermal expansion coefficient of the fluid
- ρ_f = fluid density
- R = fluid thermal conductivity
- μ_f = fluid viscosity
- T_w = wall temperature
- T_b = bulk fluid temperature
- L = mixing thickness of the hot liquid layer
- g = acceleration due to gravity

The McAdams heat transfer coefficients were calculated for the test conditions and the measured mixing layer and converted into Nusselt numbers. Figure 4.4-4 shows the calculated Nusselt numbers from the tests versus the calculated Nusselt numbers using the McAdams correlation. The agreement between the calculated and measured Nusselt numbers is reasonably good and indicates that the McAdams correlation will predict the heat transfer to the CMT walls with sufficient accuracy.

Figures 4.4-1 through 4.4-4 are not included in the non-proprietary version of this document.

4.5 Comparison of 500-Series Natural Circulation Tests to Calculation Model

The natural circulation model described in Section 2.9 was used to predict the 500-series natural circulation tests. The model was used to analyze the CMT test facility from an initial condition where the CMT is filled with cold water, to the time where the cold water has been completely replaced by hot water.

Two tests, C064506 and C072509, were analyzed with the natural circulation model. These tests were chosen because the end of the recirculation phase occurs when the CMT is completely filled with hot water. These tests were run at 1100 psia and 1850 psia, respectively, with cold water at 78°F in the CMT and saturated liquid in the S/WR. At the start of the run, valve V3 was opened to the "full open" position, and natural circulation flow was established. As the cold water is discharged from the CMT, it is replaced by a hot water layer, which increased in thickness. The model was used to predict the CMT discharge flow rate and the thickness of the hot water layer over the initial phase of recirculation. The predictions were compared to the test data to determine the validity of the tests.

The initial conditions for both tests, which were used in the natural circulation model, are summarized in Table 4.5-1. The comparison of the hot liquid layer thickness and the CMT discharge flow rate for both the model and test C064506 are shown in Figures 4.5-1 and 4.5-2. This comparison indicates that the model predictions match the test results.

The comparison of the hot liquid layer thickness and the CMT discharge flow rate for the model and test C072509 are shown in Figures 4.5-3 and 4.5-4. Once again, the hot layer thickness is predicted by the model, and the flow is slightly over-predicted.

The model was applied to the other seven recirculation tests; good agreement was obtained for all but tests C059502 and C061504. In both tests, the calculated flow was much higher than the measured flow. This is thought to be due to a partially opened drain line valve, V3.

The following conclusions can be drawn based on these comparisons:

- The natural circulation model, as developed in the CMT Test Scaling Report,[2] accurately predicts the test results at both high and low system pressure. Thus, the phenomena addressed in Reference 2 are accurately modeled in the natural circulation tests.

- The assumptions used in the development of the natural circulation model are reflected in the tests. Specifically, the tests, while run at saturated conditions, are predicted by single-phase recirculation, and no two-phase effects are observed.

- The data generated in these tests are adequate for use in the validation of computer codes modeling single-phase, buoyancy driven, and natural circulation flow.

TABLE 4.5-1 KEY PARAMETERS FOR NATURAL CIRCULATION ANALYSIS		
Parameter	**Test 506**	**Test 509**
CMT Inlet Pressure	1080 psig	1815 psig
CMT Initial Temperature	78°F	78°F
S/WR Initial Temperature	556°F	623°F
Drain Line Loss Coefficient	56.71	56.71
Steam Line 2 Loss Coefficient	21.4	21.4
Pipe Diameter	1.356 in.	1.356 i
Valve V3 % Open	100	100

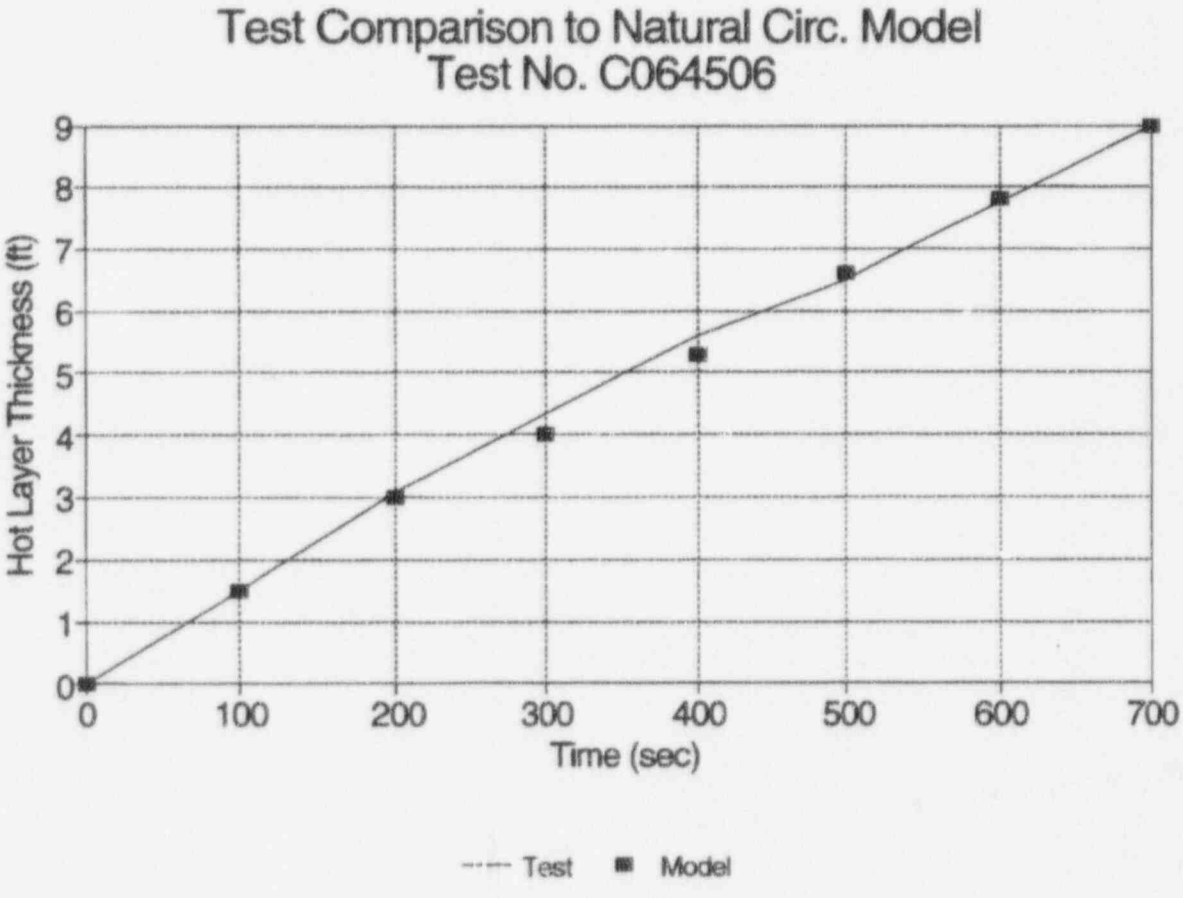

Figure 4.5-1 Hot Liquid Layer Thickness Comparison, Test C064506

Figures 4.5-2 through 4.5-4 are not included in the non-proprietary version of this document.

4.6 Addressing the Core Make-up Tank Test PIRT

As part of the core makeup tank scaling logic, a phenomena identification and ranking table (PIRT) was developed to identify the key thermal-hydraulic phenomena that were needed to validate safety analysis computer models of the CMT. The PIRT is taken from the CMT scaling report and is presented as Table 1.2-1.

The key thermal-hydraulic phenomena are grouped in Table 1.2-1 based on the phase of CMT behavior, either draining or recirculation, during which these phenomena are present. For the CMT draining phenomena, the condensation on the cold walls and the transient conduction in the walls were addressed with the 100-series tests. Interfacial condensation, dynamic effects of steam injection, thermal stratification, and mixing effects were simulated in the 300-series tests. The steam injection and mixing effects were also simulated in the 500-series tests. The phenomena identified in the PIRT table for CMT recirculation were investigated as part of the 500-series tests. Flashing effects of the hot CMT liquid layer were examined in both the 400- and 500-series tests. In the 400-series tests, the hot liquid layer was developed from steam condensation and mixing. In the 500-series tests, the hot liquid layer was developed from the recirculation behavior. The CMT convective wall heat transfer below the hot liquid/steam interface was calculated from the 300-series tests.

All the phenomena that were identified in the CMT scaling analysis PIRT have been examined experimentally, and the resulting data have been analyzed and compared to correlations where applicable. Therefore, the requirements identified in the CMT scaling report have been achieved.

5.0 CONCLUSIONS

The specific objectives of the CMT test program were achieved. Experimental data were obtained on the thermal-hydraulic behavior of the CMT during the recirculation phase of operation as well as the gravity-drain period of operation. Specifically, data were obtained to verify the wall condensation correlations, the convective heat transfer from the hot liquid layer to the CMT walls, and the steam condensation and mixing effects within the CMT liquid. All these phenomena are required to be calculated in the AP600 safety analysis computer programs.

The specific thermal-hydraulic phenomena important for understanding the CMT behavior were identified in the CMT Scaling Report.[2] The CMT test was designed to obtain the needed data to assess those thermal-hydraulic phenomena. The analysis of the data provides the understanding of the thermal-hydraulic phenomena.

The analysis of the test data supports the application of the Nusselt film condensation model for the condensation on the CMT walls. Convective heat transfer from the heated CMT liquid layer to the CMT walls can be modeled using the McAdams natural convection heat transfer correlation. The analysis of the data supports the hypothesis that it is the momentum of the steam into the CMT that determines the amount of mixing at the top of the CMT and hence the delay in the free drain of the CMT liquid.

The recirculation flow behavior of the CMT was found to be very predictable using a mechanical energy balance formulation that included the line resistances and the varying buoyant head difference for the CMT. After the CMT had been in the recirculation phase and as the CMT started to drain, there was no noticeable effect of the steam mixing with and condensing on the hot CMT liquid at the top of the CMT. The condensation on the CMT walls was also reduced due to the heat transfer from the heated liquid layer to the CMT walls. Therefore, the CMT drained freely. Draining was not significantly affected by flashing of hot CMT liquid during depressurization.

The key thermal-hydraulic phenomena, which were identified in the CMT Scaling Report, have been addressed in the analysis of the CMT data, which provide the means to validate the CMT models in the AP600 safety analysis computer codes.

6.0 REFERENCES

1. Westinghouse Electric Corporation, *AP600 Standard Safety Analysis Report (SSAR)*, June 1992.

2. Aumiller, D. and L. E. Hochreiter, *Scaling Logic for the Core Makeup Tank Test*, WCAP-13963, January 1994.

3. Leonelli, K., *Core Makeup Tank Test Data Report*, WCAP-14217 (Proprietary), November 1994.

4. Taylor, R. E., J. Ferrier, and H. Groot, "Thermophysical Properties of Sch 160 SA-106 Seamless C. S. Pipe," TPRL 1325, Thermophysical Properties Research Laboratory, School of Mechanical Engineering, Purdue University, West Lafayette, Indiana.

5. Beck, J. V., *Users Manual for CONTA - Program for Calculating Surface Heat Fluxes from Transient Temperatures Inside Solids*, SAND-83-7134, 1983. Also see Beck, J. V., B. Blackwell, and C. R. St. Clair Jr., *Inverse Heat Conduction - Ill Posed Problems*, Wiley-Interscience Publications, New York, 1985.

6. Nusselt, W., "Die Oberflachenkondensation des Wannerdampfes," Vol. 60, Zeitschr. Ver. Deutsch. Ing., 1916, pp. 541-564. Also see Collier, J. G., *Convective Boiling and Condensation*, McGraw-Hill, Inc., 1972, pp. 314-319.

7. Rohsenow, W. M., "Heat Transfer and Temperature Distribution in Laminar Film Condensation," Trans. ASME, 78, 1956, pp. 1645-1648.

8. Drew, T. B. See McAdams, *Heat Transmission*, 3rd edition, McGraw Hill, Inc., New York, 1954.

9. Minkowicz, W. J. and E. M. Sparrow, "Condensation Heat Transfer in the Presence of Non-Condensables, Interfacial Resistance, Superheating, Variable Properties and Diffusion," *International Journal of Heat Mass Transfer*, 9, 1966, pp. 1125-1144.

10. Conte, S. D. and C. de Boor, *Elementary Numerical Analysis*, Second Edition, McGraw-Hill, Inc. New York, 1965.

11. Bennett, C. O. and J. E. Meyer, *Momentum, Heat and Mass Transfer*, McGraw-Hill Inc., New York, 1960.

12. Colburn, A. P., *Note on Calculation of Condensation When a Portion of the Condensate Layer is in Turbulent Motion*, AICHE Transaction, Vol. 30, 1933, pp. 187-193.

13. Seban, R. A., "Remarks on Film Condensation with Turbulent Flow," Trans ASME, Vol. 76, 1954, p. 299.

14. Rohsenow, W. M., J. H. Weber, and A. T. Ling, "Effects of Vapor Velocity on Laminar and Turbulent Flow Condensation," Trans ASME, Vol. 78, 1956, pp. 1637-1643.

15. Sparrow, E. M., W. J. Minkowycz, and M. Saddy, "Forced Convection Condensation in the Presence of Non-condensables and Interfacial Resistance," *International Journal of Heat Mass Transfer*, Vol. 10, 1967, pp. 1829-1845.

16. Collier, J. G., *Convective Boiling and Condensation*, First Edition, McGraw-Hill Inc., New York, 1972, pp. 315.

17. Dittus, F. W. and L. M. K. Boelter, "Heat Transmission in Automobile Radiators of the Tubler Type," University of California Publications in Engineering, Vol. 2, No. 13, 1930, pp. 443-461.

18. Kreith, F. and M. S. Bohn, *Principles of Heat Transfer*, Fourth Edition, Harper & Row Publishers, 1986, p. 217.

19. McAdams, W. H., *Heat Transmission*, McGraw-Hill, Inc., New York, 1954.

APPENDIX A
CALIBRATION FUNCTIONS USED IN ANALYSIS

CALIBRATION FUNCTIONS USED IN ANALYSIS

The top graph of Figure A-1 shows the ratio of actual flow to indicated flow for the CMT discharge line flowmeters FM1 and FM6. The values shown were used, with linear interpolation, to multiply flow recorded to obtain actual flow used in analyses.

The bottom graph of Figure A-1 shows measured head loss factors for differential pressure cells, used to calculate steamline 1 flow. The notation with FM4 and without FM4 refers to the fact that the line resistance is different depending on whether a pipe-size spool piece or the larger-diameter flowmeter section is present in the line.

Figure A-2 shows the thermal properties of the CMT vessel used in calculation of wall surface heat flux and surface temperature.

Figure A-1 is not included in the non-proprietary version of this document.

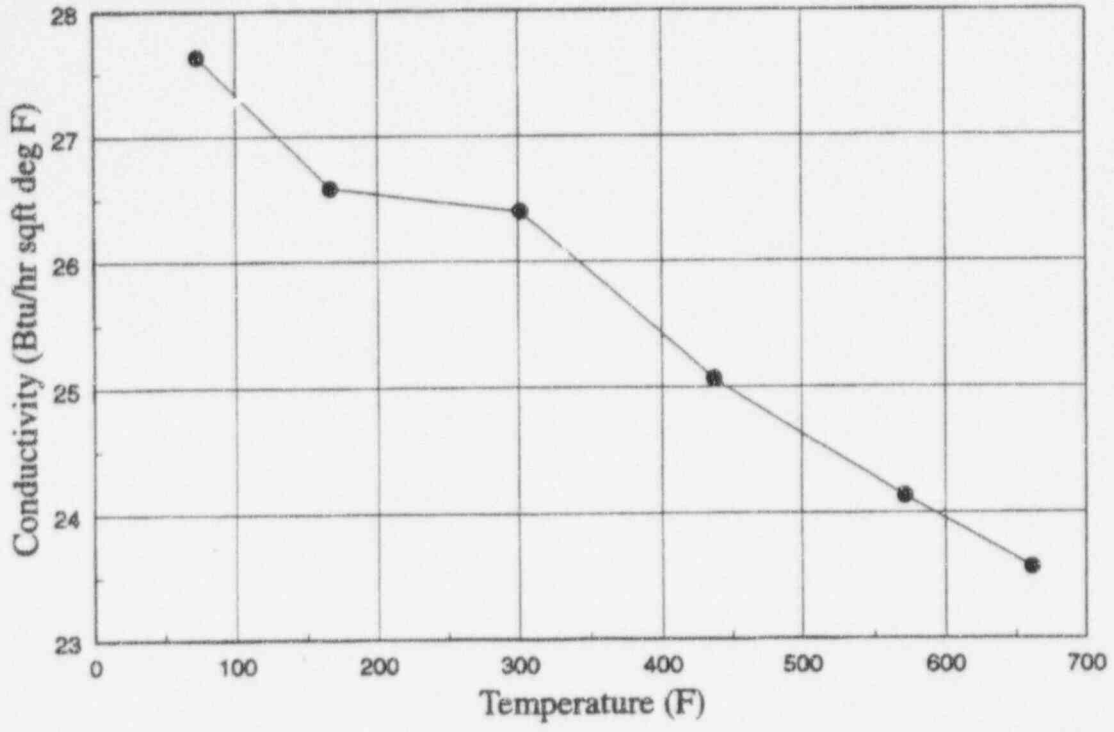

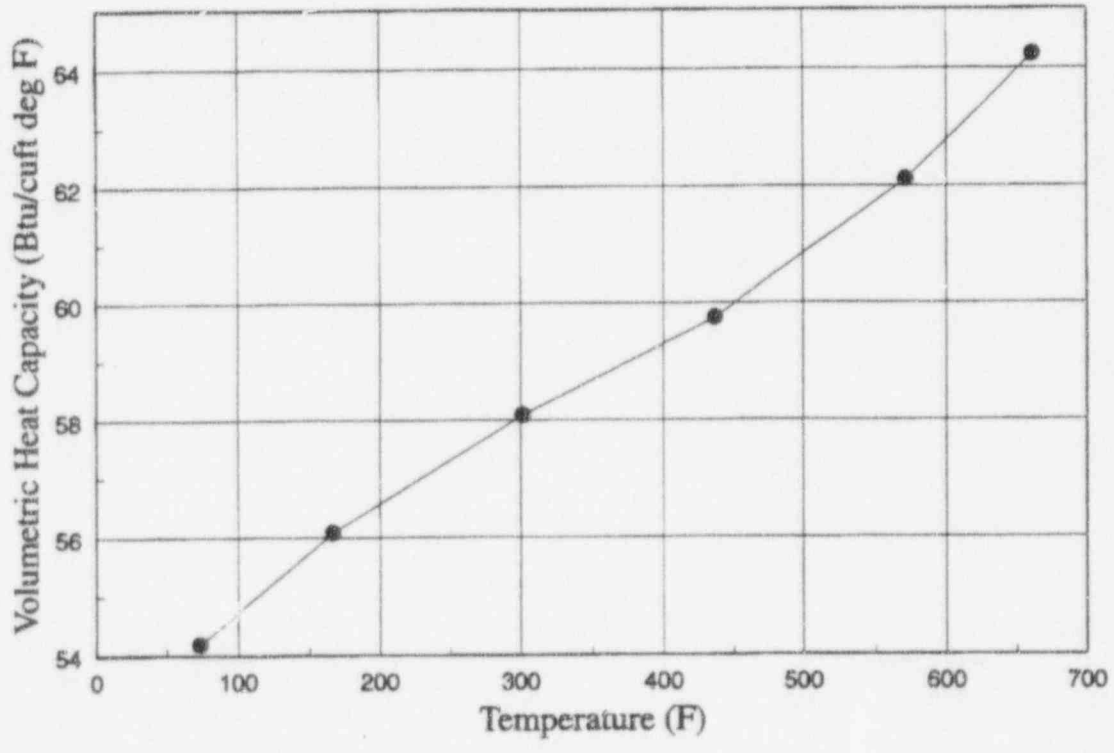

Figure A-2 Thermal Conductivity and Volumetric Heat Capacity of CMT Vessel Material Used in CMT Test Analysis

APPENDIX B
STEAM LINE FLOW CALCULATIONS

STEAM LINE FLOW CALCULATIONS

Conversion/Correction of Measured Pressures: P_{T1} thru P_{T5}

$$P_{REF} = P_{PAT} \text{ or } 14.3 \text{ psia}$$

$$\rho_{LEG} = \rho\left(\left[\frac{P_{T1} + P_{T5}}{2} + P_{REF}\right], T_{AMB}\right)$$ = density in reference legs of PT taps , lb_m/ft^3

(function employs steam table library: VCL)

$$PC_{Ti} = P_{Ti} - \frac{h_{LEGi} * \rho_{LEG}}{144} + P_{REF}$$ = corrected pressure for PTi , psia

DP_{Loss} Normalization (optional)

Time range when DP_{Loss} should have zero value (i.e. zero flow period):
from time = first time step (start of data)
to last time step with valve 3 closed, and valve 1, 1A or 2 is open as appropriate

Averaging not done when first time step has valve 3 open and/or both valves 1 & 2 closed

Determine average DP_{Loss} over time range. Use average as an offset for DP_{Loss} such that:
"new DP_{Loss}" = "DP_{Loss}" - "average DP_{Loss}"

Reservoir and Steam Line Calculations

Assumption: constant enthalpy from reservoir exit to CMT entrance
Assumption: reservoir provides dry steam to steam line 1 and liquid to steam line 2

$$T_{SAT1} = T_{saturation}(PC_{T1})$$ (function employs steam table library)

$$h_{AV} = f\left(PC_{T1}, \text{ greater of } T_{SAT1} \text{ \& } T_{SWST}\right)$$ = reservoir top exit enthalpy , btu/lb_m

(function employs steam table library)

$$h_{2AV} = f\left(PC_{T1}, \text{ lesser of } (T_{SAT1} - 0.01) \text{ \& } T_{SWST}\right)$$ = reservoir lower exit enthalpy , btu/lb_m (function employs steam table library)

Flow Calculations require the availability of valve V_1 and/or V_2

Steam Lines 1 & 2

Process steam line 1 upstream: calculation valid when V_1 open

$$DPC_{US1} = DP_{DT8} + \frac{d_{elev8}\ \rho_{LEG}}{144}$$ = upstream $\Delta P_{steam\ line\ 1}$, psi

$$K = K_{LOSS-US1}$$

$$\nu = f\left(PC_{T2} - \frac{DPC_{US1}}{2},\ h_{AV}\right)$$ (functions employ steam table library: consider mixture)

$$\rho = f\left(PC_{T2} - \frac{DPC_{US1}}{2},\ h_{AV}\right)$$ (functions employ steam table library: consider mixture)

$$\rho_{UP} = f\left(PC_{T2},\ h_{AV}\right)$$ = density at upstream end of span

$$\rho_{DOWN} = f\left(PC_{T2} - DPC_{US1},\ h_{AV}\right)$$ = density at downstream end

$$DP_{LOSS-US1} = DPC_{US1} - \frac{d_{elev8}\ \rho}{144}$$ = upstream $\Delta P_{loss\ steam\ line\ 1}$, psi

optionally normalize $DP_{LOSS-US1}$ - consider only valid data

$$F_{US1} = fl_{area}\sqrt{\frac{DP_{LOSS-US1}\ 2\ g_c\ 144}{\frac{K}{\rho} + \frac{1}{\rho_{DOWN}} - \frac{1}{\rho_{UP}}}}$$ = upstream $flow_{steam\ line\ 1}$, psi

$$R_{US1} = \frac{D}{\nu} \frac{F_{US1}}{fl_{area}}$$ = upstream Reynolds $\#_{\text{steam line 1}}$, psi

Process steam line 1 downstream: calculation valid when V_1 open & V_2 closed

$$DPC_{DS1} = DP_{DT11} + \frac{d_{elev11}\ \rho_{LEG}}{144}$$ = downstream $\Delta P_{\text{steam line 1}}$, psi

$$K = K_{LOSS-DS1}$$

$$\nu = f\left(PC_{T5} + \frac{DPC_{DS1}}{2},\ h_{AV}\right)$$ (function employs steam table library: consider mixture)

$$\rho = f\left(PC_{T5} + \frac{DPC_{DS1}}{2},\ h_{AV}\right)$$ (functions employ steam table library: consider mixture)

$$\rho_{UP} = f\left(PC_{T5} + DPC_{DS1},\ h_{AV}\right)$$

$$\rho_{DOWN} = f\left(PC_{T5},\ h_{AV}\right)$$

$$DP_{LOSS-DS1} = DPC_{DS1} - \frac{d_{elev11}\ \rho}{144}$$ = downstream $\Delta P_{\text{loss steam line 1}}$, psi

optionally normalize $DP_{LOSS-DS1}$ - consider only valid data

$$F_{DS1} = fl_{area} \sqrt{-\frac{DP_{LOSS-DS1}\ 2\ g_c\ 144}{\frac{K}{\rho} + \frac{1}{\rho_{DOWN}} - \frac{1}{\rho_{UP}}}}$$ = downstream $\text{flow}_{\text{steam line 1}}$, psi

$$R_{DS1} = \frac{D}{\nu} \frac{F_{DS1}}{fl_{area}}$$ = downstream Reynolds $\#_{\text{steam line 1}}$, psi

Process steam line 1 vortex flowmeter, FM4: calculation valid when V_1 open

$$\rho = f\left(PC_{T7}, \text{ greater of } T_{SAT1} \text{ and } T(TC72A)\right)$$ (density at flowmeter)

$$F_{FM4} = VF_{FM4} * \rho$$

Process steam line 2 upstream: calculation valid when V_2 open

$$DPC_{US2} = DP_{DT9} + \frac{d_{elev9}\ \rho_{LEG}}{144}$$ = upstream $\Delta P_{\text{steam line 2}}$, psi

$$K = K_{LOSS-US2}$$

$$\nu = f\left(PC_{T1} - \frac{DPC_{US2}}{2}, h_{2AV}\right)$$ (functions employ steam table library: consider mixture)

$$\rho = f\left(PC_{T1} - \frac{DPC_{US2}}{2}, h_{2AV}\right)$$ (functions employ steam table library: consider mixture)

$$\rho_{up} = f\left(PC_{TI}, h_{2AV}\right)$$

$$\rho_{DOWN} = f\left(PC_{TI} - DPC_{US2}, h_{2AV}\right)$$

$$DP_{LOSS-US2} = DPC_{US2} - \frac{d_{elev9}\ \rho}{144}$$ = upstream $\Delta P_{\text{loss steam line 2}}$, psi

optionally normalize $DP_{LOSS-US2}$ - consider only valid data

$$F_{US2} = fl_{area} \sqrt{\frac{DP_{LOSS-US2}\ 2\ g_c\ 144}{\frac{K}{\rho} + \frac{1}{\rho_{DOWN}} - \frac{1}{\rho_{UP}}}}$$ = upstream $flow_{steam\ line\ 2}$, psi

$$R_{US2} = \frac{D}{v}\ \frac{F_{US2}}{fl_{area}}$$ = upstream Reynolds $\#_{steam\ line\ 2}$, psi

Process steam line 2 downstream: calculation valid when V_2 open & V_1 closed

$$DPC_{DS2} = DP_{DT12} + \frac{d_{elev12}\ \rho_{LEG}}{144}$$ = downstream $\Delta P_{steam\ line\ 2}$, psi

$$K = K_{LOSS-DS2}$$

$$v = f\left(PC_{T5} + \frac{DPC_{DS2}}{2},\ h_{2AV}\right)$$ (functions employ steam table library: consider mixture)

$$\rho = f\left(PC_{T5} + \frac{DPC_{DS2}}{2},\ h_{2AV}\right)$$ (functions employ steam table library: consider mixture)

$$\rho_{UP} = f\left(PC_{T5} + DPC_{DS2},\ h_{2AV}\right)$$

$$\rho_{DOWN} = f\left(PC_{T5},\ h_{2AV}\right)$$

$$DP_{LOSS-DS2} = DPC_{DS2} - \frac{d_{elev12}\ \rho}{144}$$ = downstream $\Delta P_{loss\ steam\ line\ 2}$, psi

optionally normalize $DP_{LOSS-DS2}$ - consider only valid data

$$F_{DS2} = fl_{area} \sqrt{\frac{DP_{LOSS-DS2}\ 2\ g_c\ 144}{\frac{K}{\rho} + \frac{1}{\rho_{DOWN}} - \frac{1}{\rho_{UP}}}}$$ = downstream $flow_{steam\ line\ 2}$, psi

$$R_{DS2} = \frac{D}{\nu}\ \frac{F_{DS2}}{fl_{area}}$$ = downstream Reynolds $\#_{steam\ line\ 2}$, psi

CMT inlet and steam distributor: calculation valid when:

V_1 open and V_2 closed, then $h_{DIF} = h_{AV}$; or

V_1 closed and V_2 open, then $h_{DIF} = h_{2AV}$

V_3 closed and 100 series test, then

$$h_{DIF} = h_v \left(PC_{T5} + \frac{DPC_S}{2},\ T_{sat} \right)$$

V_3 closed and 300 series test, then

$$h_{DIF} = h \left(PC_{T5} + \frac{DPC_S}{2},\ \frac{T_{TC76} + T_{TC62}}{2} \right)$$

Note: V_1 or V_2 is open when V_3 is open
V_1 and V_2 are not concurrently open

$$DPC_S = DP_{DT13} + \frac{d_{elev13}\ \rho_{LEG}}{144}$$ = diffuser ΔP, psi

$$K = K_{LOSS-S}$$ = Total loss factor derived from liquid flow tests

$$\nu = f\left(PC_{T5} + \frac{DPC_S}{2},\ h_{DIF}\right)$$

$$\rho = f\left(PC_{T5} + \frac{DPC_S}{2},\ h_{DIF}\right)$$

$$\rho_{UP} = f\left(PC_{T4},\ h_{DIF}\right)$$

$$DP_{LOSS-S} = DPC_S - \frac{d_{elev13}\rho}{144}$$

optionally normalize DP_{LOSS-S} - consider only valid data

$$F_S = fl_{area}\sqrt{\frac{DP_{LOSS-S}\ 2g_c\ 144}{\frac{K+1}{\rho} - \frac{1}{\rho_{UP}}}}$$ = steamlines flow into CMT

$$R_S = \frac{D}{\nu}\frac{F_S}{fl_{area}}$$

Determine Best-Estimate, Maximum, and Minimum flows for steam line 1 & 2

$F_{BEST-SL1}$ = F_{FM4} if F_{FM4} is valid

or

$F_{BEST-SL1}$ = F_S if F_S is valid and V_1 open and V_2 closed

or

$F_{BEST-SL1}$ = F_{US1} if F_{US1} is valid

or

$F_{BEST-SL1}$ = F_{DS1} if F_{DS1} is valid

or

$F_{BEST-SL1}$ = 0

$F_{BEST-SL2}$ = F_s if F_S is valid and V_2 open and V_2 closed

or

$F_{BEST-SL2}$ = 0

CMT inlet

$F_{CMT} = F_{BEST-SL1} + F_{BEST-SL2}$ = CMT inlet flow , lb_m/sec

$M_{CMT} = \int_{time} F_{CMT}\, dt$ = integrated CMT inlet flow , lb_m

$h_{CMT} = h_{AV}$ if V_2 not open
= CMT inlet enthalpy , btu/lb_m

or

$h_{CMT} = h_{2av}$ if V_2 open

$\rho_{CMT} = f(PC_{T5} , h_{CMT})$ = CMT inlet density , lb_m/ft^3
function employs steam table library: consider mixture)

$V_{CMT} = \dfrac{F_{CMT}}{\rho_{CMT}\, fl_{area}}$ = CMT inlet velocity , ft/sec

$MOMH_{CMT} = \dfrac{\rho_{CMT}\, V_{CMT}^2\, 12}{4\, g_c\, 62.428}$ = CMT inlet momentum , inches of cold water,

for pipe area and CMT pressure

$T_{SAT-CMT} = T_{saturation}(PC_{T5})$ = T_{sat} @ CMT inlet pressure , °F (function employs steam table library: TSL)

CMT and Discharge Line

T_{DIS} = fluid temperature in discharge line (or in CMT bottom as backup)

following calculated only when $PC_{T5} \geq P_{saturation} (T_{DIS})$ (function employs steam table library)

$\rho = f (PC_{T5} , T_{DIS})$ (function employs steam table library)

VF_{DIS} = normalized VF_{FM6} if FM6 present

VF_{DIS} = VF_{FM1} if FM6 not present

$F_{DIS} = VF_{DIS} * \text{multiplier } (VF_{DIS}) * \rho$ = corrected discharge line flow to steam/water reservoir, lb_m/sec

$M_{CMT-OUT} = \int_{time} F_{DIS} dt$ = integrated CMT outlet flow, lb_m

General Nomenclature

D	=	pipe inside diameter
DP	=	pressure difference
DP_{DTi}	=	pressure difference measured by differential pressure cell PDTi
DP_{LOSS}	=	pressure difference after removal of calculated elevation heads
d_{elevi}	=	elevation difference between taps of differential pressure cell PDTi
F	=	mass flow rate
fl_{area}	=	pipe flow area
h	=	specific enthalpy
h_{LEGi}	=	height of reference leg for pressure tap PTi
$K_{LOSS-xi}$	=	head loss factor for location x in steam line i measured with liquid, a function of Reynolds number
P	=	pressure
P_{ATM}	=	measured atmospheric pressure
P_{TI}	=	pressure measured for pressure tap PTi
T	=	temperature
T_{AMB}	=	measured ambient temperature
T_{SWST}	=	corrected temperature at top of steam/water reservoir
V_i	=	position of valve Vi, from test operator's notes, used with a five-second margin
VF	=	measured volumetric flow rate
ρ	=	density
υ	=	viscosity

APPENDIX C
EFFECTS OF FLOW MEASUREMENT UNCERTAINTY ON MASS BALANCE ERROR

EFFECTS OF FLOW MEASUREMENT UNCERTAINTY ON MASS BALANCE ERROR

1.0 Introduction

One method used to evaluate acceptability of the AP600 core makeup tank (CMT) matrix tests was the completion of simplified mass balance calculations on the CMT. The drain flow or water out of the CMT used in these mass balance calculations is typically based on a 1-inch turbine meter installed in the CMT discharge line. A redundant drain flow measurement is provided, for selected low-pressure tests, by a magnetic flow meter also installed in the discharge line.

The purpose of this evaluation is to consider the effects of flow meter accuracy on mass balance error. For the purposes of this evaluation, only the turbine meter, which was utilized for all matrix tests, will be considered. The magnetic flowmeter, installed for selected low-pressure tests, provided increased accuracy at lower flowrates but is not considered in this evaluation since it was not installed for all matrix tests; however, the rationale discussed herein may be applied to the magnetic flowmeter if desired.

2.0 Evaluation of CMT Drain Flow With Respect to Turbine Meter Error Based on Manufacturer's Specifications

The water or condensate drain rate from the CMT through the CMT discharge line to the S/WR is measured using a 1-inch turbine flowmeter. The manufacturer's specifications for this meter are as follows:

Hoffer HO-1X1-4-60-c-1MHT-NPT 1-inch Turbine Flowmeter
Linear Flow Range: 4 to 6 gpm
Repeatable Flow Range: 2 to 75 gpm
Linearity: ± 0.5% of reading over 4 to 60 gpm linear flow range
Repeatability: ± 0.1% of reading over 2 to 75 gpm repeatable flow range

The individual effects of linearity and repeatability may be combined in accordance with:

$$E = \frac{N}{i=1} E_i^{2\ 1/2}$$

where:

E = estimate of total error
E_i = value of ith source of error or component of error
N = number of sources of error

Accordingly, the full scale accuracy of the flowmeter based on the manufacturer's specifications is ±0.382 gpm.

The analog output of the turbine meter is processed by the data acquisition system utilizing an ACRO - Systems 911-916 Analog Input Module. The accuracy of this module is rated by the manufacturer at ± 0.1% of input span + 1 count; based on a ± 20 V.D.C. input span and a 75 gpm F.S. turbine meter range, the accuracy of the analog input module equates to ±0.56 gpm.

The manufacturer specified errors calculated above are considered to be the maximum errors and are assumed to be uniformly distributed over the error interval. Since the variance of a uniformly distributed random variable over the interval $-\alpha < x < \alpha$ is $\alpha^2/3$, the standard deviation of the maximum error may be calculated from the individual instrument errors by:

$$E = \frac{N}{i=1} E_i^2 \, 3^{1/2}$$

where:

- E = standard deviation of the maximum error
- E_i = maximum error of component i
- N = number of individual sources of error

Combining the individual accuracies of the turbine meter and analog input module in accordance with this equation yields an overall accuracy of ±0.39 gpm as reported in WCAP-14217, Appendix D, "AP600 Core Makeup Tank Test Instrument Error Analysis." As stated above however, this accuracy is applicable only over the 4 to 60 gpm linear flow range of the turbine meter; the manufacturer does not specify the accuracy outside this range but does quantify the repeatability of the meter over the entire usable range of 2 to 75 gpm.

In order to evaluate the effects of turbine meter accuracy on mass balance error, 300-Series CMT matrix test C080305 may be considered as an average test with respect to the elapsed time over which the mass balance was calculated; the elapsed time interval for C080305 is reported in WCAP-14217, "Core Makeup Tank Test Data Report," as 970 seconds. An error of ±0.39 gpm applied over this 970 second interval could account for approximately 52.9 lb. of water out of the CMT; the reported mass balance error for this test was -4 lb. which is well within the error which might be expected based on a turbine meter accuracy of ±0.39 gpm.

3.0 Evaluation of CMT Drain Flow With Respect to Turbine Meter Error Determined by Cold Pre-Operational Testing

The accuracy of the CMT discharge line turbine meter was evaluated on a systems-calibration basis in cold pre-op test A-04, as documented in WCAP-14217, "Core Makeup Tank Test Data Report," November 1994. This calibration test, which utilized a weigh tank, indicated that the turbine meter was not accurate below 3.5 gpm. At flow rates greater than or equal to 3.5 gpm, the accuracy of the turbine meter was found to be between ±0.38 gpm and ±0.5 gpm, based on the results of two independent test series. These results, obtained in a systems approach, represent the overall accuracy of the data channel, including effects of the meter and signal processing hardware and are consistent with the accuracy ratings specified by the equipment manufacturers as determined above. Based on a turbine meter accuracy of ±0.38 to ±0.5 gpm and the same 970 second interval (matrix test C080305) considered previously, the turbine meter error could account for up to ±67.32 lb. of water, again broadly encompassing the -4 lb. reported mass balance error.

4.0 Evaluation of CMT Drain Flow With Respect to Turbine Meter Accuracy Based on Corrected Measurements

Using the calibration data obtained in cold pre-op test A-04, as documented in WCAP-14217, "Core Makeup Tank Test Data Report," November 1994, a correction may be developed and applied to the as-recorded flow data. Application of this correction would be expected to provide significantly improved flow measurement accuracy as correcting the data in this fashion has an effect similar to that of using an external linearization conditioner on the turbine meter output.

An approximation of the improved accuracy resulting from correction of the test data was determined by calculating an estimate of the standard deviation with respect to the available repeat calibration data points obtained from the two independent A-04 cold pre-op test series documented in the "Core Makeup Tank Test Data Report," WCAP-14217. Results indicate that the maximum estimate of error gpm evaluated over the average flow range of approximately 3 to 19 gpm is approximately ±0.026. Applying this corrected turbine meter accuracy of ±0.026 gpm to the same 970 second interval (matrix test C080305) considered previously, the corrected turbine meter error could account for approximately ±3.5 lb. of water, which could also be ascribed to the reported -4 lb. mass balance error.

5.0 Conclusions

The mass balance errors reported in the "Core Makeup Tank Test Data Report," WCAP-14217, are typically within the error that might be expected based on a flow measurement accuracy in the range of ±0.39 gpm considered herein. As would be expected, flow measurement error accumulation would account for a larger total mass error for tests evaluated over a longer time interval. While this effect could be used to justify the large mass difference associated with tests such as C052321, it is clear that turbine meter error is not the only factor affecting mass balance error; other tests such as C029306, evaluated over an elapsed time of only approximately 1/10th that of test C052321 has a relatively large mass difference nearly equal to that of test C052321.

The flowrate dependency of the turbine meter K-factor will also have an effect on mass balance error (turbine meter K-factor is the characteristic number of output pulses generated by the turbine meter per engineering unit of flow volume). As evidenced by the cold pre-op test results, the turbine meter is more accurate at higher flow rates. This flowrate dependency of turbine meter accuracy would be expected to influence mass error with respect to tests conducted at different nominal drain rates; in tests conducted at higher nominal drain rates, the flow meter would be expected to be in the more accurate flow range for a greater portion of the test. Alternately, given a test utilizing a lower nominal drain rate, the turbine meter would be operating in a less accurate flow range for a greater portion of the overall test interval, which could result in a higher mass balance error. Correction or linearization of the raw flowmeter data, as discussed in Section 4.0, would compensate for this effect.

Finally, typical reported mass balance errors appear to be consistent with errors that could be expected based on the estimated accuracy of the turbine meter used to measure flow out of the CMT, particularly when considering that error associated with other mass balance inputs, such as steam flow, will also similarly influence the mass error to some extent.

APPENDIX D
CONTRA SENSITIVITY

CONTRA SENSITIVITY

The appendix provides an investigation into the sensitivity of the CONTRA inverse heat conduction analysis to changes in dimensions and inside surface material properties.

The models for the base geometry and the sensitivity geometry are shown in Figure D-1. The changes include:

- Position of inside wall thermocouple relative to the inside surface was moved from 1/2 of the thermocouple diameter to 3/4 of the diameter.

- Wall thickness increased by 0.1 in. Position of second through fourth wall thermocouples relative to the inside moved 0.1 in.

- Conductivity between inside surface and first thermocouple decreased by 20 percent.

The changes were selected to increase the calculated wall heat flux. The magnitudes were selected to be reasonable upper bounds.

The 100-series test C047101 was analyzed with these changes. The local heat flux for the top-cylindrical-wall analysis elevation is shown in Figure D-2. Results for the base geometry, as provided elsewhere in this report, and the sensitivity geometry are shown. The sensitivity is shown in Figure D-3, which provides the ratio of heat fluxes for the sensitivity geometry to the base geometry.

The geometry changes resulted in a relatively constant increase in heat flux of 30 percent for the test case, as shown in Figure D-3.

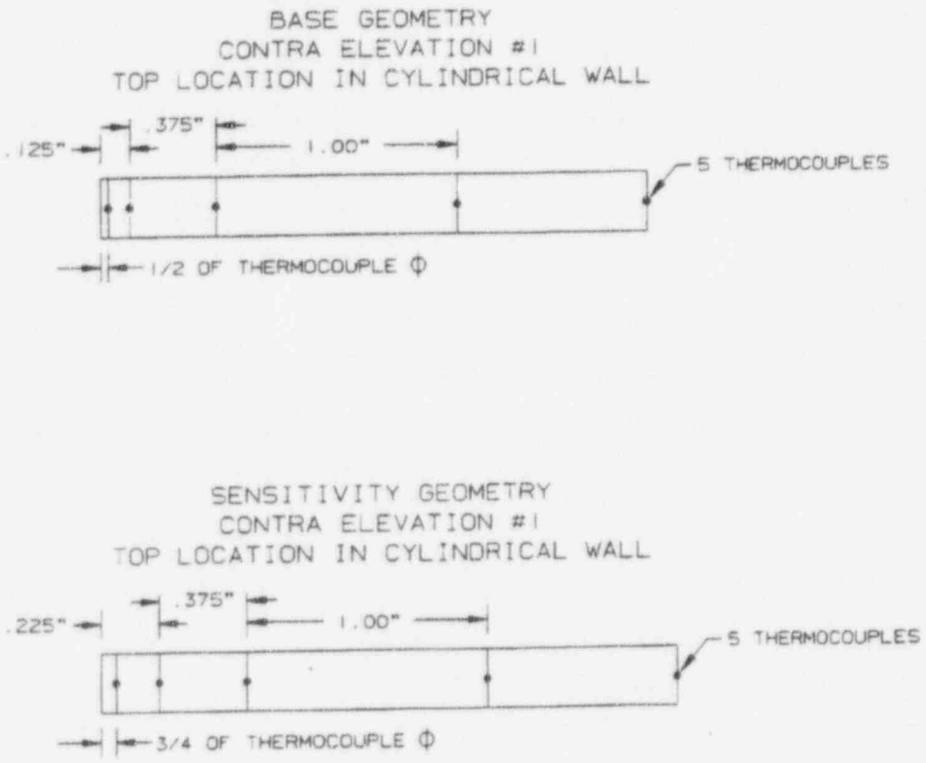

Figure D-1 Local Wall Heat Transfer Modeling for CONTRA Sensitivity Study

Figures D-2 through D-3 are not included in the non-proprietary version of this document.

APPENDIX E
INTEGRATION CELL SIZE SENSITIVITY

INTEGRATION CELL SIZE SENSITIVITY

This appendix provides an investigation into the sensitivity of the wall condensation analysis to changes in the integration cell size. The integration cell modeling of the CMT wall is discussed in Sections 2.6 and 2.7, and shown in Figures 2.6-1 and 2.7-1. This appendix investigates the following sensitivity:

	Base Geometry	Sensitivity Geometry
Maximum Integration Cell Size	1/3 inch	2/3 inch
Number of Integration Cells	366	196

The 300-series test, C053322, was analyzed with these changes. A 300-series test was selected because the transient is analytically more complex than the 100-series tests -- the analysis methods include the effects of time delays due to changing water level in addition to the 100-series effects of temperature and film variations as a function of elevation.

The steam-region wall heat transfer and wall condensation rate are shown in Figures E-1 and E-2, respectively. Results for the base geometry, as provided elsewhere in this report, and the sensitivity geometry are shown. The sensitivities during the active test time are shown as a percentage of the maximum value in Figures E-3 and E-4. (Sensitivities are shown as a percentage of the maximum values rather than the time-dependent values due to plotting package limitations.)

The very small integration cell size of 1/3 inch was selected to produce converged results. The figures clearly show small sensitivities and are consistent with expectations for a converged analytical model.

Figures E-1 through E-4 are not included in the non-proprietary version of this document.